Department of Mechanical Engineering

THE STRUCTURE AND MECHANICAL PERFORMANCE OF TELEOST FISH SKIN

by

Lawrence J. Szewciw

Department of Mechanical Engineering, McGill University, Montreal

March, 2015

A Thesis

Submitted to McGill University

In partial fulfilment of the requirements

of the degree of

Doctor of Philosophy, Mechanical Engineering

TABLE OF CONTENTS

LIST OF FIGURES

ABSTRACT

THE STRUCTURE AND MECHANCIAL PERFORMANCE OF TELEOST FISH SKIN

Lawrence Jay Szewciw
McGill University, 2014

Supervisor:
Professor Francois Barthelat

The skin of teleost fish is a natural material that exhibits a range of properties that are considered desirable for the biomimetic design of flexible and protective materials and systems. Teleost integument functions to enhance the resistance of the skin to sharp penetration and also to promote the efficient swimming of the fish. Using the common teleost striped bass (*Morone saxatilis*), the puncture mechanics of individual fish scales were first explored and specialized mechanisms of the scale contributing to the penetration resistance of the skin were revealed. The puncture resistance of the intact scaled skin was then investigated, and additional collective scale mechanisms were demonstrated, which further increase the penetration resistance of the skin. The possible mechanical role of teleost skin to function as an external tendon during undulatory locomotion and promote swimming efficiency was also investigated by examining the contribution of both the scales and the underlying dermal stratum compactum to the bending mechanics of the fish. Although the scales were found not to serve an exotendon role during locomotion, the results supported the s. compactum as a tendon-like energy storage device that improves swimming performance. This characterization of the puncture and bending mechanics of teleost fish skin will be applied to the design of biomimetic protective materials that exhibit similar properties as teleost skin, such as high puncture resistance and energy storage capability.

RÉSUMÉ

STRUCTURE ET PERFORMANCE MECANIQUE DE LA PEAU DES POISSONS TELEOSTEENS

Lawrence Jay Szewciw
McGill University, 2014

Superviseur:
Professeur François Barthelat

La peau du poisson téléostéen est un matériau naturel qui présente une gamme de propriétés remarquables pour le domaine de l'étude et de la fabrication biomimétique des matériaux et systèmes flexibles et protecteurs. Le tégument du poisson téléostéen a pour rôle d'augmenter la résistance à la pénétration de la peau ainsi que d'améliorer l'efficacité de la nage du poisson. En étudiant le bar rayé commun (*Morone saxatilis*), la mécanique de la perforation d'écailles de poisson isolées a été en premier explorée et les mécanismes particuliers de l'écaille contribuant à la résistance à la pénétration de la peau ont été révélés. La résistance à la perforation de la peau écaillée intacte a été étudiée, et des mécanismes collectifs additionnels ont été démontrés, augmentant de ce fait la résistance à la pénétration de la peau. La possible fonction mécanique de la peau du poisson téléostéen comme tendon externe durant la locomotion ondulatoire améliorant l'efficacité de la nage a aussi été étudiée en examinant la contribution à la fois des écailles et du stratum compactum dermique sous-jacent du poisson. Bien qu'il ait été constaté que les écailles n'avaient pas la fonction d'exo-tendon pendant la locomotion, les résultats décrivent le s. compactum comme un appareil tendineux de stockage de l'énergie qui augmente la performance de la nage. Cette caractérisation de la perforation et de la mécanique de la flexion de la peau du poisson téléostéen sera appliquée à la fabrication biomimétique de matériaux protecteurs présentant des propriétés similaires à celles de la peau du poisson téléostéen, comme la haute résistance à la perforation ou la capacité de stockage d'énergie.

ACKNOWLEDGEMENTS

A sincere thank you first and foremost to my supervisor, Dr. Francois Barthelat, without whom this research would not have been possible and who offered exceptional instruction, insight and direct assistance with all aspects of this work. This research would also not have been possible without the contributions from Deju Zhu, Dr. Barthelat's former Postdoctoral Research Fellow, and Frank Vernerey of the University of Colorado who provided collaborative help to Dr. Barthelat throughout the duration of these studies. As well, appreciation is given to all members of the Barthelat Biomimetics Materials Laboratory who offered support and assisted with the lab research and data analysis for these experiments, including Ahmad Khayer Dastjerdi, Reza Rabiei, Mohammad Mirkhalaf, Atefeh Nabavi, Mercedes Shiue, Jihane Ajaja, Ravi Kiran Chintapalli, and Sacha Cavelier. Histological processing of fish skin was carried out by Caroline Therien and Jo-Ann Bader at the Goodman Cancer Research Centre, Histology Core (GCRC HC), McGill University. Micro-CT of fish scales was performed by Trina Du, Redpath Museum and Department of Biology, McGill University. Atomic emission spectroscopy tests on scales were performed by Monique Riendeau, Department of Mining and Materials Engineering, and Ranjan Roy and Andrew Golsztajn, Department of Chemical Engineering, McGill University. Training for the fish skin indentation tests with three-dimensional image correlation was provided by Dr. Luc Mongeau and his students, Department of Mechanical Engineering, McGill University. Thank you sincerely to the Faculty of Engineering at McGill University for supporting my Ph.D. studies with a McGill Doctoral Engineering Award. This work was funded by a grant from the National Science Foundation under award CMMI 0927585, and by a Discovery Grant from the Natural Sciences and Engineering Research Council of Canada. Lastly, I was inspired and able to perform this research only with the encouragement and support

of my family and friends, including my father George Szewciw, my sister Linsey Kundu, and a special thanks to Katherine Ann Manuliak.

PREFACE & CONTRIBUTION OF AUTHORS

This traditional style thesis consists of four chapters that contain original research (Chapters 2 to 5 of the thesis). The title of the chapter, researcher names and affiliations, and the contributions of researchers are listed below. It was described in the Acknowledgements section that Dr. Francois Barthelat is Lawrence Szewciw's Ph.D. supervisor, Deju Zhu is Dr. Barthelat's former Postdoctoral Research Fellow, and Franck Vernerey is Dr. Barthelat's collaborator. Cesar Fuentes-Ortega and Ramak Motamedi are former students of Dr. Barthelat.

***Researcher names & affiliations*:**

Lawrence Szewciw[1], Deju Zhu[1], Cesar Fuentes-Ortega[1], Ramak Motamedi[1], Francois Barthelat[1] and Franck Vernerey[2]

[1]Department of Mechanical Engineering, McGill University, Montreal, QC, Canada

[2]Department of Civil, Environmental and Architectural Engineering, University of Colorado, Boulder, CO, USA

The methods and results presented in Figures 2.3, 2.4, 3.1, 3.2, 4.1-4.4, and 4.20 of the thesis were published in the following article: Zhu, D., Fuentes-Ortega, C., Motamedi, R., Szewciw, L., Vernerey, F., and F. Barthelat. 2012. Structure and mechanical performance of a "modern" fish scale. *Advanced Engineering Materials* **14**:B185-B194. Doi: 10.1002/adem.201180057

The methods and results presented in Figures 2.5, 2.6, and 4.5-4.18 of the thesis were published in the following article: Zhu, D., Szewciw, L., Vernerey, F., and F. Barthelat. 2013. Puncture resistance of the scaled skin from striped bass: collective mechanisms and inspiration for new flexible armor designs. *Journal of the Mechanical Behavior of Biomedical Materials* **24**:30-40. Doi: 10.1016/j.jmbbm.2013.04.011

Chapter 2: The structure of striped bass fish skin

LS: optical microscopy of scales, prepared specimens and helped perform atomic emission spectroscopy on scales, prepared specimens and helped perform micro-CT on scales, produced the map of scale thickness from micro-CT data, imaging of the fish and scale morphometrics, prepared specimens and helped perform histology on skin, optical microscopy of skin, prepared specimens and helped perform histology on s. compactum, optical microscopy of s. compactum

DZ: optical microscopy of scales, scanning electron microscopy of scales, imaging of the fish

CFO, RM: optical microscopy of scales, scanning electron microscopy of scales

FV, FB: supervised experiments, provided scientific advice, edited the figures and text

Chapter 3: Tensile properties of striped bass fish skin

LS: tensile tests on descaled skin (s. compactum)

DZ: tensile tests on individual scales

FV, FB: supervised experiments, provided scientific advice, edited the figures and text

Chapter 4: Puncture properties of striped bass fish skin

LS: puncture tests on individual scales, imaging of the puncture sequence, analytical "four flaps" model of the puncture mechanism, ball indentation tests, puncture tests on scales using different substrates, puncture tests at different locations on the scale, puncture tests on stacks of scales, puncture tests on scales in different arrangements, skin indentation tests with three-dimensional image correlation, puncture tests on s. compactum

DZ: puncture tests on individual scales, imaging of the puncture sequence, analytical "four flaps" model of the puncture mechanism, ball indentation tests (with finite element model), puncture

tests on scales using different substrates, puncture tests at different locations on the scale, puncture tests on stacks of scales (with finite element model), puncture tests on scales in different arrangements, skin indentation tests with three-dimensional image correlation

FV, FB: supervised experiments, provided scientific advice, edited the figures and text

Chapter 5: Flexural properties of whole striped bass fish

LS: fish bending tests (scaled vs. descaled) and image analysis (coordinate selection), fish body morphometrics, fish bending tests (descaled vs. incised) and image analysis (coordinate selection)

DZ: fish bending tests (scaled vs. descaled)

FV, FB: supervised experiments, provided scientific advice, edited the figures and text

CHAPTER 1

INTRODUCTION

1.1. Infraclass Teleostei & the biomimetics of teleost fish skin

One of the most diverse groups of vertebrates in terms of form, function, ecological distribution and shear number of species is the Teleostei group of bony fishes [1-5]. The classification or taxonomy of fishes has been described by several previous authors [3-5], and phylogenetic relationships and evolutionary lineages have been traced among fishes of all groups and particularly within the Teleostei taxa of bony fishes [1-5], which represent about 95% of all living fishes [3, 5]. Although cladograms are continually updated based on available evidence of differences between species and phylogenetics or cladistics and evolutionary biology are not the focus of this research, a general classification scheme for teleost fishes is offered here as the following phylogeny: kingdom: Animalia, phylum: Chordata, subphylum: Vertebrata, infraphylum: Gnathostomata, microphylum: Eugnathostomata, unranked: Teleostomi, superclass: Osteichthyes (bony fishes), class: Actinopterygii (ray-finned fishes), unranked: Actinopteri, subclass: Neopterygii, infraclass: Teleostei (teleost fishes) [3, 5]. The classification or systematics of infraclass: Teleostei is complex and, as with all biological phylogenies, evolutionary relationships are determined based on several lines of evidence and distinguishing characteristics, such as morphological and molecular (barcoding) taxonomic characters [5]. Correspondingly, infraclass: Teleostei can be considered to consist of approximately 10 superorders, which are comprised of approximately 40 orders, 450 families, 4,300 genera, and 27,000 species of teleosts [3, 5]. An important group of primitive bony fishes for comparison with the anatomy and biomechanics of teleost fishes, is a group known as “ganoid” fishes, which possess a well-studied and more primitive, ganoid fish scale type compared to the scales of modern teleosts [3-5]. Ganoid fishes consist of five main taxa all of class: Actinopterygii that form a monophyly in combination with infraclass: Teleostei [3-5]. The five clades of ganoid

fishes include birchirs (subclass: Cladistia, order: Polypteriformes, family: Polypteridae), sturgeons (unranked: Actinopteri, subclass: Chondrostei, order: Acipenseriformes, family: Acipenseridae), paddlefishes (unranked: Actinopteri, subclass: Chondrostei, order: Acipenseriformes, family: Polyodontidae), gars (unranked: Actinopteri, subclass: Neopterygii, infraclass: Holostei, order: Lepisosteiformes, family: Lepisosteidae), and bowfins (unranked: Actinopteri, subclass: Neopterygii, infraclass: Holostei, order: Amiiformes, family: Amiidae, subfamily: Amiinae, genus: *Amia*, species: *A. calva*) [3-5]. The diverse and dominant group of bony fishes known as teleost fishes, the word "teleost" meaning "perfect bone" and referring to their advanced evolutionary position among extant bony fishes [5], contains an immense number of species, which at nearing 27,000 species, represents approximately half of all known species of vertebrate animals [3, 5]. This remarkable quantity of species with diverse morphotypes and various aquatic niches demonstrates the vast number of speciation events and environmental interactions that over evolutionary time have led to the highly evolved, modern forms of teleost fishes, which are well adapted and suited for their particular current habitats.

An important selective pressure acting on the majority of fish species since the evolution of teleosts is predator-prey interactions, including both mechanisms of predation and defense that have co-evolved among teleost fishes [2, 6]. A common teleost fish with a global distribution and native to the Atlantic coastline of North America, is the striped bass (*Morone saxatilis*) species of teleost [6]. Although *M. saxatilis* has a wide biogeographic distribution and is a common fish used for produce and in fish farming, little is actually known about several aspects of the ecology of this species, particularly its predator-prey interactions [6]. With respect to their role in the ecosystem as prey items, adult striped bass have a few natural predators, but sources of predation include various aquatic birds, marine mammals, and potentially large pelagic fishes

and sharks [6]. In contrast, juvenile striped bass are known to have several predators, including the bluefish (*Pomatomus saltatrix*) and cannibalism from adult striped bass, which are both significant sources of predation on juveniles [6]. The teeth and biting force of predator bluefish have been studied [7], but the specific predator-prey (tooth-scale) interaction has not been described in terms of mechanical interaction, which is one of the objectives of this work by use of striped bass scales and puncture probes that simulate the teeth of the predators such as bluefish. The primary mechanical function of most types of fish scales is the protection against mechanical disturbances including predator bites [8], and thus teleost scales have evolved a high resistance in response to such penetration events and high contact stresses. Modern teleost scales are also thin, light weight and overlapping, which improved the swimming performance of the fish in terms of speed, flexibility and maneuverability, in comparison to the thick, multi-layered, interlocking and highly protective scales of slower moving, primitive ganoid fishes [8].

The dermal scales of fishes can be classified into four main categories, including placoid, cosmoid, ganoid, and elasmoid scale types, which generally evolved in transitions from one scale type to the next (were derived from each other) in this order [5, 8-10]. Placoid scales or "denticles" are found in cartilaginous fishes and play a main role in hydrodynamics, cosmoid scales in ancient lobe-finned fishes (superclass: Osteichthyes, class: Sarcopterygii), ganoid scales in primitive ray-finned fishes (as previously described, all members of superclass: Osteichthyes, class: Actinopterygii, save for teleost fishes), and elasmoid scales in fishes of infraclass: Teleostei. To be specific, thin elasmoid scales evolved in several groups of fishes including primitive lobe-finned and ray-finned fishes in addition to modern teleosts. Cosmoid scales, derived from a fusion of placoid scales, consist of a layer of dense lamellar bone or osseous tissue (called "isopedine") covered by a layer of spongy bone, followed by a complex dentine

tissue layer (known as “cosmine”), and an outer mineralized, enamel-like coating known as “vitrodentine”. Ganoid scales, derived from cosmoid scales, contain similar layers of isopedine and spongy bone, but these lower layers of the scale are covered by a “dentine” layer (or modified form of cosmine) and a superficial layer of “ganoine” (or modified form of vitrodentine). Contrarily, elasmoid scales are derived from either cosmoid or ganoid scales, and though elasmoid scales still contain the isopedine tissue found in primitive cosmoid and ganoid scales as well as additional outer surface features of the scale, the layer of spongy bone and layer of dentine with superficial mineralization are highly reduced or absent in elasmoid scales. Elasmoid scales of modern teleost fishes are the least mineralized of all elasmoid scales and are found in two forms of thin, translucent “leptoid” or “bony-ridge” scales (with mineralized ridges and unmineralized furrows on the surface of the scale), known as “cycloid” and “ctenoid” scales. The primary differentiating characteristic between cycloid and ctenoid scales are the stiff projections known as “ctenii” with hydrodynamic functions that are located at the posterior margin of ctenoid scales, but are absent in cycloid scales. Both cycloid and ctenoid types of teleost fish scales may be found on the same fish and may be preferentially distributed on certain regions of the fish’s body to offer different mechanical and non-mechanical functional benefits [5, 8-10].

The fish scales employed in this study were selected to represent the typical ctenoid type of elasmoid scale found on teleosts, and were dissected or examined *in vivo* using the model teleost species, *M. saxatilis*, the majority of the body surface of striped bass being covered by ctenoid scales that vary in size along the length of the fish. The main goal of this research was to characterize the structure and mechanical performance of teleost fish skin from striped bass in terms of both puncture resistance and flexural properties in order to identify key underlying

mechanisms responsible for the enhanced performance of this natural material in both the resistance to penetration and in the efficient locomotion of the fish. An understanding of the multifunctionality and precise mechanical design of teleost skin at multiple hierarchical levels and its contribution to the mechanical performance of the whole fish is the necessary initial research for the eventual biomimetic design and fabrication of artificial materials and systems that replicate the mechanisms operating to enhance the properties of natural teleost integument. The ultimate aim of this research, therefore, falls within the field of biomimicry or biomimetics, which may be generally defined as the production of synthetic systems that mimic and reproduce the structure, mechanisms and functions of biological materials [11]. A variety of natural materials have inspired novel engineering designs in recent years, and a relevant example of a fish-skin inspired biomimetic material is bodywear and other coverings with comparable surface features as the placoid scalation patterns exhibited by shark skin with its enhanced hydrodynamic properties and locomotory function [12].

While the range of biological tissues studied for biomimetic design and their applications are diverse, the natural scalation or squamation patterns found on a variety of vertebrate species have been identified as high-performance systems and advantageous designs for artificial protective systems with additional mechanical and non-mechanical benefits such as flexibility and breathability. The development of synthetic, flexible and protective systems, particularly personal armor systems, that were inspired from the natural scalation patterns of various animals including fishes, dates back to ancient Roman time periods when pieces of military equipment (scaled armor known as Lorica squamata) demonstrated some of the basic design principles and benefits of natural scaled armors [13]. The development of modern protective gear used for military applications, such as protective vests with embedded and overlapping steel or ceramic

plates [14], has advanced the understanding and design of scaled armor systems based on natural scalation patterns, but replication of these systems has focused on mechanisms operating at macroscopic levels that impart benefits from overlapped scale or plate arrangements, mechanical interactions between plates, and whole-system design [14]. These protective systems have not yet replicated and taken advantage of the complex microstructural design of such biological tissues and how the protective properties of natural materials are generated from the combination of weak component materials into composite material with fine structural detail and resultant mechanisms that allow the natural tissue to perform its protective function [11]. Elucidation of the structure-property-function relationships and how the protective capabilities of natural systems are produced from extrinsic mechanisms operating at different hierarchical levels within the material structure is necessary for the development of synthetic systems with optimized protective capacity, which is synergized over multiple length scales [11].

To this end, the scaled integument of fishes has received attention recently as a high-performance natural system with enhanced penetration resistance arising from specialized mechanisms occurring at different length scales within the material. Recent research on the puncture mechanics of fish skin and identification of mechanisms of penetration resistance has focused on energy dissipative mechanisms displayed by the multi-layered scales of ganoid fishes and the mechanical functions of intact ganoid integument with scale articulation [15], and less research has been performed on the puncture mechanics of the scales and skin of teleost fishes. Additionally, teleost fish skin is a multifunctional natural material that exhibits a range of mechanical properties necessary for the effective functioning of the integumentary system in several mechanical roles, including its contributions to both the puncture mechanics and bending or undulatory swimming mechanics of the fish [8]. The tensile properties of fish skin from a

variety of teleosts have been measured, and the flexural and swimming mechanics of whole teleost fishes have been studied [16]. This research on the tensile properties of teleost skin and its contribution to swimming mechanics, in combination with similar research on cartilaginous fishes [17], led to the proposal of a potential exotendon function of teleost skin and its possible role as an energy storage device that improves the swimming efficiency of the fish [16, 17]. The external tendon hypothesis of the integument, which identifies the lower dermal, collagenous stratum compactum layer of the skin as the source of the tendon-like properties, was originally proposed for shark skin [17], but has also been studied in teleosts [16]. This study on the mechanical performance of *M. saxatilis* teleost fish skin, therefore, also includes an examination of the tensile properties of the integument and the contributions of main structural features and mechanisms of the skin, such as mechanical interaction of scales and tendon-like mechanisms of the stratum compactum, to whole fish bending mechanics and locomotion.

In this work, knowledge of the tensile properties of striped bass skin and the potential exotendon role of the skin during locomotion is combined with knowledge of the mechanisms that were revealed to control the puncture resistance of the skin, in order to provide an efficient transfer of biological technology into fish-skin inspired biomimetic protective systems with similar diverse properties as teleost skin. Teleost fish skin not only exhibits high protective capacity in the form of puncture resistance and tendon-like properties that increase swimming efficiency, but is also flexible, breathable, light weight and transparent [8], which are all properties considered desirable in synthetic protective systems with additional mobility functions. The research presented in this study on the structure and mechanical performance of teleost fish skin substantially contributes to the understanding of the puncture and bending mechanics of teleost skin and of whole teleost fishes. The mechanisms generating the optimized

mechanical properties of this natural material will now be incorporated into the bio-inspired design of synthetic, flexible, protective and locomotory systems with additional desirable properties similar to those found in teleost fish skin.

1.2. Applications to fish skin-inspired biomimetic materials

Biomimetics may be defined as the development of synthetic systems that mimic the structure and function of biologically produced materials and mechanisms [11]. Nature can serve as a source of inspiration for new and alternative engineering designs, and biomimetics has started to produce materials with remarkable properties [11]. The natural materials that served as models for these recent developments include seashell [18], glass sponge skeleton [19], toucan beak [20], spider silk [21], and shark skin [12]. Made of relatively weak component materials, the mechanical performance of these natural materials is derived from their microstructure, often complex and displaying hierarchical morphology [11]. An understanding of the structure-property-function relationships is therefore required and will provide insight into the design of new engineering materials [11]. Various experiments [22] and models [18] are thus being employed to better understand these extraordinary materials. Meanwhile, artificial materials inspired by these natural materials have started to emerge [23]. We identified the scaled skin of fish, specifically teleost fish skin represented by striped bass (*M. saxatilis*), as a high-performance natural system with the potential to inspire novel biomimetic materials. The aim of this research was to understand the puncture and tendon-like mechanisms in fish skin, through experimentation and the characterization of fish skin structure and mechanics. This study established the structure-property relationships that will be essential for the fish skin-inspired design of new flexible artificial skins with optimal mechanical performances.

A similar biomimetic approach using teleost scales dissected from the flathead mullet, *Mugil cephalus*, was carried out by [24], and their results support fish scales and fish skin as promising sources of biomimetic inspiration for the production of high performance materials. Fish skin has remarkable and desirable mechanical properties such as flexibility, resistance to penetration, and tendon-like properties, in addition to ultra-thinness, light weight, transparency and breathability [8]. Surprisingly, this material has received little attention with respect to materials development, even though Currey [25] noted that some fish scales are so tough that they resist fracture even after immersion in liquid nitrogen. There are only a few mechanical studies of fish scales and skin, and although the full range of this biological material's function is unknown, our observations for *M. saxatilis* teleost skin show impressive performances. Our results demonstrate the remarkably efficient protection against sharp puncture provided by individual scales to teleost fish skin by way of a specialized scale puncture mechanism. While individual scales resist penetration from predator bites, at a higher length scale, the overlapped arrangement of scales, or scalation pattern, provides a flexible skin that allows for changes in shape. We also show how the imbricating scales mechanically interact upon puncture to increase penetration resistance and protect underlying tissues. As well, we report the tensile properties of descaled teleost skin (composed mainly of s. compactum) and the bending properties of whole teleost fish with contributions from the skin, to investigate the hypothesis that the s. compactum layer of teleost skin also acts as an external tendon to enhance swimming efficiency. In addition to these mechanical functions, the surface of fish scales and skin is also known for improving hydrodynamics [8, 26, 27]. The structure of scaled skin at the macroscopic level probably inspired the scaled armor used by ancient Roman military to provide penetration resistance and freedom of movement [13], but such early armor designs lacked a fundamental understanding of

the mechanics of fish skin. The hierarchical structure of fish skin appears to play a critical role in its overall mechanical performance, and we have now investigated the contributions and synergies of each length scale. For example, we show how neighboring scales interact to prevent penetration and protect soft underlying tissues. Such understanding is necessary for the replication of the performance of fish scales and skin into next generation personal armor systems.

The design and testing of fish skin-inspired body armor has commenced with puncture testing of artificial fish scales with similar structural and material properties as found in *M. saxatilis* teleost scales [28-30]. These early prototypes for synthetic fish scales closely mimic the optimized design of teleost scales to resist puncture, that of a biphasic structure (see Chapter 2) with an upper, hard and stiff material (similar to the "bony" layer) adhered at an interface to a lower, soft and strong backing membrane (similar to the "collagen" layer). The effects of cross-ply microstructure have also been replicated by inducing a similar specialized failure mode in the scale, as described in Chapter 4. These artificial scales have been designed to possess other desirable qualities of teleost scales such as light weight and thin-structure. Initial designs for protective systems inspired from intact teleost skin [28-30], have incorporated mechanical benefits of the next hierarchical level at the macroscale of the overlapped arrangement of scales, for example flexibility, breathability and scale interaction, which are discussed in Chapter 4. As well, the mechanical benefits of adding an underlying supportive material with similar attractive properties as the s. compactum have been investigated [28-30], such as penetration resistance and potential tendon-like properties, investigated in Chapters 3 and 5. The supportive layer modeled after the s. compactum would integrate all components of the protective system into a cohesive whole [28-30], and in addition to the mechanical benefits investigated in this work,

could also offer other benefits similar to the s. compactum, such as resistance to internal pressure [17, 31, 32], maximized body volume [17, 31, 32], wrinkle prevention [16], and prevention of torsion or other body motions with stability and flotation effects [17, 32-35].

1.3. Thesis objectives

(i) Characterize the structure of striped bass fish scales and skin

(ii) Characterize the tensile mechanics of striped bass fish scales and skin to reveal the mechanisms producing their optimized tensile properties, and to test the hypothesis that the s. compactum functions as a whole body exotendon to promote swimming efficiency

(iii) Characterize the puncture mechanics of striped bass fish scales and skin (including scale interaction) to reveal the mechanisms producing their enhanced penetration resistance

(iv) Investigate the contribution of fish scales and the s. compactum to the flexural response (including bending stiffness) of whole striped bass fish, to test the hypothesis that the scales or s. compactum function as a whole body exotendon to promote swimming efficiency (reduce the energy required for locomotion via facilitation of muscle contraction)

CHAPTER 2

THE STRUCTURE OF STRIPED BASS FISH SKIN

2.1. Overview: The hierarchical structure of teleost fish skin

Teleost fish skin consists of 3 basic layers, in an apical to basal direction these layers are: the cuticle, the epidermis, and the dermis, which is composed of an upper stratum (s.) spongiosum and a lower s. compactum (Figure 2.1) [8]. The two tissue layers underlying the integument include the hypodermis, followed by subcutaneous muscle (Figure 2.1) [8]. The cuticle consists of mucous secretions that coat the metabolically active epidermis [8], which, relative to the dermis, is a thin covering layer (Figure 2.1) that contributes little to the mechanical properties of fish skin investigated in this study and thus epidermal structure is not described. The fine structure of teleost fish skin has been studied extensively [8], and particular attention has been given to the structure of the dermal scale [8, 9, 26, 36, 37]. The dermis in teleost skin is composed largely of a network of collagen fibrils, but dermal scales are also mineralized with the calcium phosphate salt, hydroxyapatite (HAp) (Figure 2.1) [8]. These calcified structures originate in the loose connective tissue of the s. spongiosum layer, but often evaginate the overlying epidermis on an angle to produce a pattern of scale overlap or imbrication, the scales projecting towards the tail to improve hydrodynamic properties (Figure 2.1, 2.2a) [8, 36]. The precise non-random patterning of dermal scales in teleost integument, known as the scalation or squamation pattern (pattern of scale overlap), varies widely across teleosts (Figure 2.2a) [8, 36]. A variety of scalation patterns have evolved across teleosts from several overlapping scales to non-overlapping scales, each pattern performing unique functions [8]. The anterior area of each scale is embedded in the s. spongiosum and possibly anchored in place by circular ridges (circuli), and toothlike processes (denticles) lining their edges, on the surface of the scale (Figure 2.2b,c,d) [8, 9, 26, 36-39]. The surface of the anterior region also contains radial grooves (radii) or gaps in the upper mineralized layer of the scale, which may increase the flexibility of the scale

(Figure 2.2b,c,d) [8, 9, 26, 36-39]. On the other hand, the posterior region evaginates the epidermis and overlaps the anterior region of one or more preceding or posterior scales (Figure 2.1, 2.2a) [8, 36]. The surface of the posterior region contains stiff projections (ctenii) with hydrodynamic functions (Figure 2.2b) [8, 26]. Within an anteroposterior (A-P) row of scales, there are also dorsoventral (D-V) scales that insert between the A-P scales, providing additional overlap (Figure 2.2a) [8, 36].

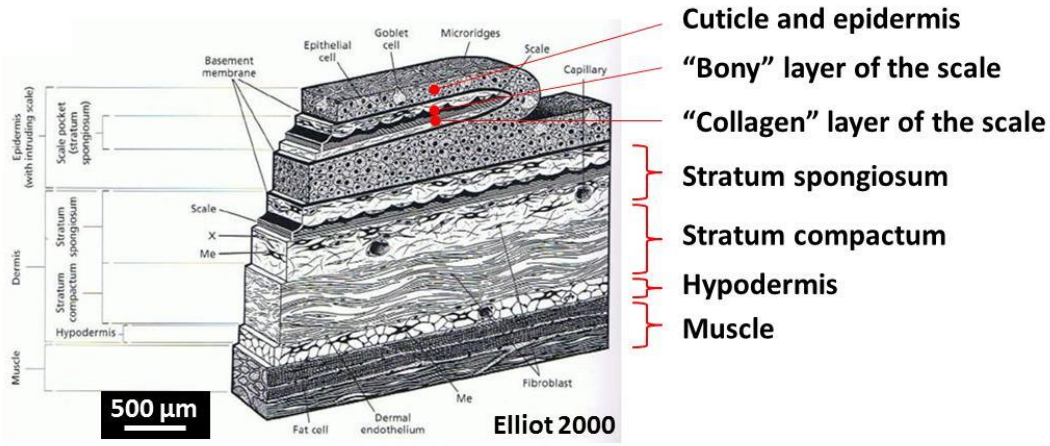

Figure 2.1. Generalized cross section of teleost fish skin showing: the cuticle and epidermis, dermal scales with upper mineralized and lower unmineralized layers, the gelatinous s. spongiosum that surrounds the scales, the s. compactum consisting of a cross-helical arrangement of collagen fibres, and the underlying hypodermis and muscle (adapted from [8]).

Teleost scales consist of 3 main layers in the posterior field, whereas the outer layer is absent in the anterior field [8, 10, 37]. These layers, in an apical to basal direction, are termed the "outer limiting" layer, the "bony" layer, and the "collagen" layer (Figure 2.2c) [8, 10, 37]. The bony and collagen layers both consist of three molecular components: collagen protein, 'ichthylepidin' protein, and HAp mineral, but the bony layer is significantly more calcified than the collagen layer [8, 10, 37, 40]. The average HAp mass fraction of whole (homogenized) teleost scales ranges from *ca*. 16 to 59% [40, 41], and the percentage points difference in

calcification between the bony and collagen layers is *ca*. 20 to 35% across teleosts [42]. The outer limiting layer is almost completely mineralized with HAp [8, 10, 37]. Examination of teleost scales in cross section after histological staining for calcium salts [43] or other techniques such as transmission electron microscopy [37, 43, 44] has revealed the general mineral distribution pattern in the scale including the upper region of calcification with its mineralization front (Figure 2.2c) [37]. Mineralization results in calcification of the outer limiting and bony layers, and an uneven mineralization front located below the midline of the scale thickness and well into the collagen layer (Figure 2.2c) [8-10, 36, 37]. We suspect that the waviness of the mineralization front may prevent shearing between the mineralized and unmineralized portions of the scale during scale flexure. The collagen fibrils in the collagen layer of the scale are arranged in a plywood pattern with the lamellae consisting of parallel fibrils that rotate across lamellae by angles that vary between species (Figure 2.2d) [8, 36, 42, 45-48]. Individual collagen fibrils may also be grouped into bundles or collagen fibres [49]. Similar plywood patterns of collagen fibrils are found in animal tissues that experience stresses in multiple directions, for example soft-shelled turtle shell [50] and human annulus fibrosus [51], and hence a similar function of increasing strength in multiple directions has been proposed for the plywood nature of the fish scale collagen layer [49, 52-56]. The main function of dermal fish scales is mechanical protection against predators, especially prevention of penetration of the skin by predator teeth [6, 7, 53, 57-59]. Several other layers throughout the thickness of fish skin exhibit a similar orthogonal plywood pattern of collagen fibrils, including basement membranes and the thick dermal s. compactum layer [8, 9, 60]. The s. compactum, which exhibits a cross-helical arrangement of collagen fibres with alternating lamellae that exhibit crimping of fibres (Figure 2.1) [8, 33, 61], has been proposed to function in stretch resistance and in locomotion via an

external tendon effect [8, 9, 16, 17, 33, 61], but has also been implicated in enhancing penetration resistance in shark skin [33].

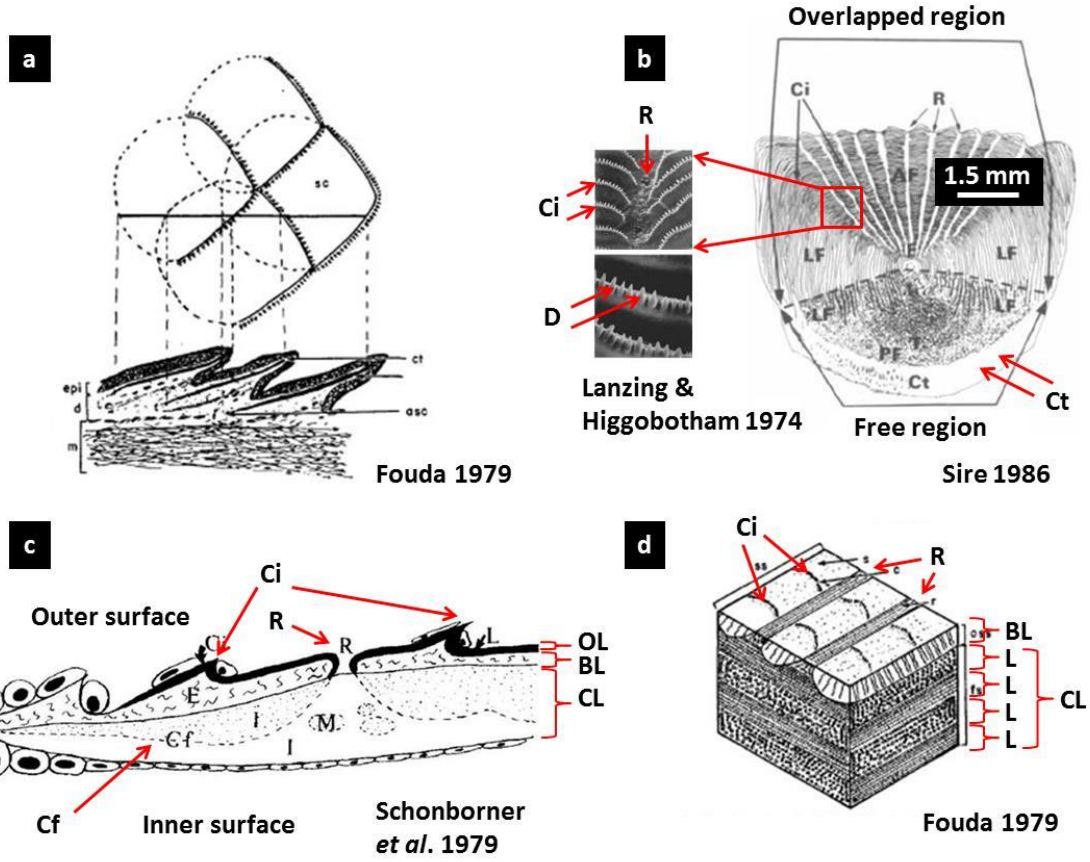

Figure 2.2. (a) The scalation pattern of a teleost fish [36]; (b) surface structure of a teleost fish scale showing the overlapped region (anterior and lateral fields), free region (posterior and lateral fields), circuli (Ci), denticles (D), radius (R) and ctenii (Ct) [26, 38] (scale bar is approximate); (c) cross section of a teleost scale showing circuli (Ci), radius (R), outer limiting layer (OL), bony layer (BL), collagen layer (CL) and the calcification front (Cf) [37]; (d) cross section of a teleost scale showing the bony layer (BL) with circuli (Ci) and radii (R), and the collagen layer (CL) with its plywood pattern of collagen fibrils arranged in alternating lamellae (L) [36].

2.2. Individual scales

In this section we have investigated the structure of a single teleost (ctenoid) fish scale from striped bass *Morone saxatilis*. Like many other structural biological materials [62-64], the structure of teleost fish scales displays a characteristic hierarchical structure, built over several

distinct length scales (Figure 2.3). At the macroscopic level, the scales are staggered and cover most of the body of the fish (Figure 2.3a,b). This arrangement provides a continuous barrier to penetration and flexural compliance. When the fish is highly curved (at the end of a swimming stroke), the scales interact more strongly, which stiffens the skin in flexion [65]. The skin then acts as an "external tendon", storing mechanical energy, which can be recovered to facilitate the onset of the next stroke [16, 66]. At the mesoscale level, an individual scale from an adult striped bass is a thin plate with an irregular pentagonal shape, about 10 mm in diameter (Figure 2.3c).

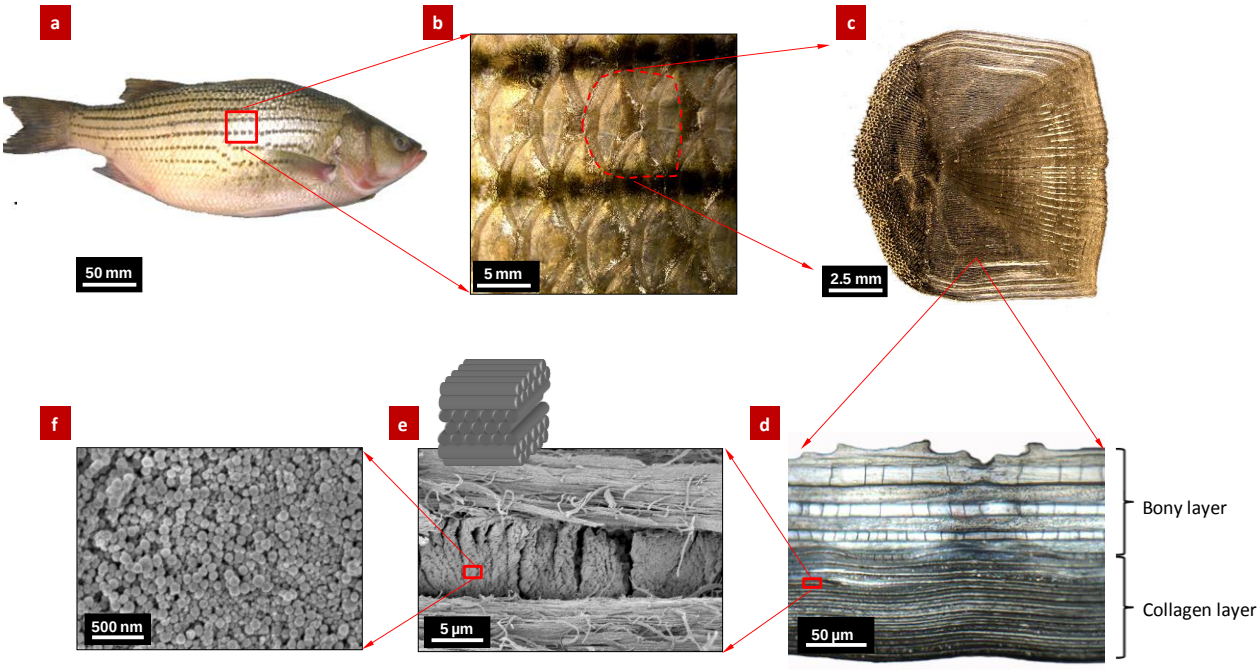

Figure 2.3. The hierarchical structure of a teleost fish scale from striped bass, *M. saxatilis*. (a) Whole scale; (b) staggered multiple scales; (c) an individual scale; (d) cross-section of a scale; (e) cross-ply collagen structure; (f) collagen fibrils.

The posterior area of the scale displays rough patterns (ctenii) which offer attractive hydrodynamic properties [26, 27], while the anterior area consists of grooves in the radial direction (radii) and ridges that form circular rings (circuli) around a central area called the

'focus' [67]. Radii and circuli possibly provide increased flexibility and anchoring of the scale, respectively [26]. Teleost scales are composed of collagen fibrils type-I, and are partially mineralized with hydroxyapatite (16-59% mineral content in weight [37, 41, 54, 56, 68]). The outer layer of the scale is significantly more mineralized and often referred to as the "bony layer", whereas the inner layer ("basal" or "collagen" layer) is mineralized mostly near the bony layer, but with mineralization pockets proceeding well into the collagen layer [37, 57]. In striped bass, bony and collagen layers have approximately the same thickness (100 μm for larger scales from the mid-lateral body region), as observed with optical microscopy and micro-CT on several scales. Using AES (atomic emission spectroscopy), we measured an average hydroxyapatite mass fraction of 46% for the whole scale (after homogenization of multiple scales from a single fish). The density of collagen (1.33×10^3 kg/m^3) and hydroxyapatite (3.17×10^3 kg/m^3) [56] were used to estimate the volume fraction of hydroxyapatite as 26%. In another experiment, we separated multiple scales from a single fish into two samples by dissecting a few plies off the collagen layer of each scale. The homogenized upper and lower samples gave hydroxyapatite mass contents of 50% and 14%, respectively (30% and 6% in volume fractions), confirming that the upper region of the scale is significantly more mineralized than the lower region. These results are consistent with reports of a general 20-35% percentage points difference in mineralization between the bony and collagen layers [42]. Bony and collagen layers are cross-ply layered composites, each ply being made of parallel collagen fibrils rotated across layers by angles that can vary from species to species [42, 45-48]. In striped bass, we found that the basal layer of larger scales is formed of 20-25 plies about 4-5 μm thick each (Figure 2.3d), where the collagen fibrils are rotated by 90 degrees from one ply to the next (Figure 2.3e). Cross-ply collagen structures are typically found in natural tissues that undergo multiaxial stresses (shell of

soft-shelled turtles [50], human annulus fibrosus [69]). Several authors have discussed the importance of the plywood nature of the collagen layer to whole fish scale mechanical properties [49, 52-56], in general by providing the scale with strength along multiple directions. At smaller length scales, individual collagen fibrils, about 50 to 200 nm in diameter, can be observed on a cross section of the scale (Figure 2.3f). Interestingly, we found that in striped bass the 90 degree cross-ply is achieved by alternating layers composed of radial fibrils ("R" layers) with layers made of circumferential fibrils ("C" layers), both layers being organized around the focus of the scale (Figure 2.4). This arrangement is consistent with the growth of individual scales, which occurs by deposition of collagen at the periphery of the scale [8, 70].

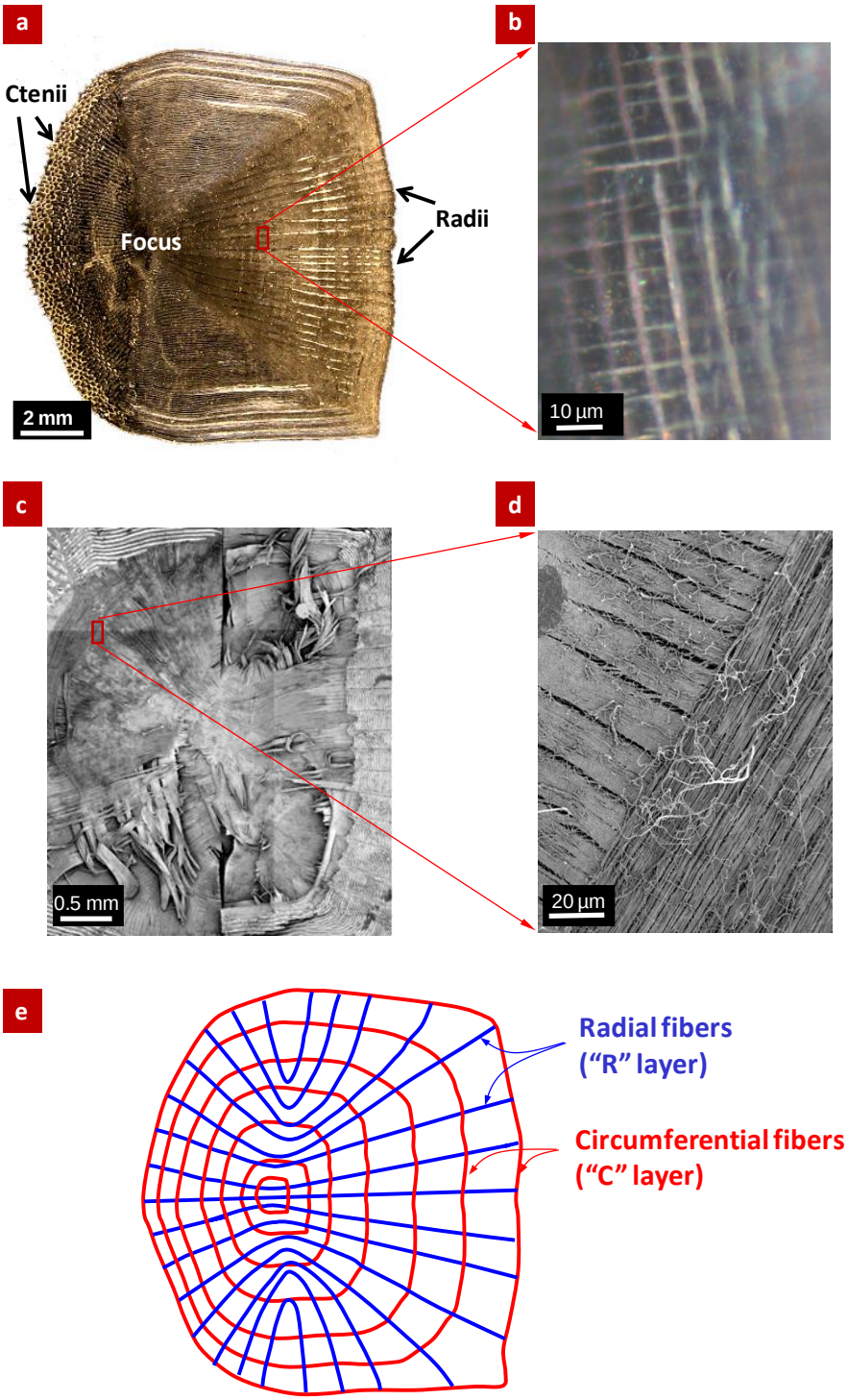

Figure 2.4. Arrangement of the collagen fibrils in a striped bass scale. (a) Top view of the whole scale showing surface features (optical micrograph); (b) bottom view showing collagen fibers in the collagen layer; (c) removal of the bony layer reveals the radial-circumferential (R-C) pattern of the collagen fibrils; (d) locally, the fibers are orthogonal from one layer to the next; (e) schematics of the R-C pattern.

We also characterized the three-dimensional morphology of individual scales using micro-computed tomography (micro-CT). Figure 2.5a shows the surface of the scale and clearly reveals surface features such as posterior ctenii (stiff projections with hydrodynamic functions) and anterior radii (radial grooves that may increase scale flexibility) [8, 26]. Figure 2.5b shows a map of the scale thickness computed from the micro-CT scans. These data reveal that individual scales are thickest at the focal point on the scale (the "focus"), and that the thickness progressively decreases towards the edges of the scale. The pattern of thickness distribution conforms to the traditional sectors of the scale based on surface roughness (focus, lateral, anterior and posterior regions). When scales are superimposed the "effective" thickness of protective material is increased. Interestingly, examination of the scalation pattern (Figure 2.6b) and the thickness distribution of individual scales (Figure 2.5b) suggests that this "effective thickness" generated by superposing three scales, is uniform over the surface of the fish.

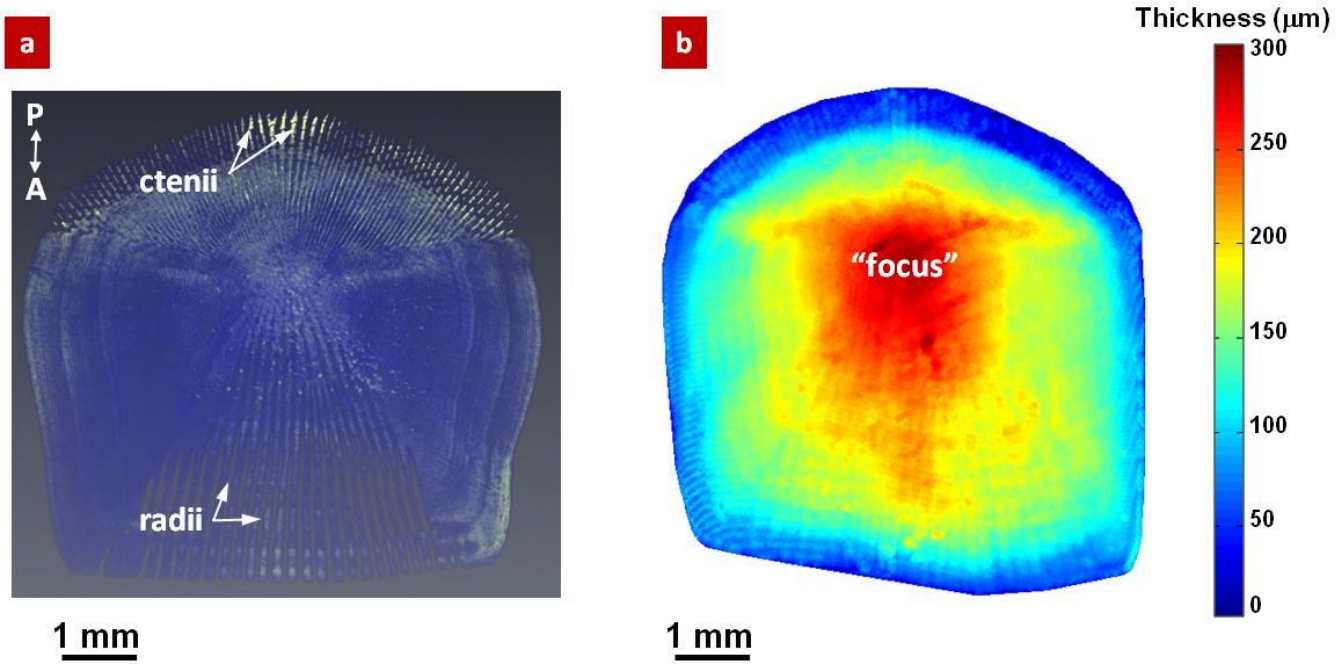

Figure 2.5. (a) Micro-CT image of an individual scale showing ctenii and radii (A-P=anteroposterior); (b) map of scale thickness obtained from micro-CT.

2.3. Arrangement of scales (scalation pattern)

The arrangement of fish scales (scalation pattern) was characterized for striped bass. The majority of the body of the fish is covered by scales (Figure 2.6a). A detailed analysis of the scalation pattern revealed that in striped bass the scales are arranged in rows along the length of the fish. Each scale overlaps with six other neighboring scales: three scales on the anterior side, and three scales on the posterior side (Figure 2.6b). Interestingly, the arrangement of the scales is such that any point on the (lateral) surface of the fish is covered by three overlapping scales. The scales are however not uniform in size over the entire fish. For example, Figure 2.6c shows the variation of scale diameter along the dorsal line of the fish. The scales are the smallest near the tail and near the head, and that they can be up to twice as large at a distance of about 1/3 of the fish length from the head. The absolute size of individual scales varies in dimensions with the age of the fish (fishes keep growing indefinitely so that there is no "adult size") [8]. Figure 2.6d shows a histological section of the skin of striped bass, prepared with H&E staining. The section shows three overlapping dermal scales with a softer, gel-like connective tissue (called stratum (s.) spongiosum, [8]) between the scales. Each individual (larger) scale is 200-400 μm thick, and composed of collagen type I fibrils (see previous section 2.2.). The outer "bony" (calcified) layer represents about one half of the thickness and is mineralized with hydroxyapatite (HAp) [8, 9, 37], as revealed here with the selective H&E and von Kossa staining (Figure 2.6d). The collagen fibrils of the inner "collagen" layer are arranged in a plywood pattern with the lamellae consisting of parallel fibrils that rotate across lamellae by angles that vary between species [46], the plywood pattern increasing strength in multiple directions [54, 56]. Figure 2.6d also shows cross sections of the intricate roughness patterns (called circuli with denticles) covering the outer surface of the scales, which may provide mechanical anchoring of the scale [8, 26, 38].

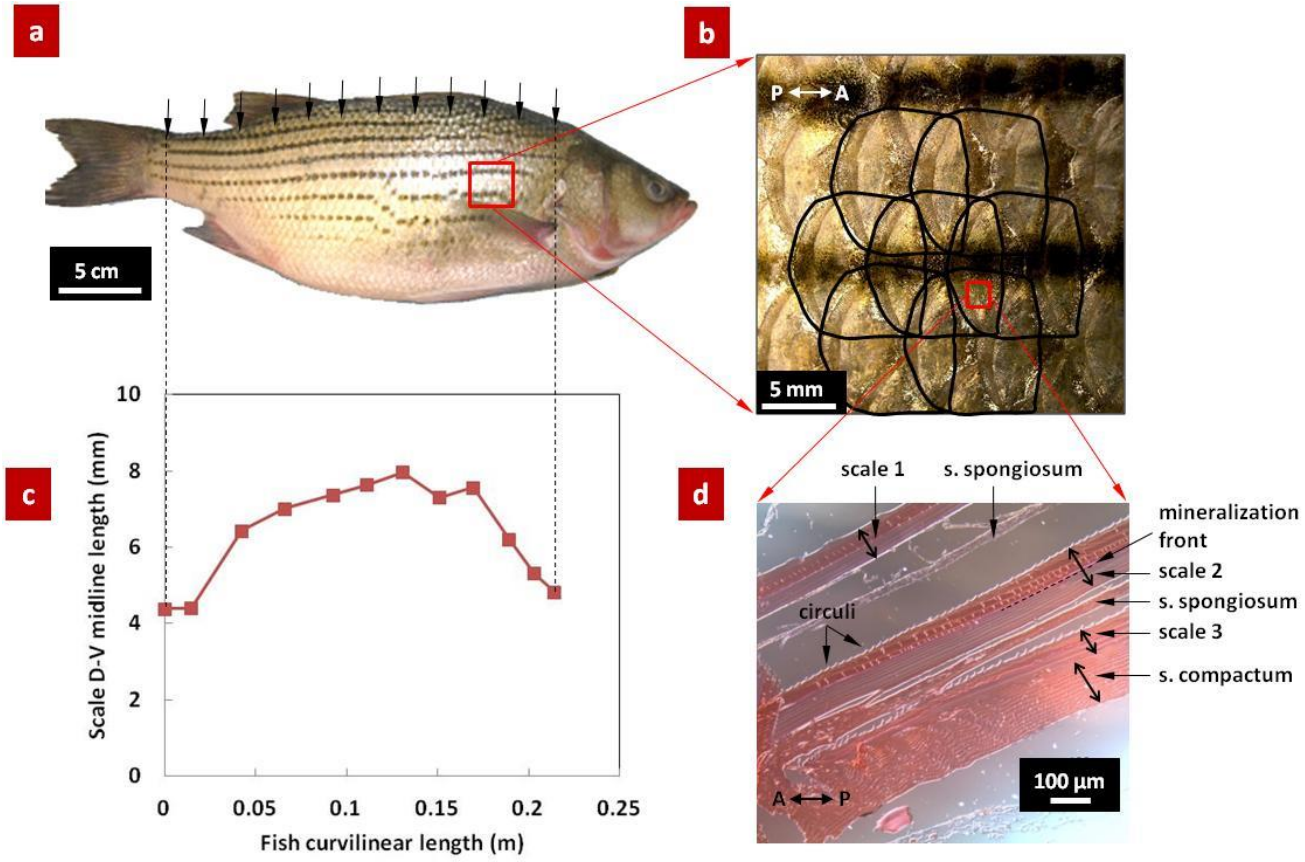

Figure 2.6. (a) Whole striped bass; (b) detail of the scalation pattern: the central scale covers three posterior (P) scales and is covered by three anterior (A) scales, resulting in three scale overlap at any location on the skin; (c) dimensions of individual scales along the length of the fish; (d) histological cross section showing three scale overlap (H&E stain).

2.4. Stratum compactum

The lowermost dermal tissue, called stratum (s.) compactum [8], is a 100-200 µm thick dense layer of collagen fibrils in which the scales are anchored (Figure 2.6d). The s. compactum, which exhibits a cross-helical arrangement of collagen fibres, has typically been proposed to function in stretch resistance and in locomotion via an exotendon effect [8, 9, 16, 17, 33, 61]. However, the s. compactum has also been implicated in improving penetration resistance, at least in sharks [33].

2.4.1. Material & methods

2.4.1.1. Sample collection & dissection

The histology methods used to characterize the structure of the s. compactum were similar to those followed by Naresh *et al*. [61] and the collagen fibre and crimp angles reported along the A-P axis of the fish showed similar patterns as in the shark and teleost skin studied by [16, 17, 33, 61]. We first present a detailed description of the microstructure and composition of the s. compactum using histology methods. Whole, fresh (recently deceased and on ice) striped bass (*Morone saxatilis*) fish were acquired from a local fish store (Montreal, QC, Canada) and originated from the fish supplier, Nature's Catch, Inc., Clarksdale, MS, USA. The fishes were the same size as those used in all chapters of the thesis, having a length (l) and width (w) of *ca*. 40 cm and 10 cm, respectively, and were kept on ice before sample collection. Tissue samples were dissected from three fishes. One fish was fully descaled on its left side from the lateral line down to the ventrum. Using a scalpel, three tissue blocks (samples A-C in Figure 2.7) were dissected from the fish immediately ventral to the lateral line and at three anteroposterior (A-P) locations (anterior, mid and posterior). The dimensions of the tissue blocks were, l (A-P axis) x w (D-V axis) x depth (d) = 3 cm x 2 cm x 0.5 mm. Each tissue block was immersed in 100 ml (>20x vol. tissue block) of 10% neutral buffered formalin (NBF) for tissue fixation. Three additional, smaller tissue blocks (samples D-F in Figure 2.7) were dissected from the fish immediately ventral to the first three samples. The dimensions of the smaller tissue blocks were, l x w x d = 2 cm x 1.5 cm x 0.5 mm. The mean thickness of samples A-F (n=6) was 0.467 $\pm$ $3.07 \cdot 10^{-2}$ mm and measured using digital calipers. All mean values reported are followed by the standard error of the mean ($\pm$ s.e.). Each of the smaller tissue blocks was immersed in 50 ml of 10% NBF. From the other two fish, five similar samples were prepared in 10% NBF, and were

dissected from the anterior and mid regions of the fish. The anterior specimen (G) was located directly above the lateral line, and the four mid specimens (H, I and J, K) were located directly above the lateral line and close to the ventrum, respectively (Figure 2.7). The five extra specimens (G-K) were immersed in 50 ml of 10% NBF. The tissue samples were stored at 4 °C and submitted for histological processing.

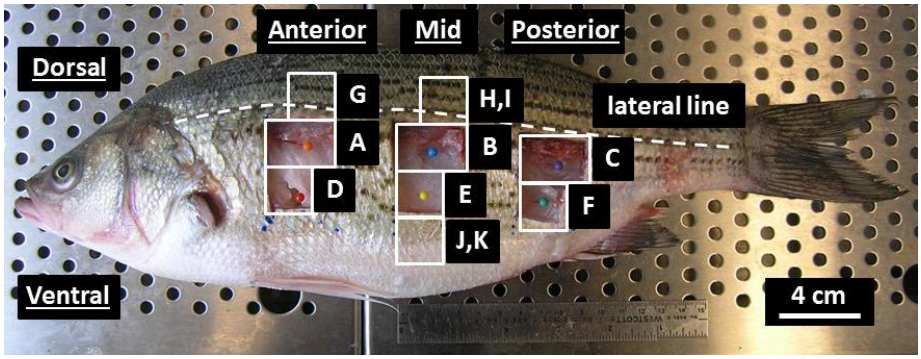

Figure 2.7. Location of striped bass skin samples collected for measurement of collagen fibre & crimp angles of the s. compactum layer. Samples were dissected at three locations along the anteroposterior (A-P) axis (anterior, mid & posterior locations), and at different distances away from the lateral line along the dorsoventral (D-V) axis. Samples A-C were used to produce sagittal sections, whereas samples D-K were used to produce transverse sections along the D-V axis.

2.4.1.2. Histological processing & microscopy

The tissue blocks were dehydrated in ethanol, embedded in paraffin, and sectioned into either *ca*. 5 μm sagittal (horizontal) sections or transverse (cross) sections, the latter cuts made along the D-V axis. Samples A-C were used to produce sagittal sections, whereas samples D-K were used to produce cross sections. All sections were stained with H&E. The H&E stained sagittal and cross sections were imaged with light microscopy. Optical micrographs were taken with an Olympus BX51M microscope in standard and differential interference contrast (DIC) mode.

2.4.1.3. Image analysis

Figure 2.8 shows typical micrographs from histology sections. Sagittal sections clearly show the collagen fibrils, which are relatively straight from that direction (Figure 2.8a,b). They form a cross-ply arrangement, with an angle that can be easily measured (Figure 2.8b). For each of the three sagittal sections (anterior, mid and posterior locations), several sites within the inner undamaged region of the section were imaged to produce an average fibre angle for each of three A-P locations. The cross-helical arrangement of collagen fibres exhibited by the s. compactum results in four measureable fibre angles at any location on the fish skin with respect to the A-P axis, a small and large angle for each of the alternating lamellae of right- and left-handed helically-wound collagen fibres. Mean collagen fibre angles (small angles) were calculated at all three A-P locations (anterior, mid and posterior) for both fibres or lamellae in the anteroventral-posterodorsal (AV-PD) and the anterodorsal-posteroventral (AD-PV) direction, or left and right helices, respectively, for the left side of the fish.

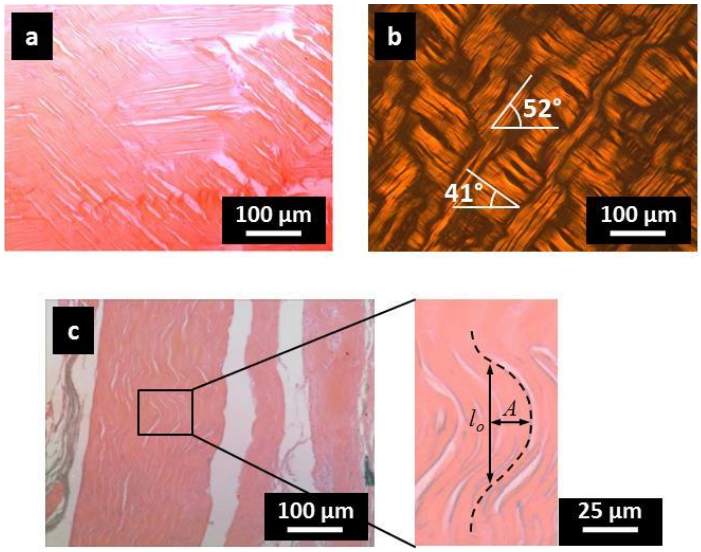

Figure 2.8. Optical micrographs of H&E stained sagittal sections of striped bass skin in both (a) standard and (b) DIC modes, showing the s. compactum and its cross-helical arrangement of collagen fibres, including fibre angle measurements; (c) optical micrograph (with enlarged portion) of an H&E stained cross section of striped bass skin, showing the s. compactum and the waviness or crimping of collagen fibres, including wave parameter measurements.

Even though the fibres are almost continuous within the tissue, the fibres shown in Figure 2.8a,b appear to be discontinuous. This effect arises because the fibres are not straight in the out-of-plane (sagittal) direction, and because they were cut during the specimen preparation steps. Figure 2.8c shows the cross section of the tissue, where the multilayered structure of the fibres is evident. The fibres are also significantly crimped, which can be characterized by a sine function. Using the sine function, $y=A\cdot\sin(\pi x/l_o)$, where A=amplitude and l_o=wavelength, and thus $A=(l_o\cdot\tan\theta_o)/\pi$, the contour length of the ellipse, L, can be calculated as $L=\pi[1.5(a+b)-(ab)^{0.5}]$, where $a=l_o/2$ and $b=A$. Typically, stretching of this type of tissue is initially dominated by un-crimping, or straightening of the fibres, which only requires a small amount of stress. Once the fibres are straightened, they start carrying the tensile stress directly, at which point the tissue stiffens significantly. Because the onset of stiffening is governed by the un-crimping of the fibres, the strain at stiffening, ε_s, can be predicted from the wavelength and amplitude of the crimps. By considering a section of fibres of length L and initially crimped with a wavelength l_o, the strain at stiffening can be written as $\varepsilon_s=(L-2l_o)/2l_o$. For each of the eight cross sections (anterior, mid and posterior locations), several sites within the inner undamaged region of the section were imaged to produce an average ε_s for each of three A-P locations.

2.4.2. Results

2.4.2.1. Collagen fibre & crimp angles

Mean AD-PV collagen fibre angles of the s. compactum for anterior, mid and posterior A-P locations were 54 $\pm$ 1.2 (n=4 sites within inner region of sagittal section), 43 $\pm$ 0.7 (n=5) and 41 $\pm$ 2.6 (n=3) °, respectively (Figure 2.9a). Mean AV-PD fibre angles for anterior, mid and posterior locations were 58 $\pm$ 0.9 (n=4), 50 $\pm$ 1.2 (n=5) and 49 $\pm$ 2.9 (n=3) °, respectively (Figure

2.9a). A pattern of decreasing fibre angle from the head to the tail region of the fish was observed for both AD-PV and AV-PD fibres (Figure 2.9a). At all three A-P locations, AV-PD fibres exhibited a higher fibre angle than AD-PV fibres (Figure 2.9a). Mean ε_s of collagen fibres of the s. compactum for anterior, mid and posterior locations were 31.1 $\pm$ 4.8 (n=4), 25.3 $\pm$ 1.5 (n=7) and 24.5 $\pm$ 1.8 (n=3) %, respectively (Figure 2.9b). A pattern of decreasing ε_s of collagen fibres from the head to the tail region of the fish was observed (Figure 2.9b).

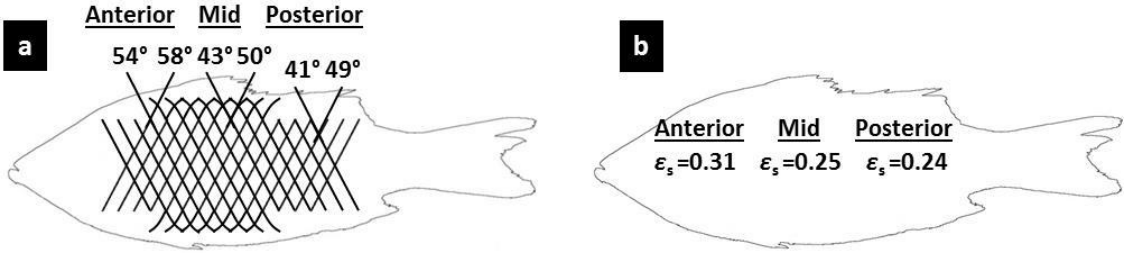

Figure 2.9. (a) Diagram of the cross-helical arrangement of collagen fibres of the s. compactum in striped bass fish skin, including mean anterodorsal-posteroventral (AD-PV) and anteroventral-posterodorsal (AV-PD) collagen fibre angles for anterior, mid and posterior A-P locations; (b) mean ε_s of collagen fibres of the s. compactum for anterior, mid and posterior A-P locations.

CHAPTER 3

TENSILE PROPERTIES OF STRIPED BASS FISH SKIN

3.1. Overview: The tensile properties of teleost fish skin

There are only a few studies on the tensile mechanics of fish scales. Recently, Ikoma *et al*. [54] characterized the structure and tensile mechanics of teleost scales from the red seabream, *Pagrus major*. Torres *et al*. [56] also studied the structure and tensile mechanics of teleost scales, but using thick scales from *A. gigas*. Garrano *et al*. [44] measured the tensile properties of scales from the common carp, *Cyprinus carpio*. Whereas the tensile mechanics of teleost scales have only recently been examined, a larger body of research has been conducted on the tensile properties of intact teleost fish skin and of shark skin. The focus of this thesis with respect to the tensile properties of teleost skin is to investigate the potential mechanical role of the dermal s. compactum layer during locomotion by serving as a whole body exotendon and enhancing swimming efficiency and performance. Therefore, only select articles on the tensile properties of fish skin are reviewed here, which concentrate on the possible exotendon function of the s. compactum. The hypothesized external tendon role of the s. compactum was first proposed for shark skin by Wainwright *et al*. [17]. Wainwright *et al*. [17] based this hypothesis on the mechanical theory of fibre-reinforced cylinders (with cross-helical arrangement similar to the s. compactum) described in Wainwright *et al*. [31]. Wainwright *et al*. [17] performed tensile tests on skin from the lemon shark, *Negaprion brevirostris*, and applied the theory on fibre-wound cylinders [31] to explain the observed tendon-like properties of the skin and the proposed exotendon function of the s. compactum, including how the s. compactum behaves under tensile deformation during undulatory locomotion. However, the precise operation of the s. compactum during swimming (or the exotendon mechanism), and thus how the s. compactum functions as an energy storage device facilitating muscle contraction and reducing the energy required for locomotion, was not completely understood.

Following this seminal paper on the exotendon role of the s. compactum in sharks, one of the co-authors from Wainwright *et al*. [17] continued the examination of the possible external tendon function of the s. compactum, but in two species of teleost fish: the Norfolk spot, *Leiostomus xanthurus*, and the skipjack tuna, *Katsuwonus pelamis*. Hebrank & Hebrank [16] reported collagen fibre angles of the s. compactum in these two teleosts and performed uniaxial and biaxial tensile tests on skin specimens. The researchers suggested that their results, particularly from biaxial tensile tests, were inconsistent with the original s. compactum exotendon hypothesis proposed by Wainwright *et al*. [17] and how the skin should behave under biaxial tension, and therefore that the s. compactum does not function as an exotendon in these two teleosts. Instead, Hebrank & Hebrank [16] suggested that because the s. compactum of teleost skin in comparison to shark skin has evolved to be substantially thinner relative to the thickness of the entire integument, that the s. compactum of teleosts may have lost its ability to store sufficient energy to act as an external tendon during locomotion. Instead, the authors suggested that the s. compactum of teleosts may simply serve a hydrodynamic function by allowing shearing of collagen fibre laminae and preventing wrinkling of the skin during locomotion, thus maintaining a smooth skin surface and improving swimming performance. However, their tensile test results and evidence for a lack of a tendon role of the s. compactum in teleosts were inconclusive, and it is possible that the s. compactum plays such a tendon role in other teleost species.

The next study on potential exotendon effects of the s. compactum was conducted by Naresh *et al*. [61]. Naresh *et al*. [61] performed uniaxial tensile tests on skin specimens from different body locations (anterior and posterior regions) and in different directions (anteroposterior and dorsoventral axes, and diagonal orientations) using skin from the spadenose

shark, *Carcharias laticaudus*. Naresh *et al*. [61] also performed a histological evaluation of the s. compactum from the same body regions and demonstrated patterns of decreased collagen fibre angle, crimping of collagen fibres, and elastin content towards the posterior end of the shark. Similar patterns of decreased collagen fibre angle were previously reported for shark and teleost skin [16, 17, 33]. Different tensile properties were measured for the skin from the two anatomical locations and in the different orientations, and these differences in mechanical properties were explained in terms of structure by the three examined histological features of the s. compactum: the collagen fibre angle, degree of crimping, and elastin content. The tensile test and histology results were consistent with the s. compactum exotendon hypothesis proposed by Wainwright *et al*. [17]. In this thesis, we investigate the exotendon hypothesis by performing tensile tests on skin from the teleost *M. saxatilis* (Chapter 3), in addition to bending experiments on whole *M. saxatilis* fish (Chapter 5). The collagen fibre angle and degree of crimping of the s. compactum are reported for three anteroposterior body locations, and the uniaxial tensile properties of the skin are measured at the same locations and in anteroposterior and dorsoventral directions. First, the results of tensile tests on individual fish scales are reported for striped bass.

3.2. Tensile tests on individual scales

3.2.1. Material & methods

In order to assess the mechanical response of individual scales, we performed tensile tests in hydrated conditions on small tensile samples prepared from individual scales. Whole, fresh striped bass (*Morone saxatilis*) fish were acquired from the local fish store and fish supplier described in Chapter 2 (section 2.4.1.1.), and were kept on ice. Scales were plucked using tweezers and stored in a freezer at -20 °C until tested. Before the test, the scales were removed

from the freezer and put in a water bath for about 5 minutes for thawing, and then cut into small dog-bone-shaped specimens using a multi-tube rotary hole-punch and dissecting scissors. The resulting samples had a gage length of 4 mm, a gage width of 1.5 mm and an average thickness (measured with digital calipers) of about 0.20 mm. Using this technique, samples were cut at 0°, 45° and 90° from the longitudinal direction (anteroposterior axis) of the fish (Figure 3.1).

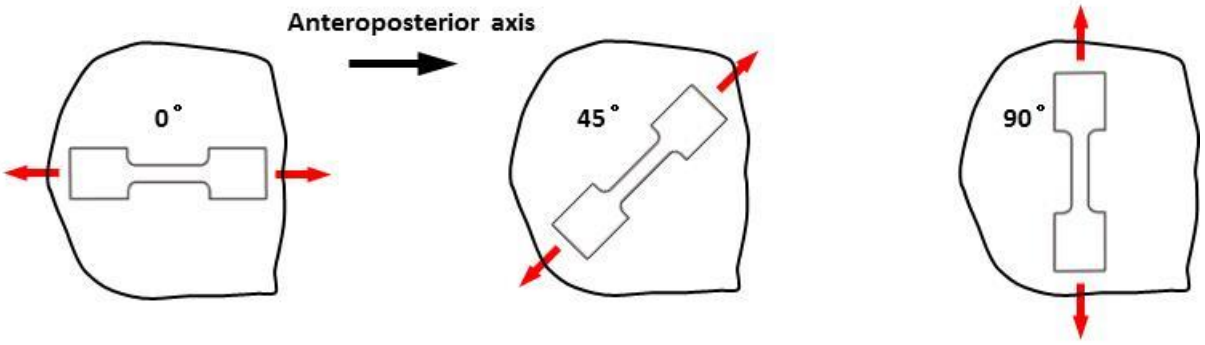

Figure 3.1. Diagram of the dog-bone-shaped specimens dissected from fish scales along 0, 45 and 90° from the longitudinal axis of the fish.

The samples were then mounted on a miniature loading stage (Ernest F. Fullam Inc., Latham, NY), which was placed under an upright, reflected light microscope (BX-51M, Olympus, Markham, Canada) equipped with a CCD camera (RETIGA 2000R, Qimaging, Surrey, Canada) in order to monitor deformations and failure modes of the specimens. All specimens were loaded in tension at a rate of 0.005 mm/s (corresponding to a strain rate of 1.25×10^{-3} s^{-1}) up to complete failure. Images were taken throughout the entire test every 10 seconds using the CCD camera. The images were used to measure the deformation and strain values of the samples using digital image correlation [71] and to monitor failure modes such as debonding of the bony layer and pullout of the collagen fibrils. All samples were kept in hydrated conditions during preparation and testing.

In order to assess the mechanical response of the collagen layer alone, we performed

additional tensile tests on scales with the bony layer removed. The collagen layer was carefully peeled out of the scale which rested on a flat and hard surface. The layered structure of the fish scale makes it easy to "delaminate" with a minimum of force. While the collagen material at the separation site might be partially damaged, the peeling force was deemed insufficient to damage in the rest of the collagen layer and to alter its overall mechanical properties. The remaining 0.05 mm thick collagenous material was tested in tension along the 0°, 45° and 90° directions.

3.2.2. Results

The resulting stress-strain curves from tensile tests on individual scales (Figure 3.2a) display an initial quasi-linear region, with an initial modulus in the 600-850 MPa range. The material softens slightly before reaching a maximum stress of 30-50 MPa (depending on scale orientation), after which the stress drops significantly. Using optical observation, we could associate this sudden decrease in stress to the sudden cracking of the bony layer. Subsequently, the collagen layer progressively detach from the stiff bony layer, while collagen plies tear one after the other, yielding step-like patterns on the stress-strain curve up to total failure at about 40% strain.

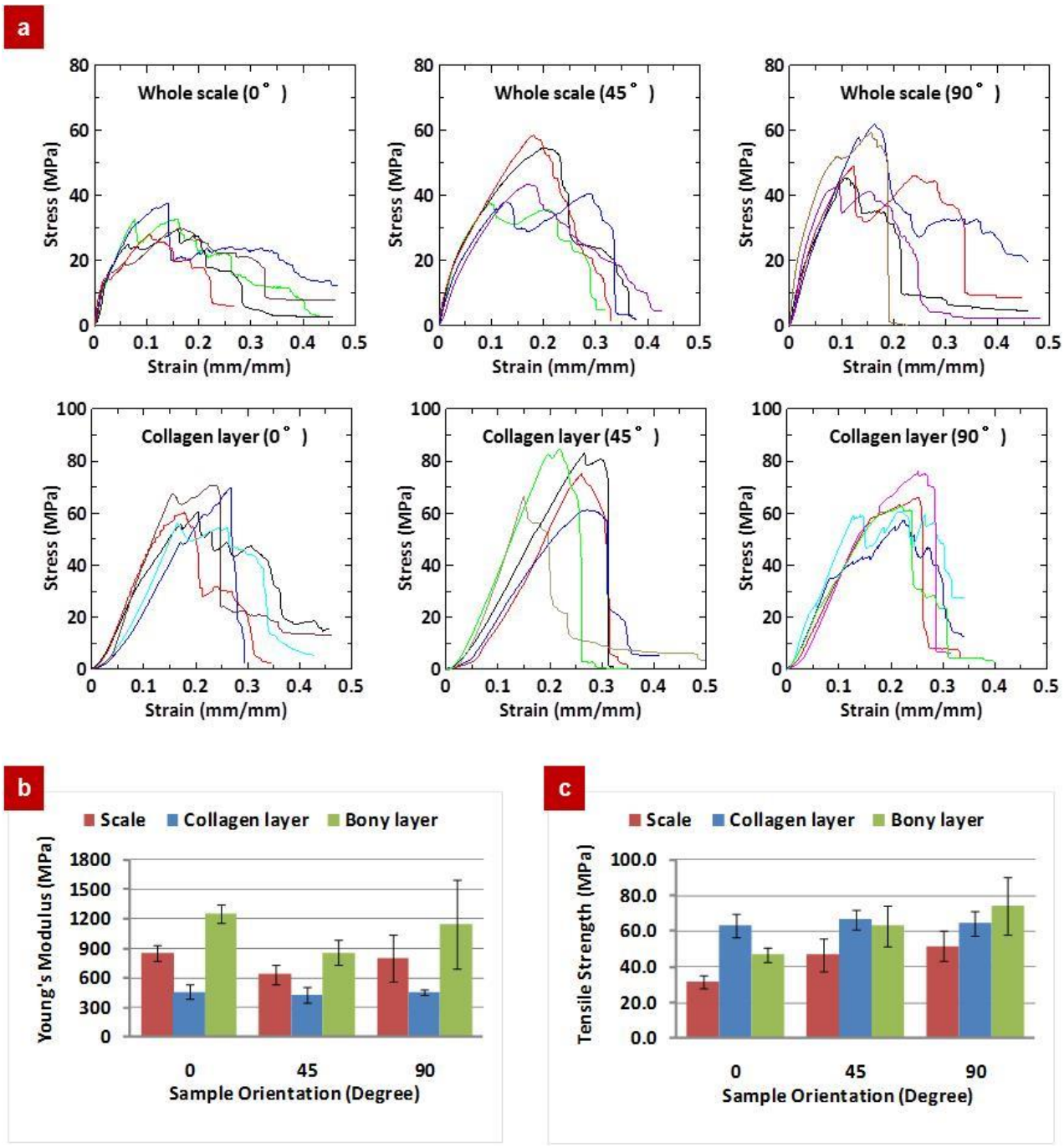

Figure 3.2. (a) Tensile stress-strain curves for fish scales along 0, 45 and 90° from the longitudinal axis of the fish. Summary of results for (b) Young's modulus; (c) strength. The error bars indicate standard deviations.

The stress-strain response of the isolated collagen layer of the scale (Figure 3.2a) displayed a linear regime with a modulus of about 450 MPa, followed by a progressive failure

after a peak stress of 65 MPa. The ultimate strain was the same with and without bony layer. The behavior of the collagen cross-ply is consistent with the behavior of single collagen type I fibrils [72]. Assuming that the fibers do not carry any stress if they are perpendicular to the loading direction, only half of the material actually carries stress in the collagen layer. Since individual collagen fibrils have a Young's modulus of about 1 GPa, a tensile strength of 200 MPa and a strain at failure of 30% [72], the modulus of the 90° ply laminate can be estimated at 500 MPa, its strength at 100 MPa and its strain at failure at 30%. This compares well with our experimental results, showing that the tensile behavior of the collagen layer is largely controlled by the stretching of straight, individual collagen fibrils.

While it was not possible to isolate the bony layer for testing, its properties were inferred from the whole scale and collagen only tensile test results. In the elastic regime, the whole scale behaves like a two-layer, constant strain composite. Since the thickness of the bony and collagen layers is similar, the modulus of the scale is given by:

$$E_S = \frac{1}{2}\left(E_C + E_B\right) \tag{1}$$

where E_C and E_B are the Young's moduli of collagen and bony layers respectively. The modulus of bony layer can then be estimated using:

$$E_B = 2E_S - E_C \tag{2}$$

The strength of bony layer can be evaluated with a similar approach. In the linear regime, with the uniform strain assumption, the stresses in the bony and collagen layers are proportional to their stiffnesses. From the whole scale test, the stress σ_S at which the bony layer fails is known. Just prior to failure the stress in the bony layer is then given by:

$$\sigma_B = \frac{E_B}{E_S}\sigma_S \tag{3}$$

This model assumes that both materials are in the linear elastic range up to the failure of the bony layer. In reality Figure 3.2a shows that the scale softens slightly when loaded in tension, probably due to damage accumulation in the bony layer (collagen behaves linearly over this range of strain). Equation 3 therefore slightly overestimates the actual strength of the bony layer. We used equations (2) and (3) to estimate the modulus and strength of the bony layer. The results show that the bony layer is about twice as stiff as the collagen layer, with about the same tensile strength (Figure 3.2b,c). The bony layer is however more brittle, failing at about 10% strain while the collagen layer fails at strains in excess of 40%. Interestingly, we also found that the whole scale displays in-plane anisotropic properties, but only because of the bony layer; the collagen layer is isotropic in plane in terms of both modulus and strength. This set of experiments highlights the main traits of the scale's components: the bony layer is stiff, hard and brittle because of its high mineral content, while the underlying collagen cross-ply is softer and more deformable, with larger strains at failure.

3.3. Tensile tests on stratum compactum

3.3.1. Material & methods

3.3.1.1. Dissection & specimen collection

The tensile tests on fish skin performed in this chapter also followed a protocol similar to that of [61] in that skin specimens were tested from different locations on the fish and in different directions to explore possible specimen orientation and A-P and D-V location effects on the tensile properties of the skin. The dissection procedure for tensile tests on fish skin started with rinsing the fish with cold water for several minutes and descaling one side of the fish from the lateral line down to the ventrum. The descaled region of the fish was patted dry and lines were

drawn with a marker to outline either six parallel (anteroposterior, A-P) specimens or six perpendicular (dorsoventral, D-V) specimens, as indicated in Figure 3.3. Three parallel specimens were located immediately below the lateral line and the other three parallel specimens were located immediately ventral to the upper three specimens (Figure 3.3a). The rectangular-shaped areas (l x w = 5 x 2 cm) outlined with the marker for either parallel or perpendicular specimens were carved out of the fish's body using a scalpel. The tissue block was immediately dissected to isolate the s. compactum layer and overlying epidermis from the hypodermis and musculature. The prepared specimens were patted dry, sealed in labeled plastic Ziploc bags, and placed in a freezer at -20 °C for preservation until tensile tests were performed.

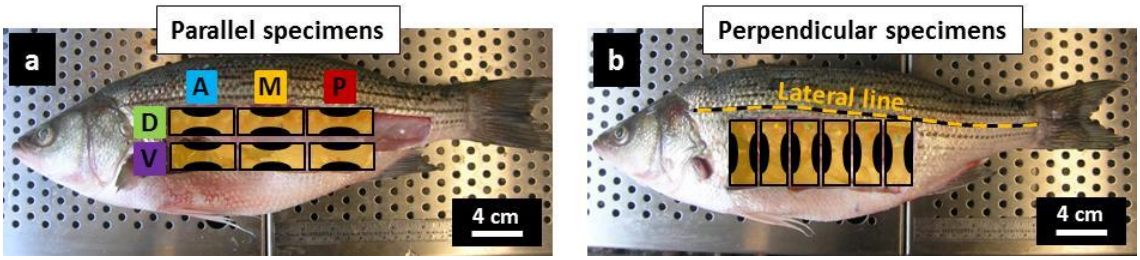

Figure 3.3. Experimental setup for tensile tests on fish skin in both (a) parallel (anteroposterior, A-P) and (b) perpendicular (dorsoventral, D-V) orientations and at different locations on the fish (D or V for parallel specimens, and A, M and P locations for all specimens).

3.3.1.2. Specimen preparation & test procedure

Tensile tests were performed shortly (typically one or two days) following a fish dissection and skin sample collection. Prior to testing, the skin samples, still in plastic Ziploc bags, were thawed in room temperature (*ca*. 20 °C) water for approximately 30 min. The skin specimens were then removed from the sealed bags and submerged in room temperature water for at least 15 min before tests. Using Teflon sheet, a stencil or template (adapted from [73]), had been previously constructed for producing dumbbell-shaped specimens for tensile tests on fish skin (Figure 3.4a).

The stencil and thus the dumbbell-shaped skin specimens had a gauge length and width of 1 cm and 0.2 cm, respectively (Figure 3.4a). The thickness of the gauge region was measured for each specimen using digital calipers. The mean gauge thickness for all specimens (n=69) was 0.234 $\pm$ $2.28 \cdot 10^{-3}$ mm. All mean values reported are followed by the standard error of the mean ($\pm$ s.e.). A speckle pattern of marker dots was applied to the inner (s. compactum) surface of the specimen to measure strain accurately using image analysis (Figure 3.4b).

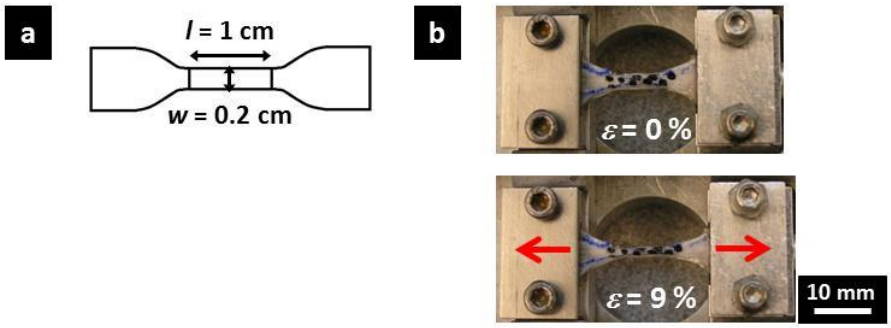

Figure 3.4. (a) Diagram of the dumbbell-shaped stencil used for tensile tests (adapted from [73]); (b) typical fish skin tensile test specimen at zero and maximum strain.

The skin specimens were then mounted on a miniature loading stage (Ernest F. Fullam Inc., Latham, NY, USA) with the embedded portion of the specimen well-secured within the clamps using abrasive paper (no slippage from the grips occurred during tests and all specimens failed within the gauge region). The specimens were pre-loaded with a small force (0.1 N) at a low extension rate to remove any slack before load and extension values were zeroed. The specimens were then stretched at a rate of 0.005 $mm \cdot s^{-1}$ (corresponding to a strain rate of *ca*. 5.0 x 10^{-4} s^{-1}) until complete failure. Images were taken throughout the test every 0.5 mm extension and more rapidly towards the end of the test to obtain an image of the specimen immediately

before failure. Special care was taken to keep the specimens hydrated throughout the preparation steps, during the mounting procedure and during the tests.

For all tensile test specimens (parallel and perpendicular at all anatomical locations), the stress (σ, MPa) was calculated as force / initial cross-sectional area, where cross-sectional area was computed as the product of the width and thickness of the gauge region of the specimen. Image analysis and strain measurements were performed using ImageJ version 1.46r (http://rsb.info.nih.gov/ij/). At high magnification, the gauge region of the specimen at zero strain (first image) was examined. Two distinct ink dots from the speckle pattern were selected at both ends of the gauge region and along its midline. A line was drawn connecting the two marks and the length of the line measured in pixels. The final image of the specimen (immediately prior to failure), was also examined at high magnification. The same two ink dots were located, a line drawn to connect the marks, and the length measured in pixels. The strain of the gauge region was then calculated as change in length (pixels) / initial length (pixels).

3.3.1.3. Data analysis (tensile property calculations)

Several material properties were calculated from the stress-strain curves (Figure 3.5). The tangent modulus was computed as the slope of the stress-strain curve. The tangent modulus was initially low for all curves and increased to a maximum value as the fibre angle decreased. Following this stage, the tangent modulus decreased slightly, an indication of damage in the overextended tissue. The modulus for each specimen (E, MPa) was taken as the maximum value of the tangent modulus. The point of maximum tangent modulus was located on the stress-strain curve, and the tangential line at that point was extended to intersect the horizontal axis, thus defining a strain value which we took as the strain at stiffening (ε_s, mm/mm). ε_s was directly

obtained by the equation, $\varepsilon_s = (-\sigma_E / E) + \varepsilon_E$, where ($\varepsilon_E$, σ_E) are the coordinates of the point of maximum tangent modulus and E the tangent modulus at that point (i.e. the modulus of the material). Finally, the strength of the tissue was simply taken as the maximum stress, σ_{max}.

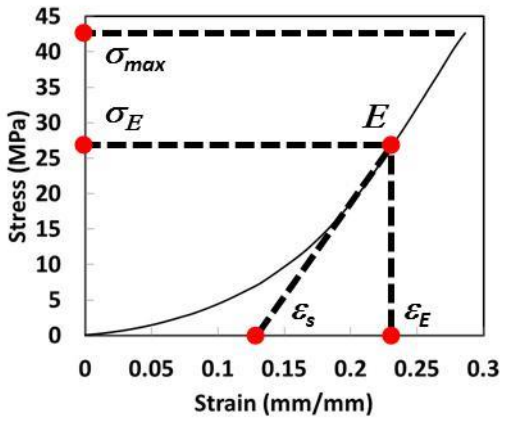

Figure 3.5. Diagram showing the calculation of tensile properties, including maximum tangent modulus (E), maximum stress (σ_{max}), stress at maximum tangent modulus (σ_E), strain at maximum tangent modulus (ε_E), and strain at stiffening (ε_s).

3.3.2. Results

3.3.2.1. Stress-strain curves for parallel specimens

The resulting stress-strain curves from tensile tests on parallel (A-P directed) specimens are shown in Figure 3.6. Parallel specimens were prepared from three different fishes (N=3), with n=11, n=10, and n=12 skin specimens dissected from the three fishes (all data plotted in Figure 3.6). As expected for tissues made of crimped fibres, the tissues are initially soft, and stiffen at larger strains as the fibres straighten and align along the direction of loading (Figure 3.6). The three fish samples all exhibited a similar range or spread of stress-strain curves. However, marked differences were observed when the stress-strain results were examined for possible A-P and D-V location effects. Parallel specimens from the posterior region exhibited notably stiffer

and stronger tensile responses compared to specimens from the anterior region, while mid-region specimens displayed intermediate results (Figure 3.6a). Similarly, a strong effect of D-V location was also observed, with dorsal specimens displaying stiffer and stronger responses (Figure 3.6b).

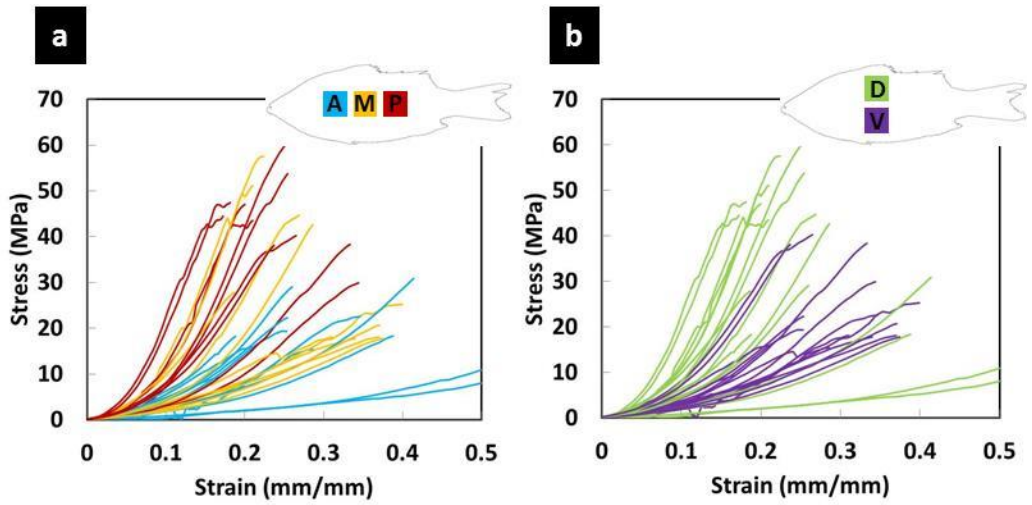

Figure 3.6. (a) Stress-strain curves for tensile tests on striped bass (N=3) fish skin in the parallel orientation (n=33) color-coded for anteroposterior (A-P) location; (b) stress-strain curves for parallel specimens coded for dorsoventral (D-V) location.

3.3.2.2. Tensile properties vs. location correlations

The effects of A-P and D-V location on the σ_{max}, E and ε_s of parallel specimens are shown in Figure 3.7a-c. Strong positive linear correlations were found between σ_{max} and A-P location for both dorsal (R=0.81) and ventral (R=0.80) specimens, with dorsal specimens displaying elevated σ_{max} values (Figure 3.7a). Similarly, strong positive correlations were determined between E and A-P location for both dorsal (R= 0.73) and ventral (R= 0.61) specimens, with dorsal specimens showing increased E values (Figure 3.7b). A strong negative correlation (R=0.66) was found between ε_s and A-P location for dorsal specimens (Figure 3.7c). A weak positive correlation

(R=0.30) was found between ε_s and A-P location for ventral specimens, which is excluded from Figure 3.7 and explained by Figure 3.8.

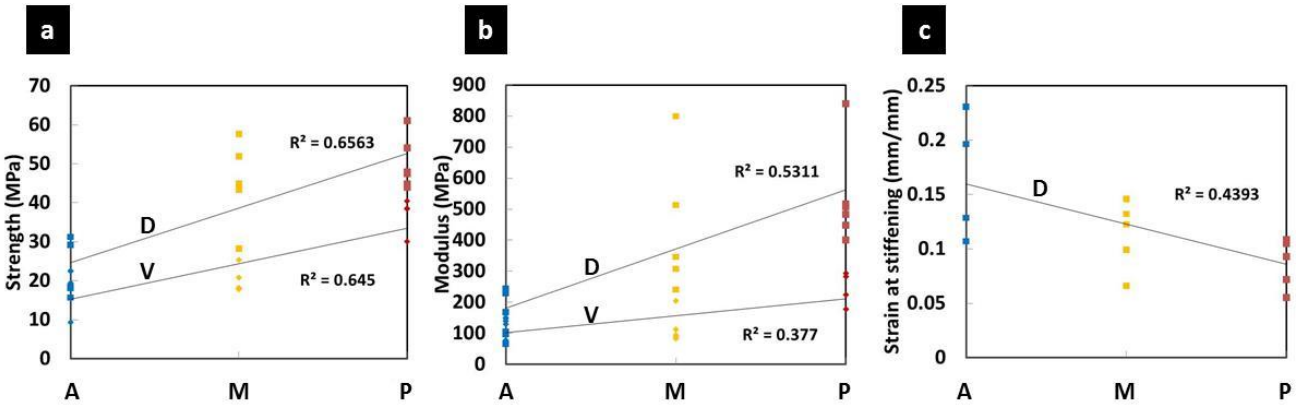

Figure 3.7. (a) Strong positive linear correlations between σ_{max} and A-P location for both dorsal and ventral specimens; (b) strong positive correlations between E and A-P location for both dorsal and ventral specimens; (c) strong negative correlation between ε_s and A-P location for dorsal specimens.

3.3.2.3. Tensile property maps

The effects of A-P and D-V location on the stress-strain results of parallel specimens are further demonstrated in Figure 3.8, which plots mean σ_{max}, E and ε_s of parallel specimens from all locations. The number of parallel specimens dissected from the anterior, mid and posterior locations of the three fishes were n=6, n=5 and n=6, respectively, for dorsal specimens, and n=6, n=6 and n=4, respectively, for ventral specimens. Standard two-tailed, unpaired two-sample Student's t-tests assuming unequal variances were employed to compare the mean values reported for the tensile tests. The mean σ_{max} and E of posterior specimens were significantly higher than those of anterior specimens for both dorsal and ventral specimen types ($p < 0.05$) (Figure 3.8a,b). The mean ε_s of posterodorsal specimens was lower than that of anterodorsal specimens ($p = 0.066$) (Figure 3.8c).

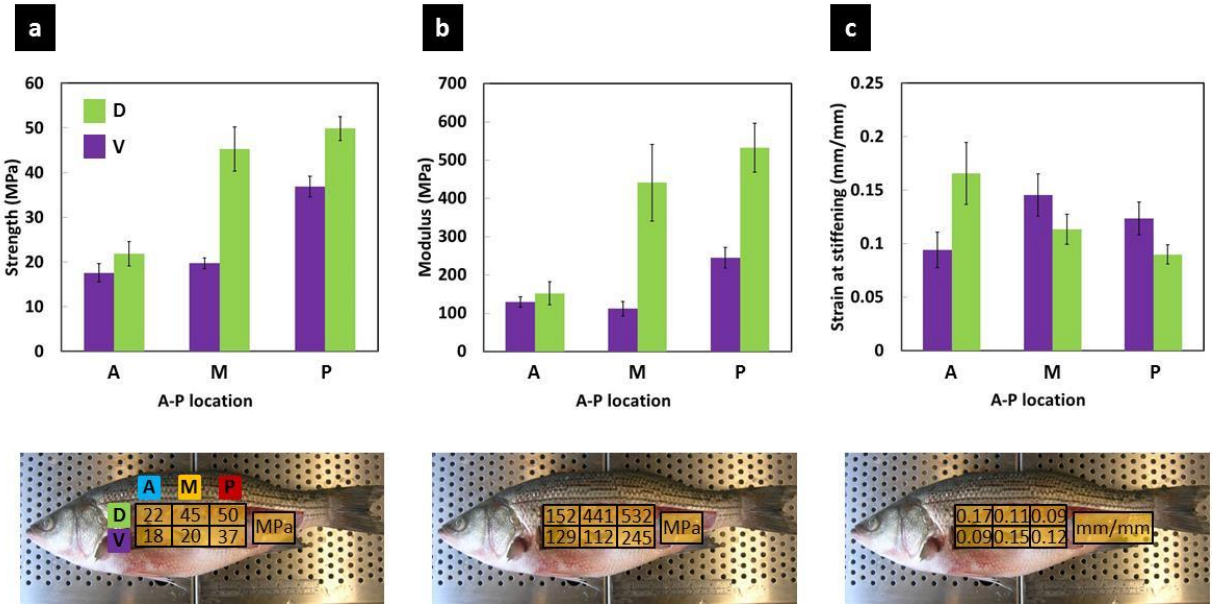

Figure 3.8. Mean ± s.e. (a) σ_{max}, (b) E and (c) ε_s of parallel specimens from all anteroposterior (A-P) and dorsoventral (D-V) locations.

3.3.2.4. Stress-strain curves for perpendicular specimens

The results of all tensile tests on specimens dissected in parallel (A-P) and perpendicular (D-V) directions are included in Figure 3.9a. Perpendicular specimens were prepared from three different fishes (N=3), with n=12 skin specimens dissected from each of the three fishes (all data plotted in Figure 3.9). Clear differences were observed between the stress-strain curves of parallel versus perpendicular specimens, with perpendicular specimens exhibiting notably stiffer and stronger results, and a lower ε_s (Figure 3.9a). The mean σ_{max} and E of perpendicular specimens were significantly higher than those of parallel specimens ($p < 0.05$) (Figure 3.9c,d), whereas perpendicular specimens exhibited a significantly lower ε_s ($p < 0.05$) (Figure 3.9e). No A-P location effects were determined for perpendicular specimens (Figure 3.9b), which displayed a narrower range of stress-strain results than parallel specimens (Figure 3.9a).

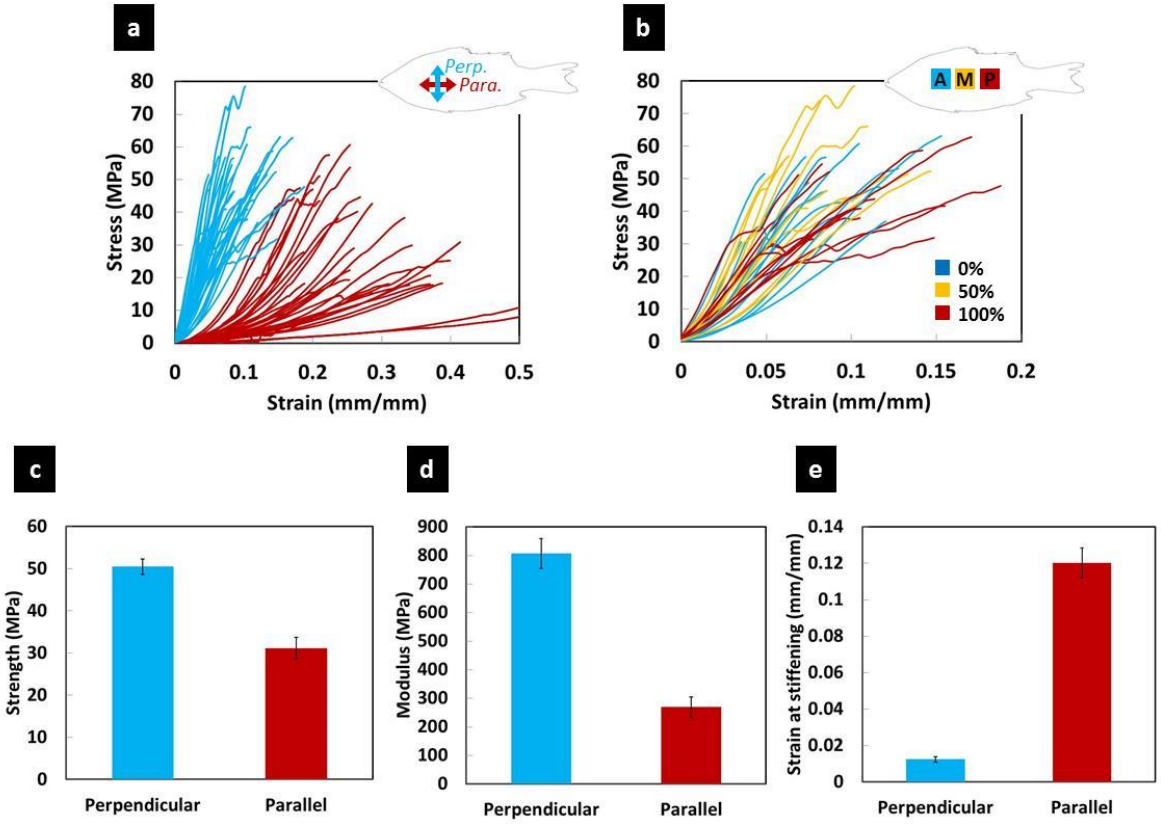

Figure 3.9. (a) Stress-strain curves for tensile tests on striped bass fish skin in parallel (N=3 fishes, n=33 specimens) and perpendicular (N=3 fishes, n=36 specimens) orientations; (b) stress-strain curves for perpendicular specimens color-coded for anteroposterior (A-P) location; mean $\pm$ s.e. (c) σ_{max}, (d) E and (e) ε_s of parallel versus perpendicular specimens.

3.4. Discussion

Overall, the tensile results demonstrated that the σ_{max} and E of perpendicular specimens exceeds that of parallel specimens while ε_s is lower, and that parallel specimens exhibit location effects with posterodorsal specimens displaying the highest E and σ_{max}, and lowest ε_s. From histology, it was shown that both AV-PD and AD-PV directed fibres of the s. compactum exhibit a pattern of decreased collagen fibre angle towards the tail region, with AV-PD fibres exhibiting higher fibre angles. In addition, it was shown that the ε_s of collagen fibres also decreases towards the posterior region. Similar results were found by Naresh *et al.* [61] for shark skin, that is, they

determined patterns of decreased collagen fibre and crimp angle towards the caudal region. As suggested by Naresh *et al*. [61] and in support of the original s. compactum exotendon hypothesis [17], the mechanical properties of the skin, which are dominated by the properties of the s. compactum that composes the majority of the integument, may be controlled primarily by the collagen fibre and crimp angles of the s. compactum. These two variables, along with elastin content, were proposed by Naresh *et al*. [61] to be the strongest factors influencing the measured tensile properties of the skin, including the observed specimen location and orientation effects. Our results for striped bass also suggest that the tensile performance of the skin is determined by A-P and D-V location and thus by local histological features that vary along these axes, including collagen fibre angle and ε_s of collagen fibres. The lower tensile ε_s of parallel specimens from the posterodorsal region compared to the anterodorsal region may be explained by the lower collagen fibre angle and ε_s of collagen fibres measured for this area of the skin, as the fibres would be expected to align with the axis of force and become less crimped at a lower strain, thus resulting in earlier stiffening. The higher E and σ_{max} of both dorsal and ventral specimens from the posterior region compared to the anterior region may be explained by recruitment of collagen fibres. That is, a higher total number of collagen fibres may be recruited and align with the axis of force before failure of the fibres that were first aligned occurs (assuming all fibres do not align uniformly), which would result in higher E and σ_{max} due to a greater number of collagen fibres being loaded before failure. Similarly, the lower ε_s of perpendicular specimens versus parallel specimens may be explained by their lower fibre angles relative to the axis of force, and the higher E and σ_{max} values by increased recruitment of collagen fibres before failure.

In addition, although the tensile ε_s of parallel specimens and the ε_s of collagen fibres from histology both displayed the predicted trend of decreased ε_s towards the posterior region of the fish, it was observed that the tensile ε_s values were notably lower than the corresponding collagen fibre ε_s values. The tensile ε_s of parallel specimens ranged from 17% in the anterodorsal region to 9% in the posterodorsal region, whereas the ε_s of collagen fibres ranged from 31% in the anterior region to 24% in the posterior region. However, the mean ε_E of parallel specimens ranged from 29% in the anterodorsal region to 15% in the posterodorsal region. Although ε_s and ε_E mirror one another and follow the same pattern of decreased magnitude towards the posterior region, the ε_E values are closer in magnitude to the ε_s of collagen fibres from histology. The close correspondence between the ε_E of parallel specimens along the A-P axis and the ε_s of collagen fibres along the A-P axis suggests that the significant stiffening observed near the end of the stress-strain curve is, as predicted, a result of un-crimping of collagen fibres in conjunction with alignment of the fibres along the axis of force. Therefore, the anisotropic (direction-dependent) tensile properties of striped bass fish skin from different anatomical locations are explained well by local structural features of the s. compactum, including collagen fibre angle and ε_s. The tensile properties of the skin in the A-P direction are most physiologically relevant to fish locomotion as this is the natural direction of stretching on the convex side of the fish during swimming. Regardless of A-P location, the collagen fibre angle of the s. compactum always exceeds 45° and the lamellae always exhibit a degree of crimping, and thus these structural attributes generate an initial compliant tensile response followed by significant stiffening, with the E, σ_{max} and ε_s dependent on the local collagen fibre angle and ε_s. These tensile properties are necessary for the s. compactum of striped bass skin to function as an exotendon at a late stage in the locomotory

cycle, and support the s. compactum exotendon hypothesis for striped bass skin, which is further explored in Chapter 5 using whole fish bending tests with disruption of the s. compactum.

CHAPTER 4

PUNCTURE PROPERTIES OF STRIPED BASS FISH SKIN

4.1. Overview: The puncture resistance of teleost fish skin

Nature increasingly serves as a model and inspiration to scientists and engineers, and biomimetics has the potential to lead to novel engineering materials and systems with new combinations of properties, multi-functionalities, adaptability and environmental sustainability. In particular, there is a growing interest in examining how animals evolve protective systems against predators or other mechanical threats [59, 74]. The scaled skin of fish is a 500 million-year-old protective system, with many attributes which would be desirable in personal protective systems: it is ultrathin, flexible, light weight, transparent, breathable, and can resist puncture from collision with obstacles or other fish, or from attacks by predators [8]. The research presented here on the mechanical properties of both individual fish scales and intact fish skin has revealed the adaptive mechanisms at different length scales producing the high protective capacity of this natural material against sharp penetration.

There are only a few studies on the puncture mechanics of fish scales. Bruet *et al*. [15], using nanoindentation and examining energy dissipative mechanisms of the multilayered scale, showed how the primitive ganoid scales from the gray bichir, *Polypterus senegalus*, are optimized to resist penetration. Also, Meyers *et al*. [59] studied the penetration resistance of thick teleost scales from *Arapaima gigas* and showed that these scales can resist bites from predator pirahnas, *Pygocentrus natteri*. Although these other recent studies have investigated the penetration resistance of ganoid and teleost scales, the results reported here are the first to reveal specialized mechanisms of puncture resistance in both individual teleost scales and whole teleost skin using striped bass, *Morone saxatilis*, as a model species. The main findings for intact teleost skin supported the model of teleost fish scale interaction upon puncture proposed by Vernerey & Barthelat [65]. Similar mechanisms of scale interaction, but upon whole predator bite and

encompassing the entire circumference of the fish, in contrast to individual tooth-scale interaction [15, 59], have been investigated using the ganoid fish *P. senegalus* [28].

In this chapter, we have first studied the structure and mechanics of modern teleost fish scales, which have received relatively little attention in the past [15, 54, 56, 75, 76]. This type of scale displays interesting combinations of flexibility, strength, resistance to penetration, light weight and transparency. Teleost scales have excellent hydrodynamic properties [26, 27] and provide a protective layer resisting penetration [15, 53, 57]. Currey, in a review article on mineralized tissues, noted that some fish scales are so tough that they cannot be easily fractured even after immersion in liquid nitrogen [25]. In an effort to better understand this natural system, a number of recent articles have focused on the structure and mechanics of individual fish scales, which was also the focus of Chapter 3. Tensile tests, including those reported in Chapter 3, have revealed the scale's capability to absorb large deformation and energy, associated with progressive failure mechanisms [44, 54, 56]. In this chapter, sharp puncture tests are employed in order to measure the force required to completely defeat the scale using a sharp needle. The high puncture resistance of teleost fish scales from striped bass is demonstrated, and explained by a two-step failure associated with the bony and collagen layers of the scale.

We now have a good understanding of the structure and mechanisms associated with the deformation, fracture and puncture of the three major fish scale types (teleost, cosmoid and ganoid) as individual components. However, the protective layer provided by natural fish skin consists of many scales, and while the structure and scalation or squamation patterns of various fish scales is now well documented [8, 46, 77], little is known on how scales interact to generate high resistance to puncture. The mechanical interaction between teleost scales upon puncture or bending of the fish was modeled by Vernerey & Barthelat [65] and suggests that interaction

between the scales can enhance both penetration resistance and locomotion by increasing flexural stiffness, providing an exotendon effect during swimming as well as dispersing puncture force and preventing unstable localized deformation during puncture. More recently, Browning *et al*. [78] studied scale-scale interactions during puncture using a two-dimensional polymer model of elasmoid scales, revealing useful mechanisms and properties associated with the scalation pattern. In this chapter, we report, for the first time, insights into collaborative mechanisms between scales during a puncture event on natural fish skin. The main goal of this work was to identify key mechanisms and parameters controlling the puncture resistance of fish skin, in order to ensure an efficient biomimetic "transfer of technology" to synthetic flexible protective systems.

4.2. Puncture tests on individual scales

4.2.1. Material & methods

Adult striped bass have a few natural predators, including various aquatic birds, marine mammals, and potentially large pelagic fishes and sharks [6]. Juvenile striped bass are known to have several sources of predation including bluefish (*Pomatomus saltatrix*) and cannibalism [6]. The main function of the scales is mechanical protection against predators [15, 53, 57] and, in particular, the scale must be capable of preventing sharp objects such as teeth [7] from completely penetrating the skin and reach the softer and more fragile underlying tissues. A sharp tooth concentrates the biting force over a very small area on the scale, which leads to severe contact stresses. We have assessed the resistance to penetration of single striped bass scales (larger ctenoid scales from the mid-lateral body region) using an experimental setup that simulates a predator's bite using the same miniature loading stage described above in the tensile tests. A sharp steel needle (tip radius=25 μm) was used to simulate a predator's tooth (bluefish,

for example, have teeth of a shape similar to a needle and a radius smaller than 250 μm). The needle was driven through a scale resting on a silicone rubber substrate (E~1.8 MPa measured by spherical indentation) used to simulate the soft dermis and tissues underlying the scale, at a speed of 0.005 mm/s while the force was recorded (Figure 4.1).

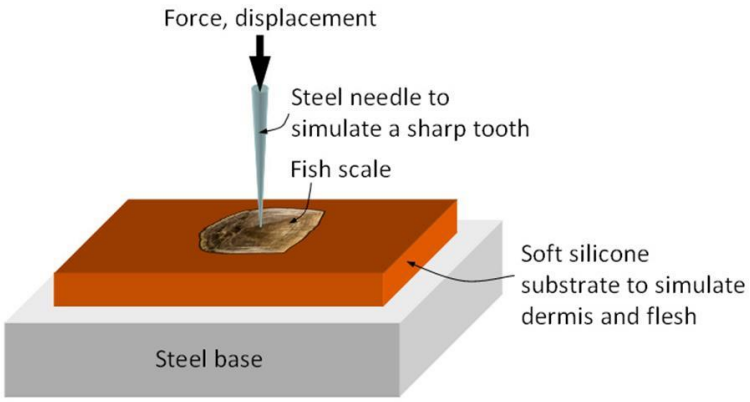

Figure 4.1. Experimental setup for puncture tests on individual scales.

For comparison, we also performed puncture tests on the isolated collagen layer of the scale and on thin polystyrene (PS) and polycarbonate (PC), which are modern engineering polymers typically used when light weight, stiffness, strength, optical translucence and impact resistance are required (their applications include CD cases, biomedical equipment such as petri dishes, and protective gear such as safety glasses or squash goggles). For proper comparison we prepared 10 mm diameter disks of these polymers, and we adjusted the thickness so the areal density (the mass per unit area of protective material) of the protective layer was then same for fish scale, PC and PS.

4.2.1.1. Analytical "four flaps" model

A simplified analytical model was derived to capture the progressive deflection of the four flaps and the retaining membrane effect provided by the underlying collagen layer (Figure 4.2).

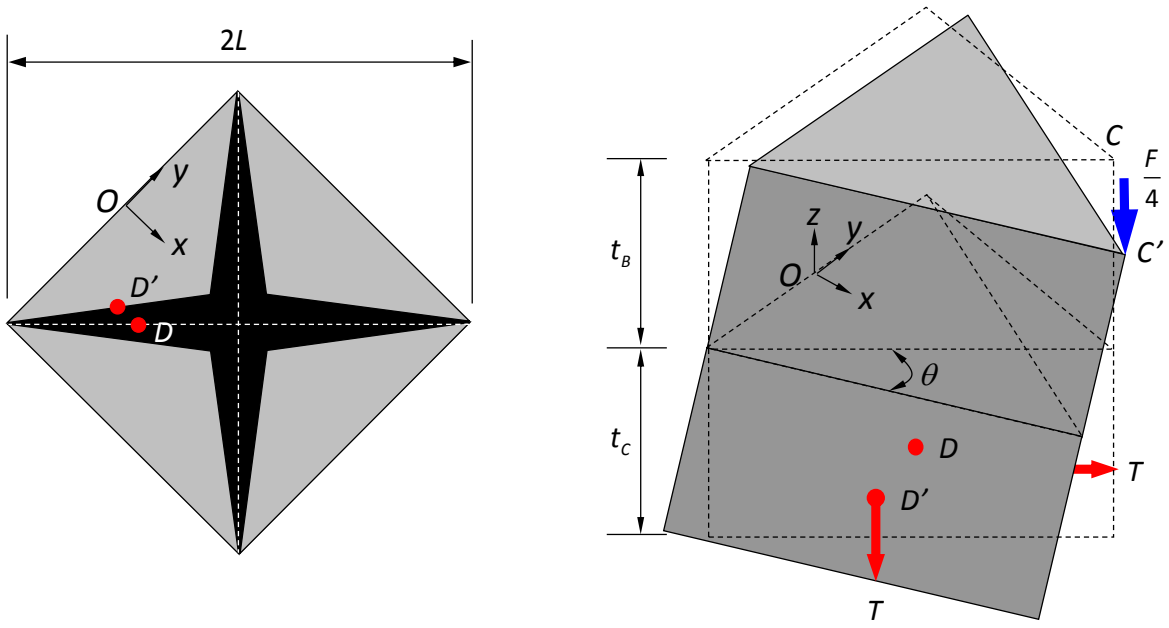

Figure 4.2. Schematic diagram of the deformation and force in the four flaps model.

A.1. Strain

The strains in the collagen were determined by tracking the displacement of the point in the centroid of the section of collagen (point D). Upon deflection of the flap point D moves to D', so that its displacement vector can be written, in the Cartesian system *xyz* (Figure 4.2):

$$\vec{DD'} = \begin{vmatrix} \frac{L}{2\sqrt{2}}(\cos\theta - 1) - \frac{t_C}{2}\sin\theta \\ 0 \\ -\frac{L}{2\sqrt{2}}\sin\theta - \frac{t_C}{2}(\cos\theta - 1) \end{vmatrix} \quad \text{(A.1)}$$

Any fiber crossing the cracks will extend by a distance (using scalar product to project $\vec{DD'}$ on the unit vector collinear to *T*):

$$\begin{bmatrix} \frac{L}{2\sqrt{2}}(\cos\theta-1)-\frac{t_C}{2}\sin\theta \\ 0 \\ -\frac{L}{2\sqrt{2}}\sin\theta-\frac{t_C}{2}(\cos\theta-1) \end{bmatrix}\cdot\begin{bmatrix} -\frac{1}{\sqrt{2}} \\ \frac{1}{\sqrt{2}} \\ 0 \end{bmatrix}=\frac{L}{4}(1-\cos\theta)+\frac{t_C}{2\sqrt{2}}\sin\theta \tag{A.2}$$

The collagen is detached from the bony layer in the puncture area, which leads to the assumption that the tensile strain in the collagen is uniform and equal to:

$$\varepsilon_C=\frac{1}{2}(1-\cos\theta)+\frac{t_C}{L\sqrt{2}}\sin\theta \tag{A.3}$$

Interestingly, the geometry and kinematics for the system is such that the strain in the collagen layer is equi-biaxial and uniform in the puncture site. Knowledge of strain in the collagen layer leads to stress, using the modulus found from the tensile tests (E=500MPa).

A.2. Deflection of the flaps

Similarly, point C at the upper tip of the flaps moves to C' upon deflection, and

$$C\vec{C}'=\begin{vmatrix} \frac{L}{\sqrt{2}}(\cos\theta-1)+t_B\sin\theta \\ 0 \\ -\frac{L}{\sqrt{2}}\sin\theta+t_B(\cos\theta-1) \end{vmatrix} \tag{A.4}$$

The deflection at the loading point is then the z component of $C\vec{C}'$:

$$\delta=\frac{L}{\sqrt{2}}\sin\theta-t_B(\cos\theta-1) \tag{A.5}$$

A.3. Force

Under the concentrated force *F/4*, the rigid bony flap rotates along the y axis and the loading location changes from *C* to *C'*. The force vectors acting on the bony and collagen layers are:

$$\vec{F} = \begin{bmatrix} 0 \\ 0 \\ -F/4 \end{bmatrix} \qquad \vec{T} = \begin{bmatrix} \frac{T}{\sqrt{2}} \\ \frac{T}{\sqrt{2}} \\ 0 \\ \end{bmatrix} \tag{A.6}$$

As the cross product of the vectors $O\vec{D}'$ and $\vec{T}$ is equivalent to half of the cross product of the vectors $O\vec{C}'$ and $\vec{F}$, then we get the force retained by the collagen layer as follows:

$$F = 2Lt_C\sigma_C\left(\frac{\sqrt{2}\tan\theta + 2\frac{t_C}{L}}{1+\sqrt{2}\frac{t_B}{L}\tan\theta}\right) \tag{A.7}$$

Normalized by the square of the scale thickness *t* and the tensile strength of collagen σ_C:

$$\frac{F}{\sigma_C t^2} = 2\frac{L}{t}\frac{t_C}{t}\left(\frac{\sqrt{2}\tan\theta + 2\frac{t_C}{L}}{1+\sqrt{2}\frac{t_B}{L}\tan\theta}\right) \tag{A.8}$$

A.4. Force generated by flexural stresses at the hinges

Assuming that the entire thickness of the bony layer undergoes plasticity, the bending moment transmitted is calculated as follows:

$$M = \sqrt{2}L\left(\frac{t_B}{2}\right)^2\sigma_B \tag{A.9}$$

The force applied by the needle is balanced by this moment:

$$\frac{L}{\sqrt{2}}\frac{F}{4} = M \tag{A.10}$$

Combining equations (A.9) and (A.10), we get the force generated by flexural stresses at the hinges:

$$F = 8\left(\frac{t_B}{2}\right)^2 \sigma_B \tag{A.11}$$

4.2.2. Results

The load-deflection curves resulting from puncture tests on individual scales were highly repeatable throughout all tested samples, with a slight force drop at about 2 N and a maximum penetration force of 3-3.5 N (Figure 4.3). As well, remarkably, the fish scale provided a significantly higher resistance to puncture compared to the high performance engineering polymers, polycarbonate and polystyrene (Figure 4.3).

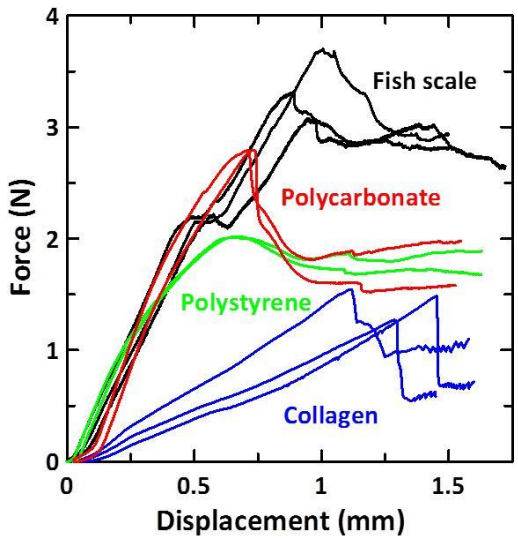

Figure 4.3. Typical results for striped bass scales with and without bony layer. Results for polystyrene and polycarbonate are also shown for comparison.

Finally, we performed additional puncture tests on scales with the bony layer removed. The isolated collagen layer was easily penetrated, providing only half of puncture resistance in terms of force. The bony layer is therefore an important component of the system, operating in synergy with the collagen layer to increase the performance of individual scales. The fish scale

followed a sequence of mechanisms that was highly repeatable from scale to scale as well as across locations on a given scale. The penetration curves consist of three distinct stages that we investigated in detail by imaging of the puncture site at different points on the penetration curve (Figure 4.4). Stage I is the initial linear region, which is dominated by flexion of the entire scale and by damage and indentation of the surface of the bony layer. At a force of about 2 N, the force drops slightly, which we associated to the sudden cracking of the bony layer. Bony and collagen layers have the same thickness, but since the bony layer is stiffer, the neutral plane of the scale lies within the bony layer. As a result, flexural deformations generate tensile stresses in the lower side of the bony layer. Once these stresses reach the tensile strength of the bony layer, cracks initiate at the collagen/bone interface and rapidly propagate towards the surface of the bony layer. Interestingly, the patterns of the flexural cracks always followed a cross pattern, whose orientation invariably followed the orientation of the local radii and circuli (Figure 4.4c) and underlying collagen fibrils. The microstructure of the bony layer therefore induces the failure of the bony layer along specific directions. Upon cracking of the bony layer, four "flaps" of bony material immediately deflect downwards, generating circumferential cracks. At this point, the underlying collagen layer, while remaining intact, detaches from the bony layer over a ring-like area observable with an optical microscope (the scale, while opaque to electrons, is transparent to visible light). The cracking of the bony layer marks the beginning of stage II, dominated by further flexion of the scale, opening of the cross cracks as the four "flaps" of bony material are bent towards the collagen layer, radial propagation of the cross cracks, and further delamination between collagen and bony layers. Eventually the deflection and opening of the flaps are sufficient to let the needle reach the collagen layer and completely puncture it (stage III). The initial failure of the collagen layer indicates the beginning of stage III, and the sharp drop in

force at this point suggests that the failure is rapid, possibly because the collagen layer is stretched. Throughout the rest of stage III, the scale is deflected by the needle, the delamination between collagen and bony layers propagates more extensively, and the radial cracks continue to grow.

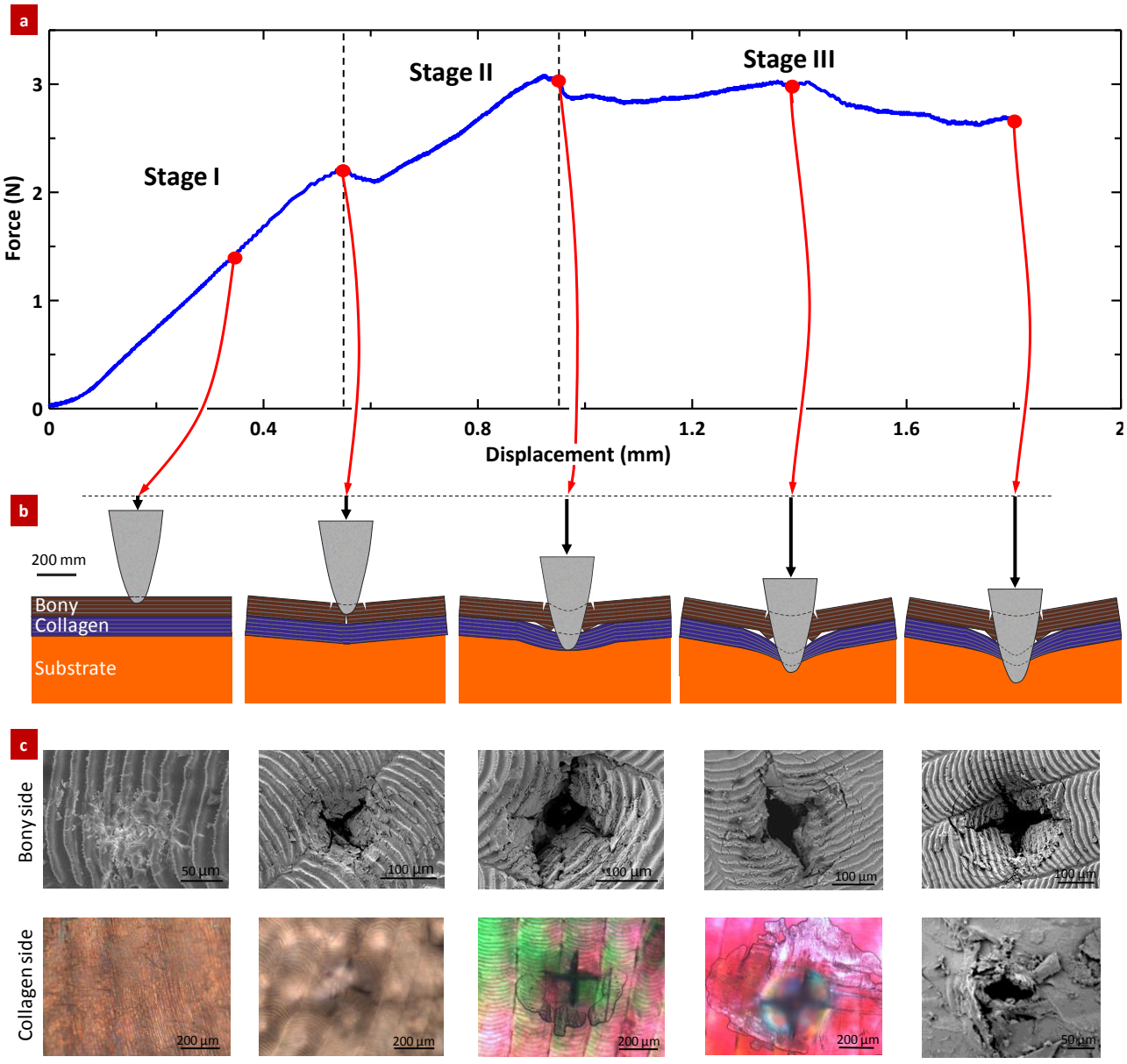

Figure 4.4. Detailed sequence of a puncture test. (a) Load-displacement curve showing three distinct stages; (b) associated mechanisms and (c) imaging. The images of the bony side and the last one of the collagen side were obtained by scanning electron microscopy (SEM), while the first four images of the collagen side were taken with an optical microscope.

4.3. Puncture tests on groups of scales

4.3.1. Material & methods

4.3.1.1. The puncture performance of striped bass fish skin

Although it is believed that the scaled skin of fish has multiple functions [8], its primary role is probably protection against predators [8, 15, 59, 74]. To assess the effectiveness of scales, we therefore performed puncture experiments on whole fish skin to duplicate a predator's attack using striped bass (*M. saxatilis*), a common teleost fish originating from the northern Atlantic Ocean. The specimens we used for this work were acquired from the local fish store and fish supplier described in Chapter 2 (section 2.4.1.1.). A half-striped bass was placed in immersed condition and a sharp needle (tip radius=35 μm) mounted on a universal testing machine was driven through the skin (Figure 4.5). Tests were performed on fully scaled (natural, intact) fish as well as on entirely descaled fish for comparison.

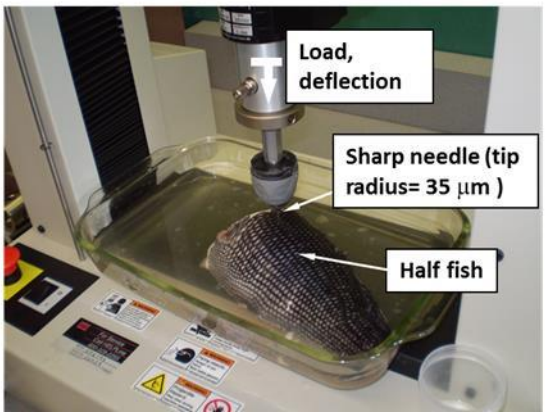

Figure 4.5. Experimental setup for puncture tests on a half-striped bass.

4.3.1.2. Effect of substrate stiffness

The deflection and deformation of the scales is largely controlled by the stiffness of the underlying substrate, but it is not clear whether the substrate affects their puncture resistance.

More generally, the question of whether the structure and mechanics of fish scales have evolved in relation to the properties of the underlying tissue must be assessed for a proper biomimetic transfer to synthetic systems. In this section, we have investigated this question for natural fish, using puncture tests on individual fish scales resting on elastomeric substrates with different stiffnesses. Three substrates covering a wide range of stiffness were considered: a soft silicone rubber, a hard silicone rubber, and natural fish substrate dissected from striped bass consisting of the dermis (specifically descaled skin) and underlying muscle (which is likely less stiff than the activated musculature in living fish). These materials were cut into 2.5 x 2 x 1.5 cm blocks which served as substrate for puncture tests on the individual fish scales. The elastic properties of each of these substrates were measured by spherical indentation, using a 3.16 mm steel probe. An inverse method was used to recover the elastic parameters of the substrates from the experiments: the indenter and substrate were modeled with finite elements (ANSYS Inc., Houston, Pennsylvania, USA) (Figure 4.6a). Axisymmetric elements were used. The spherical indenter was assumed to be perfectly rigid, and frictionless contact elements were inserted between the indenter and the upper surface of the substrate. The substrate was modeled as a Neo-Hookean incompressible material because of its elastomeric nature. The finite element mesh was progressively refined until convergence of the force-displacement curves.

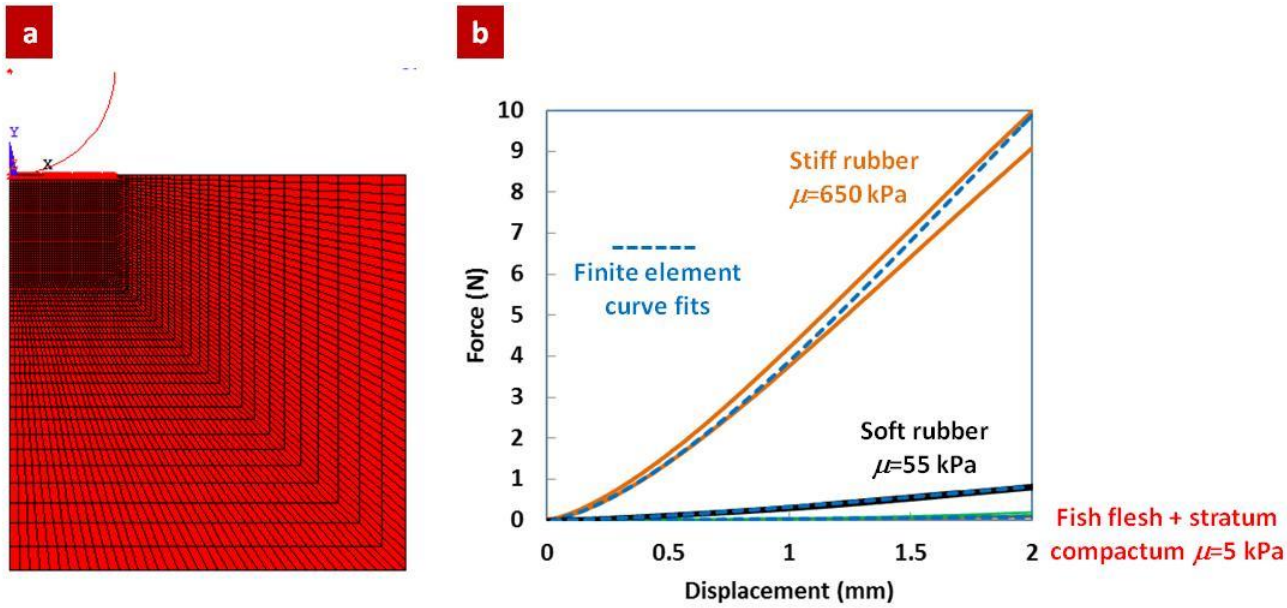

Figure 4.6. (a) Axisymmetric finite element model of the ball indentation test; (b) the model was used to fit the experimental curves, yielding the shear modulus of the Neo-Hookean substrates.

The experimental indentation curves were then fitted with the finite element model, with the shear modulus of the Neo-Hookean model μ as the fitting parameter. This model provided excellent fits to the experimental curves (Figure 4.6b), and we found about an order of magnitude of difference between each of the three substrates in terms of stiffness. Individual fish scales (E=0.5-1 GPa, Chapter 3) are almost rigid in comparison: they are 10,000 times stiffer than the flesh and s. compactum. The three different substrates were then used for puncture tests on individual fish scales, following the setup and procedure described in section 4.2.1. (Figure 4.1). A sharp steel needle (tip radius=25 μm) provided a good model for a tooth, with a simplified geometry and a stiffness about two orders of magnitude greater than the scales themselves. The setup was installed in a miniature loading stage (Ernest F. Fullam Inc., Latham, NY, USA) in order to record force and displacement. These puncture tests were conducted in quasi-static conditions and at a relatively slow displacement rate of 0.005 mms^{-1} (the effects of

loading rate were not explored in this work). All of the tests were performed in hydrated conditions: the scales were stored in water and positioned on the substrate just before the test. The short duration of the test (several minutes) did not allow for significant loss of water content from evaporation, and specimens were kept hydrated throughout testing.

4.3.1.3. Effect of puncture site

While previous puncture tests on individual fish scales were performed through the centre of the scales [59] (section 4.2.1.), puncture performance probably depends, in fact, on the puncture location. To examine this effect, puncture tests were performed on a single fish scale at five different locations on the upper surface of the scale (Figure 4.7): midline distal (edge) locations in all four fields of the scale, i.e. anterior, posterior, dorso-lateral, and ventro-lateral edge locations, and a more central location within the anterior field near the elevated "focus".

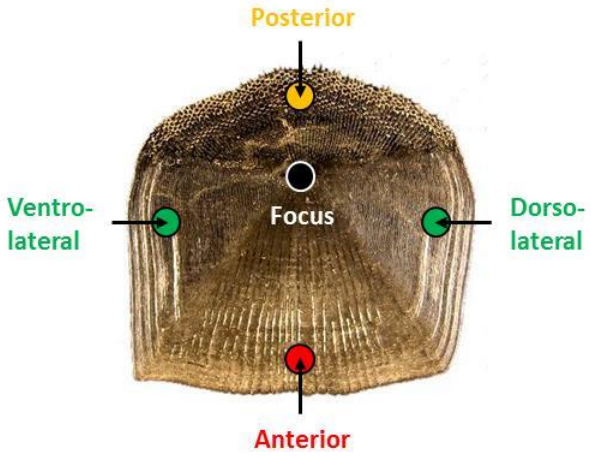

Figure 4.7. Puncture sites on the scale including midline edge locations in the anterior, posterior and lateral fields, and a central location near the elevated "focus".

4.3.1.4. Effect of number of overlapping scales

The scalation pattern generates overlap of scales which must all be defeated by a predator in order to injure the fish. In this section we explored potential synergies between scales when they overlap on the natural skin of fish. The same experimental setup as for the single scale test was used. As a first set of experiments, we stacked several scales into piles up to ten scales thick on the hard rubber substrate (Figure 4.8). The scales were therefore completely overlapping one another and had the same orientation. A central location in the anterior area of the scale was targeted for puncture and the needle driven through the entire stack of scales.

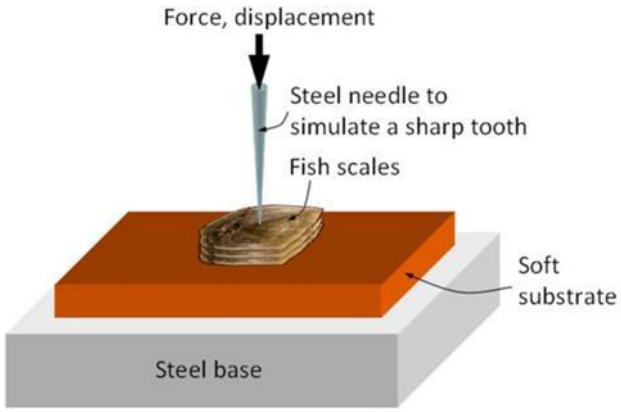

Figure 4.8. Experimental setup for puncture tests on stacks of scales.

4.3.1.5. Effect of friction between scales

As discussed in Chapter 2, the upper surface of the scale is hard and shows intricate roughness patterns (circuli with denticles, Figure 2.6d, and ctenii, Figure 2.5a) which may generate friction or even possible mechanical locking between overlapping scales. These interactions would increase puncture resistance and impact swimming performance (increase flexural stiffness of the fish and provide an exotendon effect). Friction coefficients can be challenging to measure experimentally for engineering materials, and even more so for a biological material like fish

scales. In this work we therefore used an indirect approach which exploited the fact that the deformation of the scales during a puncture test is dominated by bending. In general, the bending stiffness of two or more stacked plates depends on how they are joined, and more specifically on what level of shear stresses can be transmitted at their interface. For example, a stack of perfectly bonded plates will have a significantly higher flexural stiffness compared to a stack of plates that are in simple, frictionless contact. We used this property to estimate the coefficient of friction between the scales. The initial stage of the puncture test was modeled with an axisymmetric finite element model (ANSYS Inc., Houston, Pennsylvania, USA). The model incorporated the salient features of the system: a Neo-Hookean substrate, scales including bony and collagen layers, and rigid indenter whose profile was built from optical images of the needle (Figure 4.9a). The interface between the substrate and the scale was assumed to be frictionless, since both surfaces are smooth and hydrated. The experimental value for the stiffness of the hard rubber substrate was used in the model. Meanwhile, the properties of the bony and collagen layers within the scales were taken from previous experiments on striped bass scales (section 2.4.2.). Figure 4.9b shows that the finite element model captures the initial slope of the experimental puncture tests remarkably well (we limited the scope of this type of model to initial stiffness, because problems associated with element distortion and convergence appeared for large deflections). In order to investigate the effect of friction between scales, additional finite element models were generated with stacks of 2, 3, 5, 8 and 10 scales (Figure 4.9c). The friction parameter between the scales was the unknown in the models, and can be used as a parameter to fit the experiments. Two extreme cases were considered: perfectly bonded scales and frictionless scales.

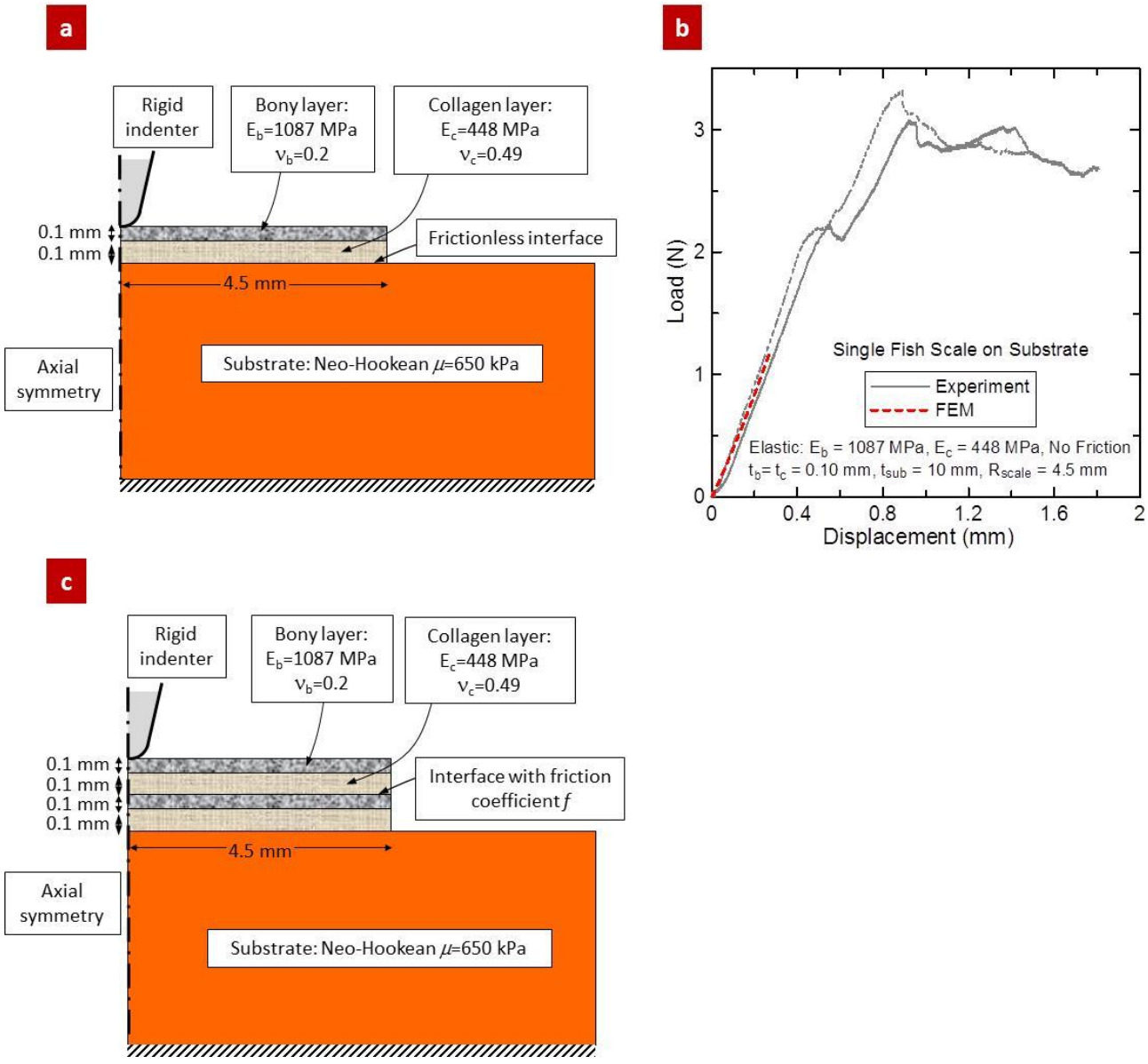

Figure 4.9. (a) Axisymmetric finite element model of a puncture test on a single scale; (b) comparison of the curves obtained by experiments and the FE model; (c) axisymmetric finite element model of a puncture test on a stack of 2 scales.

4.3.1.6. Effect of scale arrangement

The previous series of tests examined the puncture resistance of stacks of perfectly aligned scales. In reality, the scales overlap on the surface of the fish and the scalation pattern is more complex (Figure 2.6b). To examine the effect of scale arrangement on overall puncture

performance, three fish scales were plucked from the mid-lateral body region of the fish specimen and tested directly on the hard rubber substrate in three different arrangements, with the procedure repeated five times (Figure 4.10): (i) stacked (which is the same arrangement as reported in the previous section), (ii) staggered overlap (which is the natural arrangement), and (iii) rotated (such that the "effective" protective thickness was the same as (ii)). The stacked scale arrangement was the same arrangement as reported in the previous section. It exhibited the thickest puncture site, the highest extent of scale overlap, and least of scale-substrate contact area. In the staggered overlap arrangement, three scales were arranged in the exact same pattern as the natural scalation pattern, and the puncture site was at the centre of the overlapping region of the scales. The exposed areas of the scales were outlined with marker to facilitate replication of the natural overlap pattern directly on the rubber substrate. In the rotated arrangement, scale #2 was rotated 180º counter-clockwise and shifted down or inserted entirely between scales #1 and 3 so that the dorso-ventral borders of all three scales were aligned and the three scales placed on the hard rubber substrate. The objective of the rotated configuration was to change the arrangement of the scales while maintaining the "effective" protective total thickness as the staggered overlap case.

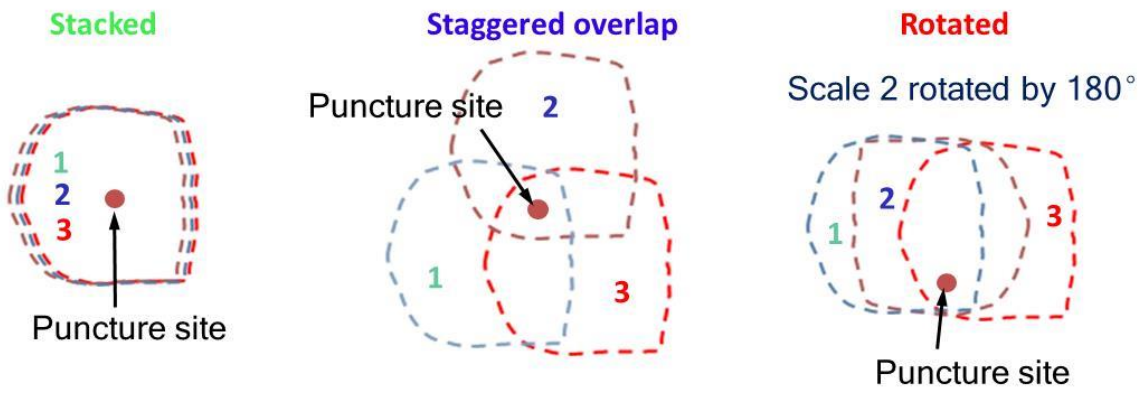

Figure 4.10. The three scale arrangements used for puncture tests: stacked, staggered (natural) overlap, and rotated.

4.3.1.7. Effect of scale interaction & force dispersal

The objective of this test was to assess the deflection of the skin during the puncture event on an actual fish, in order to unveil potential collective mechanisms of the scales preventing excessive deflection and localization. The overall experimental setup is shown in Figure 4.11a. A whole fish was placed on a high capacity precision scale. A blunt probe (tip diameter=2.2 mm) attached to a micromanipulator, itself attached to a rigid column clamped on the table, was used to press onto the skin of the fish. The micromanipulator was used to impose deflections with accuracy, while the scale was used to measure the puncture force. For all tests, the loads were kept below the force required to penetrate the scales (F=1 N). Two cameras were mounted above the fish in order to image its surface from either side of the puncture site. These cameras produced stereo images of the fish skin (i.e. images of the same object viewed from two different points). The images were in turn used for three-dimensional image correlation (VIC-3D, Correlated Solutions, Inc.). This method can determine the three-dimensional shape of an object (in this case the surface of the fish). In addition, comparison of two pairs of images process the full three-dimensional displacement field (Figure 4.11b). The correlation technique consists of tracking the location of dark and bright features on the surface of the object, which we generated in this case by applying a finely crushed black graphite powder over the area surrounding the puncture site. The test consisted of acquiring a pair of initial images of the fish, and then acquiring another pair of images at a puncture force of 1 N. The test was first performed on an intact fish. The fish was then entirely descaled around the puncture site, except for the scale directly at the puncture site. The test was then repeated at the exact same location.

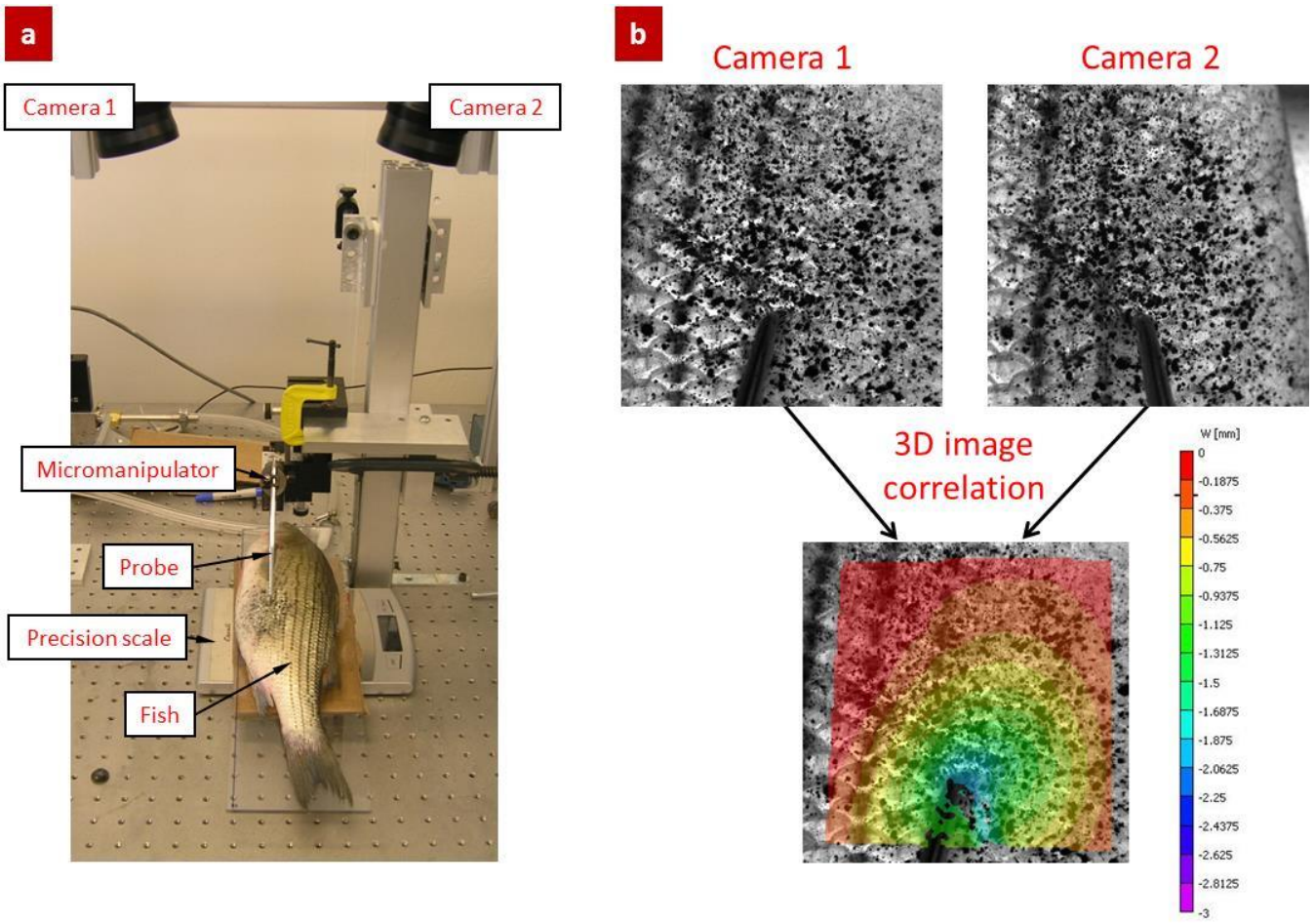

Figure 4.11. (a) Experimental setup for skin indentation tests on striped bass with stereo-imaging; (b) stereo images of the puncture site on the scaled (natural, intact) fish at 1 N force, and 3D displacement field around the puncture site computed using 3D image correlation.

4.3.2. Results

4.3.2.1. The puncture performance of striped bass fish skin

The results of puncture tests on intact striped bass skin demonstrate that the scales provide a highly efficient barrier against predators, increasing the puncture resistance of the skin by four to five times (Figure 4.12). The scales also stiffen the skin, with the effect of decreasing the amount of deflection upon puncture. In terms of biomimetics, it is critical to examine and identify the structure and mechanisms behind this performance. In section 4.2.2., we demonstrated that

individual scales displayed a remarkably high resistance to sharp puncture, and we identified the structures and mechanisms associated with this performance. The outer "bony" layer and inner "collagen" layer operate in synergy to trigger specific failure mechanisms which dissipate energy and increase the force required to completely puncture the scale. Other potential effects influencing the puncture mechanics and performance of fish skin include substrate stiffness (dermis and flesh), puncture site, number of overlapping scales, friction between scales, scale arrangement, and long distance collaborative mechanisms between scales and force dispersal. These various aspects are systematically explored in the following sections.

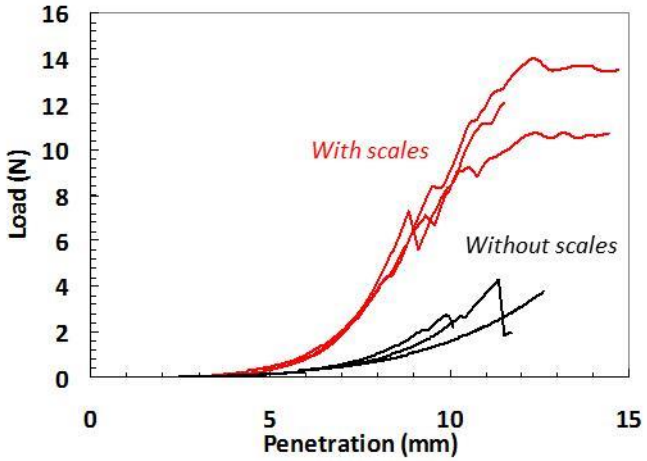

Figure 4.12. Force-displacement curves showing that the scales increase the puncture resistance of the skin by four to five times.

4.3.2.2. Effect of substrate stiffness

Figure 4.13 shows the results of this set of experiments. The stiffness of the substrate has, as expected, a strong effect on the stiffness and deflection during the puncture tests (Figure 4.13). However, we found that the substrate stiffness had no significant effect on the force required to puncture the scale, at least over the range of substrate stiffnesses explored here (which is

consistent with the concept of a soft system protected by stiff scales). This finding therefore indicates that the puncture resistance (puncture force) of the fish skin remains unchanged whether the underlying substrate is contracted (stiff) or relaxed (soft). In terms of biomimetics, this result indicates that the stiffness of the backing material for artificial scales is of secondary importance. It is however important to limit the amount of deflection, at and around the puncture site, in order to minimize the risk of blunt injury to the underlying tissues. This aspect is discussed in further detail towards the end of this chapter.

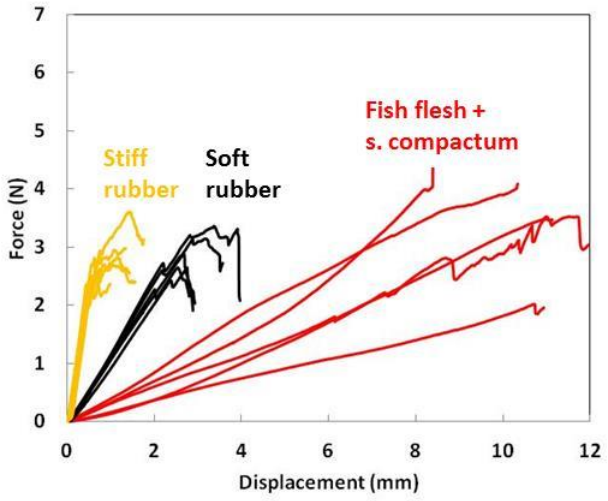

Figure 4.13. Force-deflection curves for puncture tests on individual scales using three different substrates.

4.3.2.3. Effect of puncture site

The puncture force-displacement curves at each puncture site were highly repeatable, and showed a similar pattern with a slight force drop at 2.0-2.5 N and a subsequent force increase until final failure (Figure 4.14a). The puncture failure mode of a single scale follows the same mechanisms as discussed in section 4.2.2., regardless of puncture location. However, we observed differences in puncture stiffness and force across different puncture locations (Figure

4.14a). The anterior centre location had the highest puncture stiffness and force due to its increased thickness, and puncture force was lowest at the thin posterior edge location (Figure 4.14b,c). The performance of the scale in resisting puncture was shown to be site dependent, which can be explained by variation in thickness across the scale (Figure 2.5b) and possibly by other scale features, for example differences in HAp content and surface structures across the scale (Figure 2.5a). As noted in Chapter 2, however, the “effective “ thickness of protective material resulting from superposing three scales is uniform over the surface of the fish and as a result, puncture on whole fish was less dependent on location than for the individual scale.

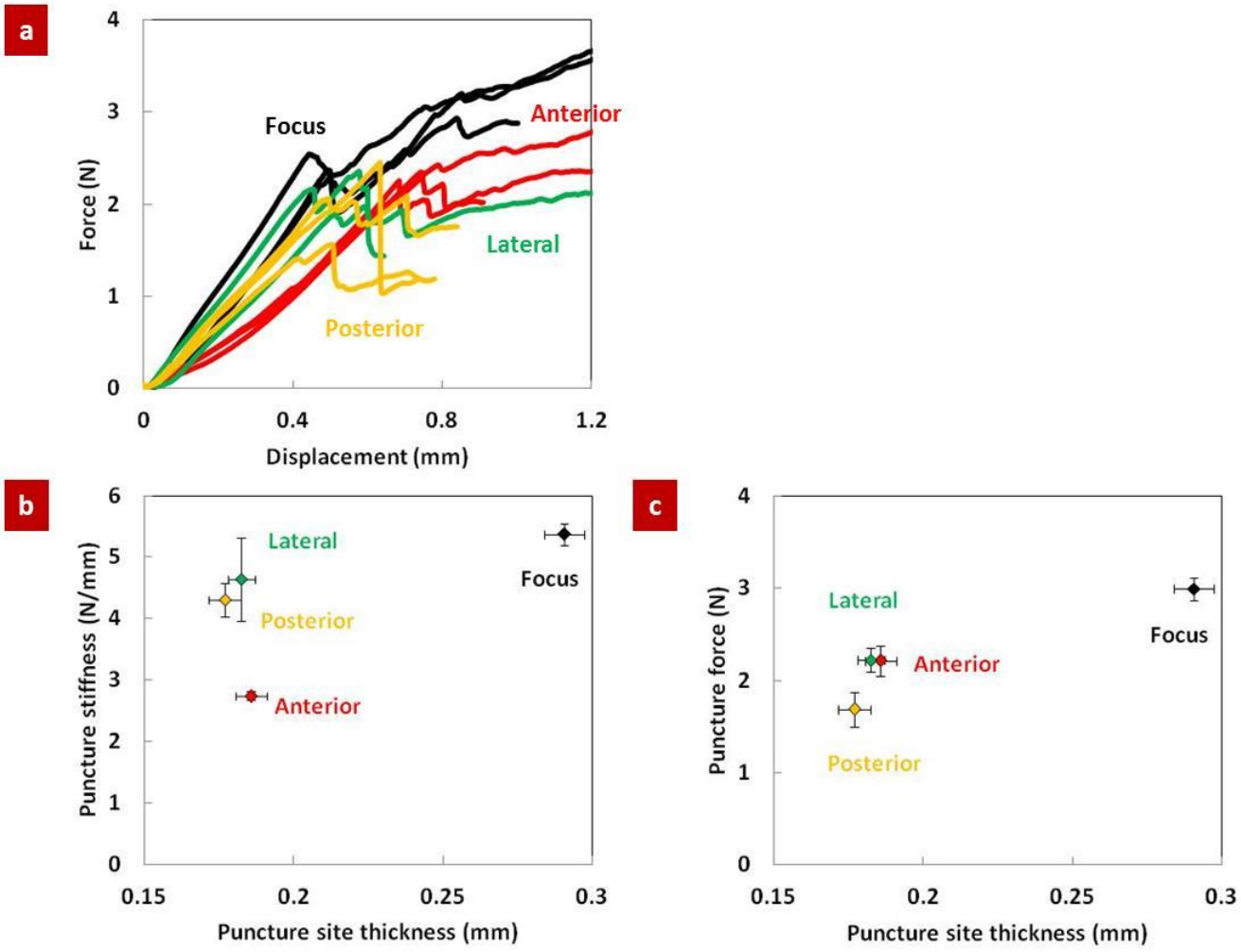

Figure 4.14. (a) Force-displacement curves at each puncture site; (b) puncture stiffness as a function of puncture site thickness; (c) puncture force as a function of puncture site thickness.

4.3.2.4. Effect of number of overlapping scales

The force-displacement curves for stacks of 2, 3, 5 and 10 scales are shown in Figure 4.15a, which also includes the force-displacement curve of individual scales. We found, as expected, that the force required to puncture the entire stack of scales increases with the number of scales. The failure mechanism was similar to what was observed for single scales (section 4.2.2.). The bony layers failed in sequence, softening the system while the underlying collagen layers delayed

further penetration. Closer examination of the force-deflection curves revealed a sequence of softening/stiffening events corresponding to the needle defeating the bony layer (softening), and then deforming the collagen layer and meeting the upper surface of the next scale down (stiffening) until full penetration of each scale ("failure event"). These trends can be better seen by plotting the instantaneous stiffness (slope) of the force-deflection curve as a function of displacement (Figure 4.15b).

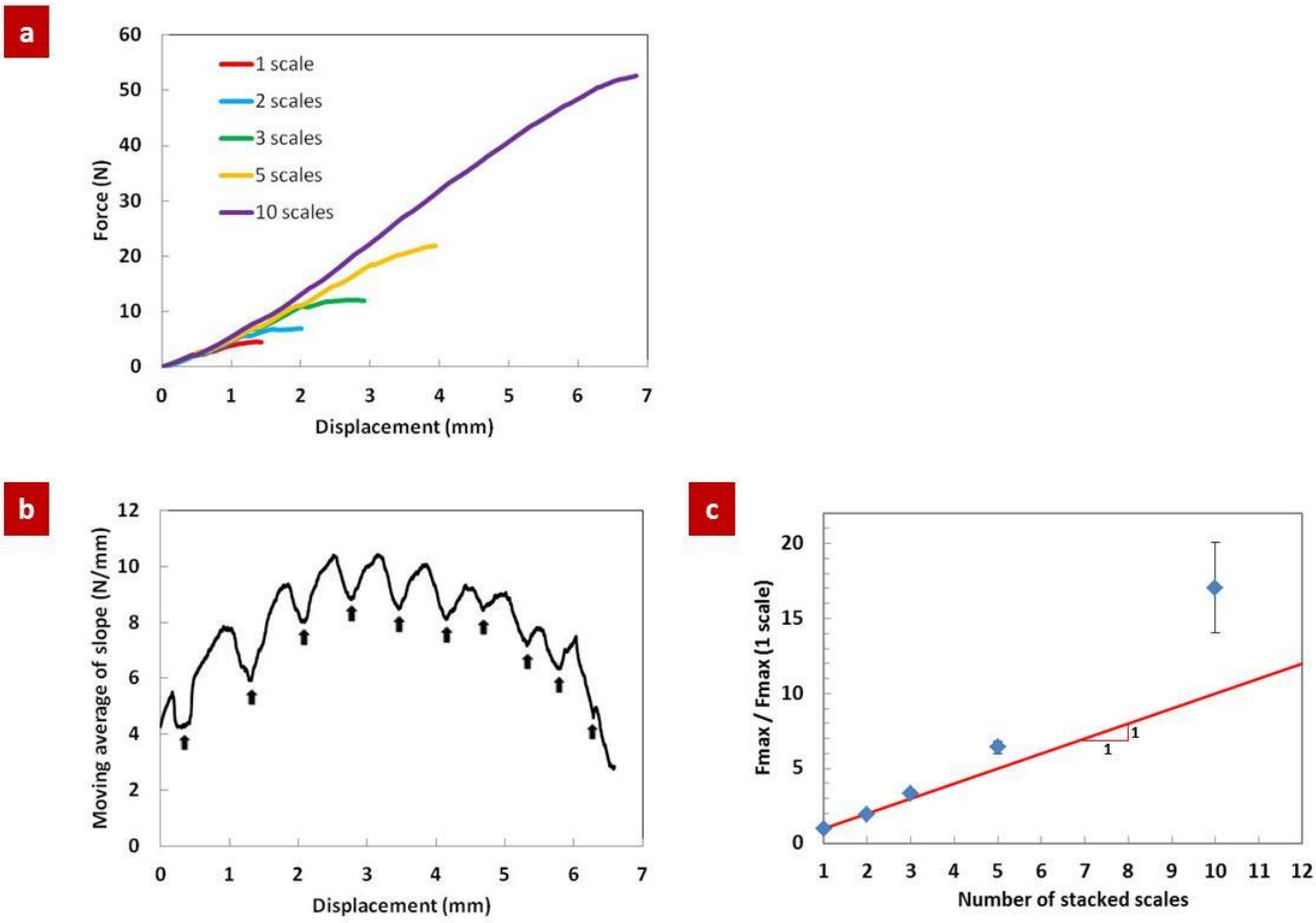

Figure 4.15. (a) Force-displacement curves; (b) instantaneous slope of the force-deflection curve as a function of displacement (arrows indicate scale "failure events"); (c) normalized puncture force as a function of number of stacked scales.

Figure 4.15c shows that the puncture force increases almost linearly with the number of scales, at least up to 3 scales, for example doubling the number of scales doubles the force at puncture. This result is relevant to striped bass since three overlapping scales cover the body of the fish at any point. We found that for natural striped bass skin the mean puncture force value for the three scale overlap region was 6.90 $\pm$ 0.24 N (n=5 tests), which is lower than the puncture force of three stacked scales (10.1 $\pm$ 0.3 N (n=11 tests)) and can be explained by puncture site thickness. When the needle punctured 5 and 10 scales the results deviated from the linear trend, possibly due to the nonlinear profile of the needle. This result suggests that there are no significant synergistic mechanisms amongst scales in this configuration. Figure 4.15a also shows that the puncture stiffness only slightly increased when the number of scales was increased: the scales are so much stiffer than the substrate that substrate deformation accounts almost entirely for the deflection measured here. In effect, the scale or stack of scales appeared to "sink" into the soft substrate over the course of the experiment. As a result, higher force to penetration resulted in more deflection at failure, as also shown in Figure 4.15a. The effects of scale and substrate deflections are examined in more detail in sections 4.3.2.6. and 4.3.2.7.

4.3.2.5. Effect of friction between scales

Figure 4.16 shows the initial predicted slopes for these two types of interfaces and as function of number of scales. As expected, the initial stiffness increases with number of scales, and stacks of bonded scales are stiffer than frictionless scales. The initial stiffness from the experiments presented above is also plotted. The model does not exactly predict the experiments, possibly because the thickness of the scale in the model was assumed to be uniform without considering the actual conical shape of the scale (Figure 2.5b). Nevertheless, the model suggests that the friction between the scales is negligible, since the frictionless models were the closest to the

experiments. The circuli therefore do not generate significant friction, probably because of the soft, gel-like, s. spongiosum between the scales, which may act as a solid lubricant, preventing direct contact between scales. Low friction between scales is highly beneficial in terms of swimming efficiency when the scales slide on one another, but maybe less so in terms of puncture resistance.

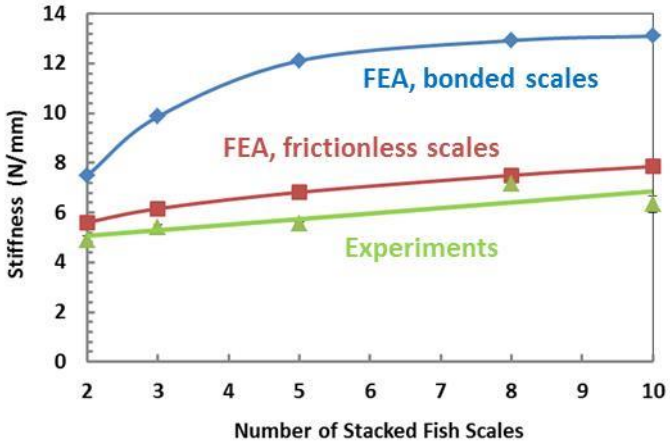

Figure 4.16. Predicted (bonded and frictionless scales) and experimental initial slope of the force-deflection curve as a function of number of scales.

4.3.2.6. Effect of scale arrangement

Figure 4.17a shows representative force-deflection curves for each of the three arrangements. We found that the stiffness was the same for all three arrangements, and that the staggered and rotated scales displayed the same penetration resistance, the final failure events corresponding to the slight force drops at the end of the force-displacement curves. The stacked scales, however, had the highest puncture resistance because the puncture site was in the anterior field of the stacked scales in a location that was notably thicker than the puncture sites for the staggered and rotated scale arrangements. Over the course of the tests on scales in different overlapping

arrangements, we also made interesting observations: for all configurations, the stiff stacks of scales "sank" into the soft substrate (Figure 4.17b). In the case of staggered overlap scales, the section of scales at the periphery of the system lost contact with the substrate. These two effects arose because of the large contrast of stiffness between the scales and the hard rubber substrate. The effective contact surface between scales and substrate remained essentially the same for all arrangements, and in all cases the scales appeared to "sink" within the soft substrate. This deformation mode resulted in high localized strains in the soft substrate, which would potentially lead to blunt injury on the actual fish. This observation motivated the final experiment in this chapter, where we investigated collective scale mechanisms around the puncture site.

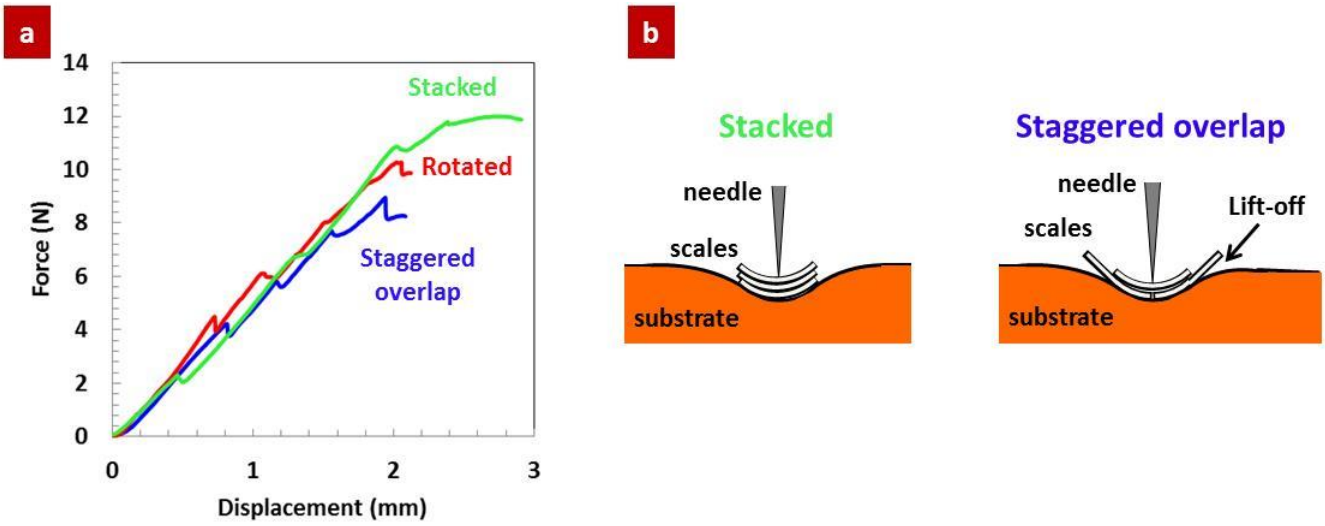

Figure 4.17. (a) Force-displacement curves for the three scale arrangements; (b) "sink-in" mechanism of scale and substrate deformation.

4.3.2.7. Effect of scale interaction & force dispersal

Figure 4.18a shows the deflection of the fish skin around the puncture site for the scaled (natural, intact) and descaled conditions. Profiles of these two surfaces were then taken along radial lines intersecting at the puncture site, in order to produce the plot shown on Figure 4.18b. The results

show that descaling the skin increases the deflection by about 25%, but only close to the puncture site. The region that showed additional deflection due to descaling corresponded to a circular area around the puncture site, whose size matched the dimensions of the scale. At larger distances of 10 mm and further away from the puncture site, the deflections of the scaled and descaled fish were similar. These observations confirmed the "sink-in" mechanism observed in the previous section (Figure 4.17b). Individual scales subjected to localized puncture forces can deform the underlying soft tissues, possibly up to a point where the soft tissue is damaged. This type of "blunt trauma" is however averted by the surrounding scales, which support the scale being punctured and redistribute the puncture force over large surfaces and volumes in the soft tissue.

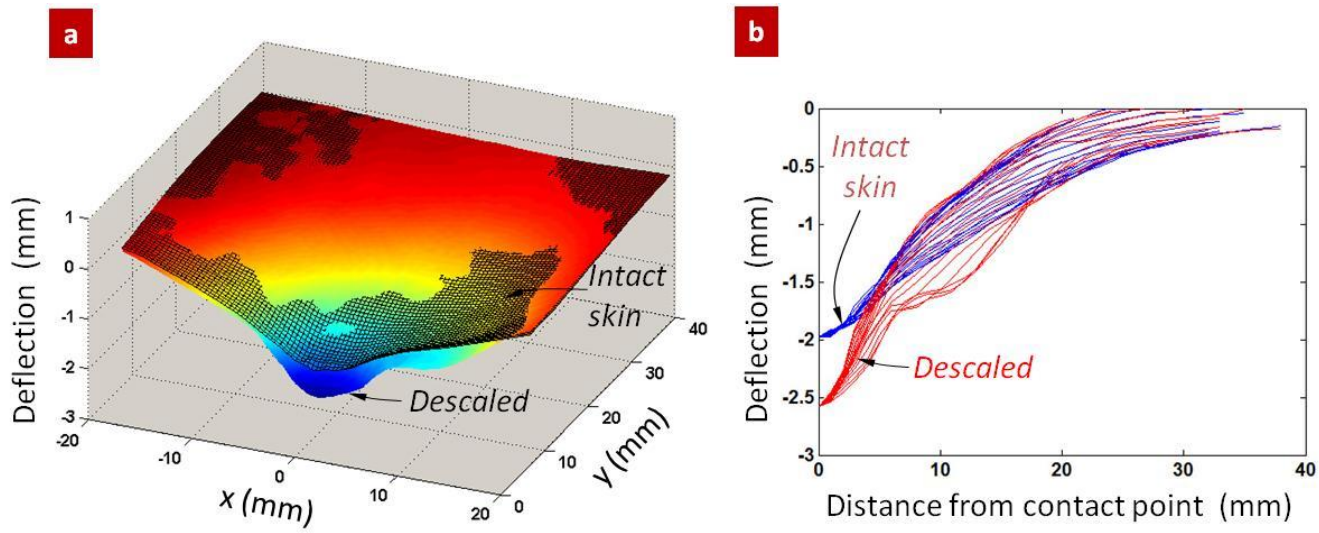

Figure 4.18. (a) Deflection of the skin around the puncture site for scaled (natural, intact) and descaled conditions; (b) two-dimensional profiles around the puncture site for scaled and descaled conditions.

4.4. Puncture tests on stratum compactum

4.4.1. Results

The results of puncture tests on scaled (natural, intact) and descaled skin from striped bass, the latter composed mainly of s. compactum with a thin overlying epidermis, are shown in Figure 4.19. Although the scaled skin exhibited a puncture force *ca*. 4X greater than that of descaled skin, the descaled skin still displayed a relatively high puncture force of *ca*. 2 N. This finding demonstrates the substantial contribution made by the s. compactum to the puncture resistance of the natural skin from striped bass with its pattern of 3-scale overlap, and suggests an important mechanical role of the s. compactum, and not just of collective scale mechanisms, in increasing the penetration resistance of the skin. The possible function of the s. compactum in improving the penetration resistance of the skin was first proposed for the s. compactum of shark skin [33], but the data reported here clearly demonstrate the contribution of the s. compactum to the puncture performance of teleost skin and highlight the multifunctionality of this layer of integument.

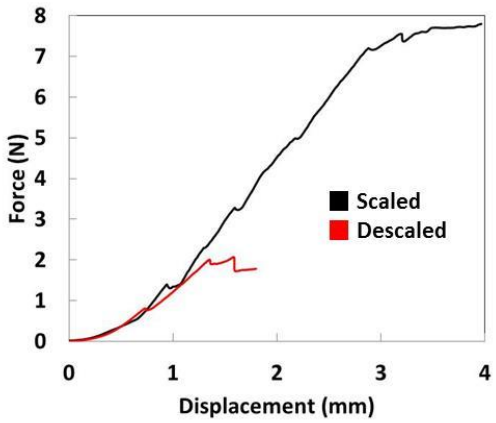

Figure 4.19. Force-displacement curves for puncture tests on scaled (natural, intact) and descaled striped bass fish skin.

4.5. Discussion

We further investigated the mechanisms operating at stage II of the scale puncture sequence, since they are powerful enough to increase the resistance of the scale by an additional 1 N (representing an additional 50% of the load at failure of the bony layer). In particular, we examined the controlled deflection of the four "bony flaps" using an idealized three dimensional geometry shown in Figure 4.20a,b. Each of the fours flaps was assumed to be rigid and hinged along a straight line at the bone/collagen interface. The force from the needle was assumed to be evenly distributed between the tips of the 4 flaps. Only two mechanical loads resist the deflection of the flaps by balancing the force from the needle: (i) the bending moment transmitted through the remaining membrane of the bony layer, and (ii) the intact collagen layer, which acts as a "retaining membrane" for the flaps. Interestingly, in this configuration the collagen layer is in a state of biaxial tension at the penetration site, and the purpose and advantage of its cross-ply structure become evident.

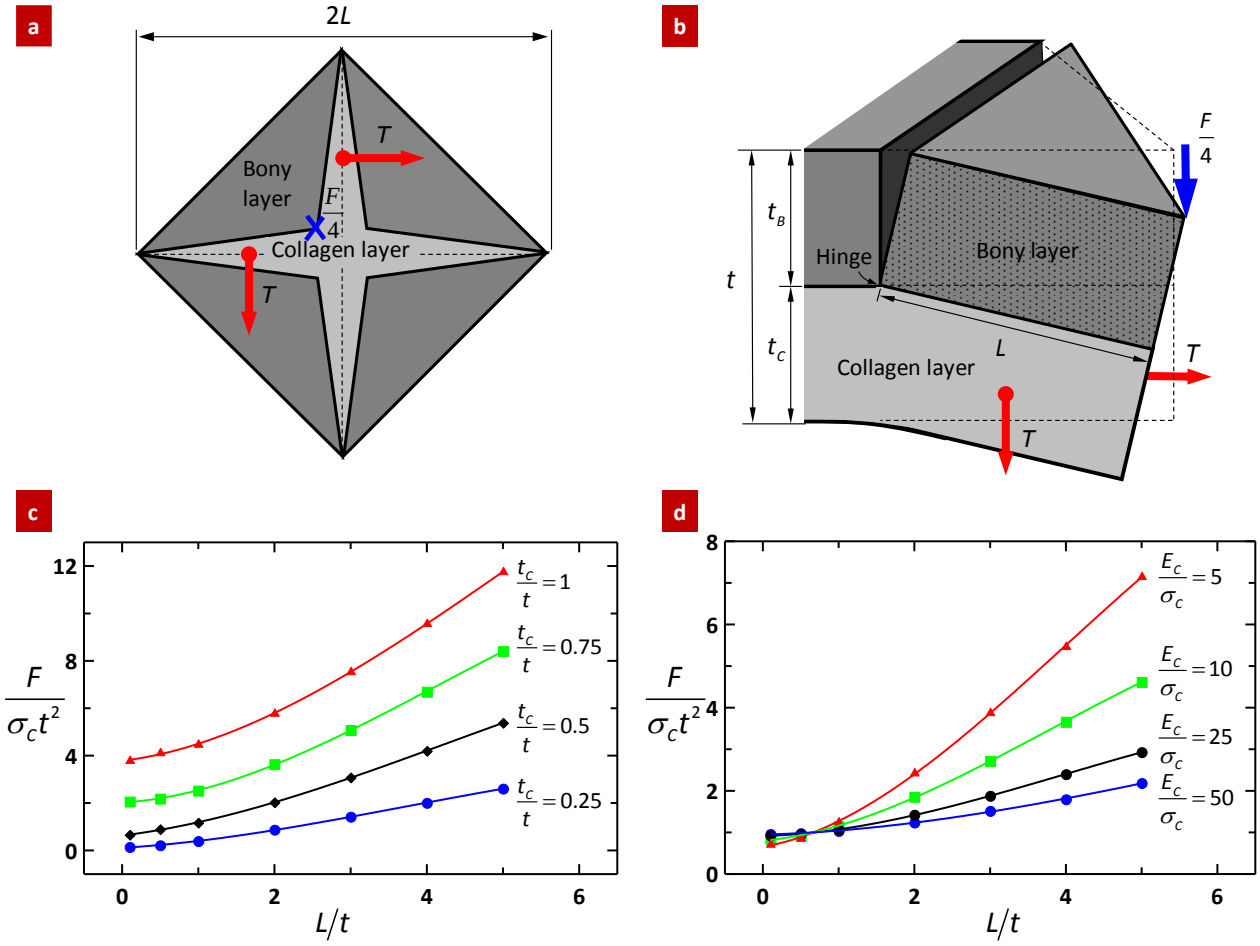

Figure 4.20. (a) Top view of the idealized puncture configuration; (b) three-dimensional view of single bony flaps. The force applied by the needle (*F/4*) and the forces generated by the tension in the collagen layer are shown. (c) Effect of collagen layer thickness and (d) collagen resilience on the normalized penetration force.

The bending moment transmitted at the membrane was evaluated by assuming perfect plasticity in the bony layer with $\sigma_Y = 60$ MPa (evaluated from our tensile test). In order to balance this moment, the force applied by the needle was estimated at 1.2 N (see section 4.2.1.1. Analytical "four flaps" model, for calculation details), which is actually below the force at which the bony layer fractures. This value represents an upper bound estimate, since in reality the bony layer probably cracks before the full plastic state can be reached. This prediction shows that in stage II, there is no bending moment transmitted at the bony flaps, and that the flaps can be

assumed to rotate about frictionless hinges. The experiments show circumferential cracks in the region of the hinges, confirming that little or no bending moment can be transmitted though the bony hinge. The second mechanism examined was associated with the collagen, which acts as a retaining membrane for the flaps.

In the model, the collagen layer was assumed to have completely delaminated from the overlying surface of the bony layer, which is consistent with experimental observations towards the end of stage II. The collagen layer then acts as a retaining membrane, with biaxial tension as the dominant stress. Based on the idealized geometry, the moment balance of a single bony flap about the hinge led to a simple expression for the penetration force as a function of bony and collagen layer thickness (t_B, t_C), length of the flaps (L), and stiffness (E_C) and strength (σ_C) of the collagen layer. Full penetration at the end of stage II was assumed to be reached when the collagen failed in tension (at a stress of 65 MPa according to our tensile tests). Our model predicted a penetration force of F=3 N based on the properties of the collagen layer (E_C=500 MPa, σ_C=65 MPa) and optical observation ($t_B = t_C$=100 μm, L=200 μm). This prediction is remarkably close to penetration force we measured experimentally, which demonstrates that the retaining membrane effect dominates stage II and controls the ultimate penetration resistance of the scale.

In terms of design, the model reveals that longer flaps are desirable, and since L is larger for larger "teeth" and higher forces, the scale provides a greater resistance to penetration for larger teeth and stronger bites (Figure 4.20c,d). A thick collagen layer is also beneficial, although a minimum of bony material is required to form stiff flaps. This finding completes previous discussions on mechanical benefits of thicker collagen fibrils and plywood organization in the collagen layer [49, 52, 53, 79]. Finally, a soft and strong material increases resistance to

penetration, although a too soft backing layer may lead to excessive deflection that may damage the underlying tissues even before needle penetration. A cross-ply of collagen is therefore ideal for this function, and the function of the harder bony layer is to protect the collagen layer from direct contact with the tip of the needle, and to mitigate the stresses transmitted onto the softer collagen layer by redistributing them over a large area.

Individual teleost fish scales are therefore high performance natural protective systems, offering resistance to puncture superior to modern engineering polymers typically used for protective applications. Remarkably, fish scales are made of a set of materials that are both softer and weaker than these engineering polymers, which highlights the important role of the structure and architecture of the scale in "amplifying" the properties (as seen in other classes of biological materials [80-82]). The high performance of the scales is the result of a fine balance of structure and material properties, and in particular the hardness and stiffness of the outer layer, the softness and strength of the inner layer, and an interface weak enough to delaminate and allow the collagen layer to stretch under the bony flaps. While this first study on the puncture mechanics of fish scale does not consider viscous effects, it is likely that viscoelastic and viscoplastic effects also contribute to the energy dissipation capability of the scale. The actual skin of the fish is of course covered with a large number of overlapping scales and, for striped bass, we counted that any given point on the surface of the body is covered with 3 or 4 layers of scales. The resulting multilayer system alternates hard and soft layers in an arrangement reminiscent of the design of bulletproof glass. In addition, overlapping scales ensures compliance and breathability, two highly desirable properties for personal armors. A biomimetic design at the individual scale level could therefore be combined with a clever arrangement of the scales at the macroscale to yield a hierarchical protective system with attractive properties.

In this chapter, we also showed that teleost fish scales, while being light and thin, provide a flexible layer with remarkable protection against sharp puncture. The resistance to puncture observed on the actual fish could be largely explained in light of the additional experiments and models we presented here. In summary, puncture resistance is generated by sophisticated mechanisms at the level of the individual scales, consisting of a two-step failure process involving both the bony layer and collagen layer. On the actual striped bass the scales form a well-defined scalation pattern, offering three layers of scales to resist puncture at any point on the fish. While there are significant variations in thickness within a given individual scale, the scalation pattern is such that the total "effective" protective thickness is uniform over the entire fish. The stiffness of the substrate was not found to affect the puncture force, at least in the range of substrate stiffnesses we explored (which are relevant to the actual fish and to actual biomimetic applications). We found that overlapping three scales essentially multiplies their puncture force by three. Friction between the scales is negligible, and therefore does not generate additional resistance to deformation and puncture, regardless of scale arrangement. While our experiments and models demonstrate a rather simple scenario in terms of puncture force, they also revealed a new failure mode: even if the scales resist puncture, the large deflections and deformations of the softer underlying tissues around the puncture site may lead to blunt injury. Using stereo-imaging and image correlation, we demonstrated that the scales surrounding the puncture site redistribute the puncture force over large surfaces and volumes in the soft tissue, which verified the hypothesis proposed by Vernerey & Barthelat [65]. This mechanism of scale interaction and force dispersal prevents unstable localized deformation of the skin and damage to underlying tissues. Fish scales therefore provide the fish with a flexible, light weight protective system against both laceration and blunt injuries. This study on natural fish skin teaches us useful

lessons for future biomimetic “artificial fish scales”: the resistance to puncture of individual scales is equally important as their overlap and their arrangement to provide efficient protection.

CHAPTER 5

FLEXURAL PROPERTIES OF WHOLE STRIPED BASS FISH

5.1. Overview: The bending properties of whole teleost fish

In Chapter 4, we revealed the principal mechanism of individual teleost fish scales that amplifies their penetration resistance, which involves induction of a specific failure mode in the upper mineralized half of the scale and subsequent interaction with the lower pure collagenous half upon puncture with a sharp probe. At the tissue level, however, teleost fish skin is composed of several overlapping scales arranged in precise, species-specific squamation patterns [8], and additional mechanisms of scale interaction may further synergize puncture resistance of fish skin at higher length scales. In Chapter 4, we therefore also investigated key mechanisms and parameters controlling the high puncture resistance of teleost fish skin, and demonstrated that the scales mechanically interact and redistribute the force upon puncture over large volume and thus limit local deflection and prevent damage to the soft underlying tissue. This finding was the first experimental data in support of the model of fish scale interaction upon puncture proposed by Vernerey & Barthelat [65]. However, as described in [65], this model of scale interaction applies not only to puncture events, but also to whole fish bending during locomotion as progressive interlocking of scales could play an important role in the undulatory locomotion of teleost fishes. That is, fish scales on the inner, concave side of a bent teleost during swimming could potentially mechanically interact to assist with locomotion by increasing whole fish flexural stiffness at high body curvatures at the end of a swimming stroke, thus providing an exotendon effect and facilitating muscle contraction of the next swimming stroke. In this scenario, the scales deform and accumulate elastic strain energy at the end of each stroke, which can be recovered to initiate and rapidly accelerate the next stroke. The scales would therefore function as an external tendon (or exotendon) to enhance swimming efficiency (reduce the energy required for locomotion).

Bruet *et al*. [15] investigated puncture mechanisms of individual fish scales but from the ganoid fish the gray bichir, *Polypterus senegalus*, and examined the scalation pattern on this fish species, including how neighboring ganoid scales interlock and hinge upon bending using a peg-and-socket mechanism that allows some mobility. Gemballa & Bartsch [83] more thoroughly studied the scalation patterns of various ganoid and teleost species and showed that the peg-and-socket articulation of ganoid scales from *Polypterus* spp. and *Lepisosteus* spp. restricts movement of scales within the same cross-helical scale row, but that other scale features such as the anterior process and concave anterior margin permit displacement or sliding of scales relative to each other and increased scale overlap and thus also permit high body curvatures during undulatory locomotion. However, previous reports have suggested that fish scales, including ganoid scales, may indeed have an effect on locomotion by increasing flexural stiffness at high body curvatures [84]. The possible role of scaled fish skin in increasing whole fish flexural stiffness was first investigated by Long *et al*. [84] using the ganoid fish the longnose gar, *L. osseus*. These researchers determined a significant decrease in whole fish flexural stiffness after incision of the dermis and removal of a single row of scales at a caudal location on the fish. However, Long *et al*. [84] assessed only the effects of a single row of ganoid scales and underlying dermis on the flexural stiffness and anguilliform locomotion of this ancient fish species and did not describe a potential whole body exotendon effect provided by the scaled skin during carangiform locomotion of teleost fish species.

It is possible that the scales in fact provide only a small or negligible amount of whole body flexural stiffness during fish bending or swimming and thus do not provide a hypothesized exotendon effect. Although the scales and intervening gelatinous stratum (s.) spongiosum (Figure 2.1) composing the upper portion of the dermal layer of the integument in striped bass

may not function in locomotion via an external tendon effect, it is the lower layer of the dermis, the collagenous stratum (s.) compactum (Figure 2.1), that has received the most attention as a potential energy storage device providing an exotendon function to the skin [8, 9, 17, 61]. The general structure of the s. compactum was first described by Motta [33] for sharks. It consists of a cross-helical arrangement of collagen fibres whose fibre angles relative to the long axis of the fish vary along its anteroposterior (A-P) length, and whose alternating lamellae of left- and right helically-wound fibres were later shown to exhibit varying degrees of crimping or waviness along the fibre axis [61] (Figure 2.1). Shortly thereafter, Wainwright *et al*. [17] were the first to propose that the s. compactum acts as a whole body tendon in sharks. Wainwright *et al*. [17] based their hypothesis on mechanical theory described in [31] on open- and closed fibre-reinforced cylinders (with helically-wound fibres similar to the s. compactum). This theory explained volume changes of the cylinder as a function of change in fibre angle under tension or compression of the cylinder, and how a fibre angle of 54 °, also seen in fishes, is optimal for having the fibres aligned with- and resisting the principal stresses that arise from a pressurized fibre-reinforced cylinder [31]. Given a cylinder wound with fibres of fixed length, this particular angle also generates the highest volume for the cylinder [31]. Wainwright *et al*. [17] applied this fibre-wound cylinder theory to the s. compactum of lemon sharks (*Negaprion brevirostris*) in order to explain the proposed exotendon function and how the s. compactum behaves under bending deformation during locomotion, but the precise operation of the s. compactum during swimming (or its exotendon mechanism) is still not completely understood. Subsequently, Hebrank & Hebrank [16] studied the possible exotendon function of the s. compactum in two species of teleost fish (Norfolk spot, *Leiostomus xanthurus* and skipjack tuna, *Katsuwonus pelamis*) as opposed to sharks. By examining the structure of the skin including collagen fibre

angles of the s. compactum and by performing uniaxial and biaxial tensile tests on the skin, Hebrank & Hebrank [16] suggested that s. compactum does not play a tendon role in teleosts, but their evidence of a lack of tendon function was inconclusive.

Naresh *et al*. [61] continued the investigation of possible tendon effects of the s. compactum, and revealed that the s. compactum of their model shark species (spadenose shark, *Carcharias laticaudus*), similar to the sharks and teleosts studied in [16, 17, 33], displayed a pattern of decreased collagen fibre angle towards the caudal end of the shark, and also a pattern of decreased crimping or waviness of collagen fibres towards the tail end. The elastin content of the s. compactum was also examined as an additional variable contributing to the differing properties of the skin along the A-P axis, with the anterior region containing a higher proportion of elastin. By performing tensile tests on specimens in different directions ("parallel" or along the A-P axis, "perpendicular" or along the dorsoventral D-V axis, and AV-PD and AD-PV "diagonal" orientations), the mechanical properties of the skin from the different A-P regions of the shark were explained in terms of its structure and more specifically by the collagen fibre and crimp angles, and the elastin content of the s. compactum. The histology results and mechanical properties of the s. compactum reported by Naresh *et al*. [61] for *C. laticaudus* shark skin were consistent with the original exotendon hypothesis proposed by Wainwright *et al*. [17] for the s. compactum of *N. brevirostris* shark skin. In Chapter 3, we provided a characterization of the structural and mechanical properties of the s. compactum from the common teleost fish, striped bass (*M. saxatilis*). We provided histological data (collagen fibre and crimp angles) in addition to tensile data for the s. compactum of this teleost fish that, similar to the results from Naresh *et al*. [61], were consistent with the original exotendon hypothesis proposed by Wainwright *et al*. [17]. In this chapter, we also report bending tests on whole striped bass fish (in the natural state),

descaled fish and descaled fish where the structure of the s. compactum was severely disrupted with laceration, to experimentally assess its mechanical contribution to bending and thus further explore the s. compactum exotendon hypothesis for striped bass fish skin.

5.2. Whole fish bending tests (scaled vs. descaled)

5.2.1. Material & methods

5.2.1.1. Sample collection & dissection

Whole, fresh striped bass (*Morone saxatilis*) fish, a common teleost from the northern Atlantic Ocean, were acquired from the local fish store and fish supplier described in Chapter 2 (section 2.4.1.1.), and were kept on ice before testing. All tests were commenced within a few hours of purchasing the fish specimens and the fishes were preconditioned by rinsing with cold tap water and gently flexing the fish for about 5 min before tests, in order to raise the temperature of the fish samples and bring them closer to physiological body conditions (the flexural rigidity of the samples was notably lower after preconditioning). With reference to De luliis & Pulera [85], the anterior and posterior dorsal fins and the caudal fin of the fishes were removed using large dissecting scissors. In order to track the position of the spine, about 20 push pins were inserted into the body of the fish along the mid-dorsal line from the tail region to the start of the cranium and spaced *ca*. 12.5 mm apart (Figure 5.1a). A hole was then perforated through the thickness of the body in the tail region below the last pin and in the dorso-ventral midline. Using large dissection scissors and following De luliis & Pulera [85], the opercular bones on the pharyngeal region on both sides of the fish were removed to expose the gills and pharynx, and a small passage was cleared through the thickness of the rostrum via the pharyngeal cavity.

The fish was placed belly down on an immersible support board, which consisted of a Plexiglas board covered with cm graph paper and plastic sheet, with a clamp fixed to one end of the board. The entire support board including the fish was submerged into a cooler of ice water and leveled so that the ventral half of the fish was underwater. Head-to-tail attachment first included inserting a treble fish hook through the hole in the tail so that the three points of the hook were securely embedded in the right side of the tail and the eye of the hook protruded through the left side of the tail. A precision extension spring was attached at one end to the eye of the treble hook, and braided steel wire was tied to the other end of the spring. The steel wire was then carefully fed through the fish's pharyngeal cavity from the left to right side of the rostrum, and connected to the clamp in a rope and pulley manner. The length of the head-to-tail attachment could then be adjusted by sliding the wire through the pharyngeal cavity, thereby inducing bending onto the body of the fish. The clamp on the convex side of the head was used to secure the wire and set the bending to a fixed desired position. The spring was selected carefully so that it provided enough stiffness to enable large fish bending while it was soft enough to enable sufficient extensions for accurate force measurements from image analysis. Prior to the test, the force-extension response of the spring was calibrated by attaching a series of weights and taking pictures and a stiffness of 0.623 N/mm was found. An Olympus digital camera (model no. C-5060) on a tripod was positioned over the cooler in order to take high-resolution images of the entire fish at each bending position.

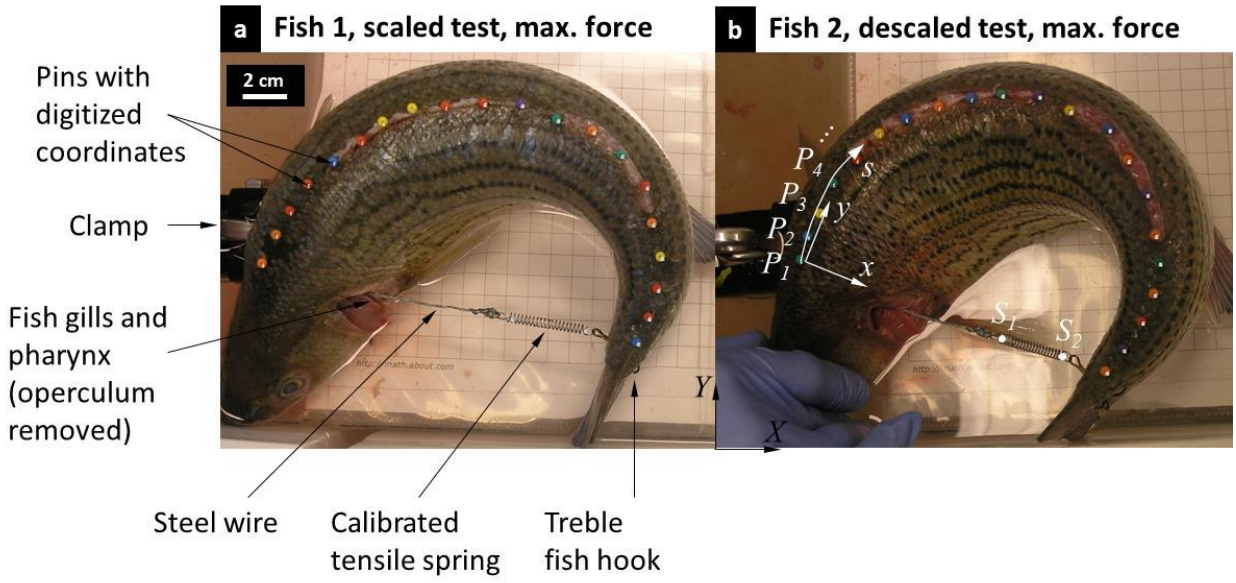

Figure 5.1. (a) Experimental setup for bending tests on a whole striped bass; (b) measurements from image analysis including: P_1-P_{20} (digitized pin coordinates), s (curvilinear coordinate), and S_1 and S_2 (spring coordinates).

5.2.1.2. Test procedure

Bending tests commenced with the fish in a near-straight body position and the wire slack. The wire was then pulled and the fish was bent until the wire was taut, and a first image was acquired. The wire was then pulled by small (*ca*. 1 N) increments, and a picture was taken at each bending position until a high body curvature was achieved. About 15 bending positions per test were recorded, and the maximum bending position was significantly larger than the amplitude during normal swimming and approached bending that occurs during sharp turns or escape responses (Figure 5.1) [86]. The test was performed two additional times on the same fish in order to check repeatability. Upon completion of the first three scaled (natural, intact) tests, the fish was entirely descaled by gently plucking the scales using tweezers. The fish was descaled across both lateral body surfaces from the head to the tail fin, up to the dorsum and across the whole ventrum. The fish was replaced atop the support board and in the cooler for

another three tests in the descaled state. In order to test for possible degradation of properties, another "control fish" was tested in bending at the very beginning of the test session, and subjected to the same temperature and hydration as the tested fish. The control fish was tested again at the very end of the session. No change in properties was observed in the control fish, and therefore no significant degradation of properties occurred over the course of the testing session.

5.2.1.3. Image analysis (coordinate selection)

Image analysis was used to compute the curvature (C) and bending moments (M) along the fish. The coordinates (X,Y) of the centres of the pins (points P_1 through P_{20} in Figure 5.1b) were digitized at high magnification (with single pixel resolution, and the pin containing hundreds of pixels) using the software Plot Digitizer version 1.9 (http://plotdigitizer.sourceforge.net/) and converted to mm using the graph paper. The coordinates of the two points S_1 and S_2 positioned on either side of the spring precisely at the base of the eyes of the spring (with single pixel resolution) were also recorded (Figure 5.1b). These coordinates were then processed using the software Matlab version R2011b. The coordinates of the points were first transformed into the (x,y) coordinate system, with the x axis aligned with the spring and the origin corresponding to the intersection between the axis of the spring and the mid-dorsal line on the fish's head (Figure 5.1b). The angle for transformation was computed from the coordinates of the points S_1 and S_2. The procedure was repeated for each image, producing a series of fish profiles in the (x,y) coordinate system (Figure 5.2).

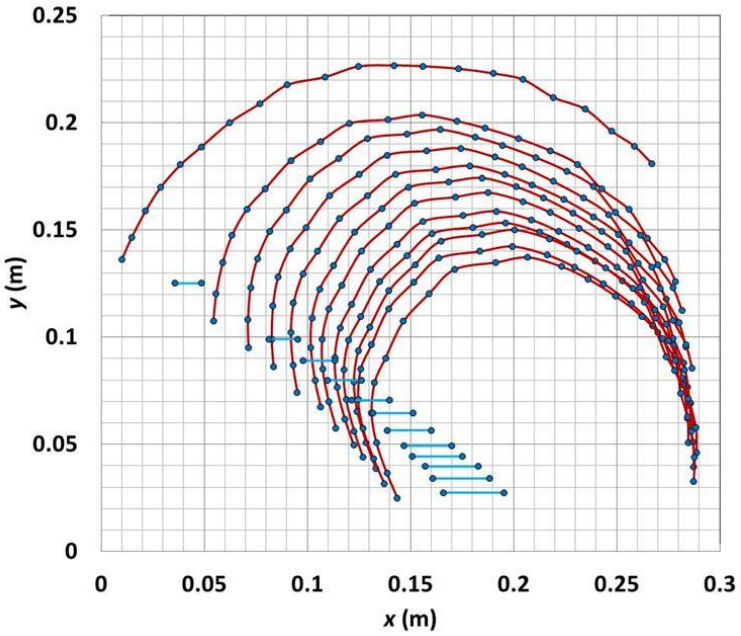

Figure 5.2. Fish profiles in the (*x*,y) coordinate system. Each data point corresponds to a digitized pin coordinate (P_1-P_{20}) with the axis of the spring (blue lines) aligned with the *x* axis and the origin set as the intersection between the line of force and the mid-dorsal line on the fish's head. Fish profiles for increasing force increments are shown from left (0 force) to right (maximum force).

5.2.1.4. Data analysis (curvature & moment calculations)

In this framework, the head of the fish is fixed, and bending is induced by displacing the tail region along the *x* axis in the negative direction. The curvilinear coordinate *s* of each pin was also computed using the *x* and *y* coordinates. The curvature of the fish was then determined as a function of the curvilinear coordinate *s*, by fitting a circle onto a segment of the profile of length Δs centered on the point where curvature is to be determined. The curvature (mm^{-1}) was then simply determined by computing the inverse of the radius of the circle. Figure 5.3a shows the local curvature of the fish as a function of position along the fish (curvilinear coordinate *s*) as computed from the profiles of Figure 5.2. The coordinates of the points S_1 and S_2 were used to compute the extension of the spring, which was in turn used to calculate the tensile force.

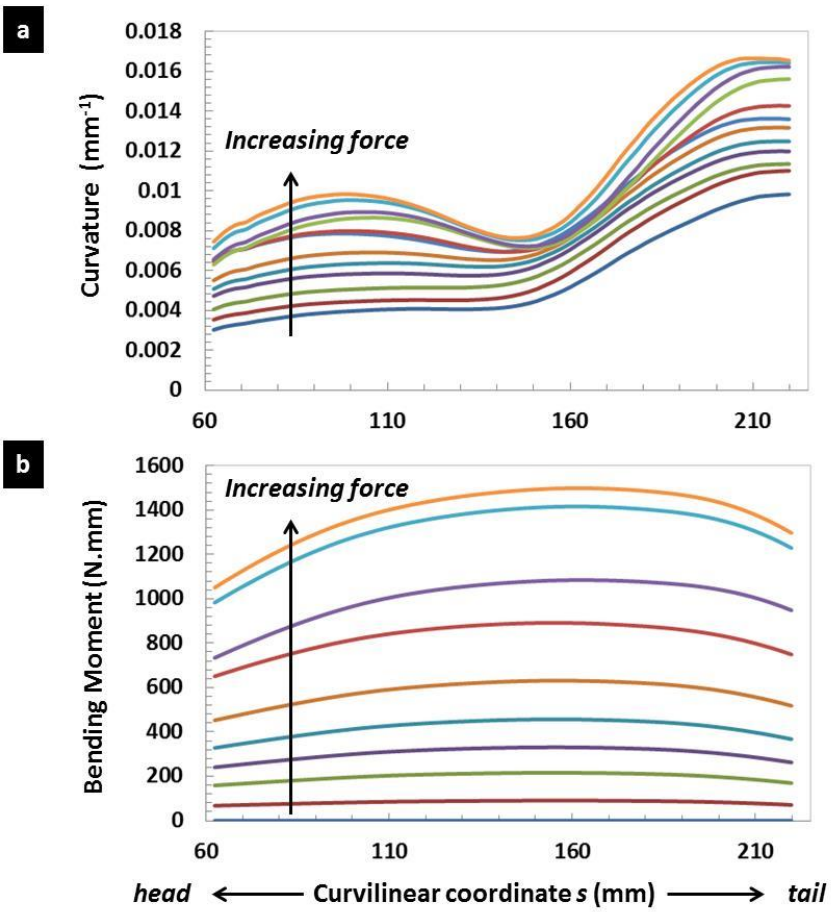

Figure 5.3. (a) Local curvature *C* of the fish as a function of curvilinear coordinate *s*; (b) local bending moment *M* of the fish as a function of curvilinear coordinate *s*. Arrows labeled "increasing force" indicate the fish being flexed from the initial bending position (bottom curve) to the maximum bending position (top curve) during a single bending test.

A convenient way to reveal the internal forces and moments in the system is to consider a virtual cut along the spring and along the fish at point *C* (Figure 5.4). This "virtual cut" on the fish was taken along a cross section perpendicular to the mid-dorsal line of the fish (in the transverse plane), but not necessarily perpendicular to the spring. A free body diagram of the resulting system is shown in Figure 5.4. The application of a force *F* along the axis of the spring must be balanced by internal loads within the fish, exposed by the virtual cut at point *C*.

Following conventions used for the bending of beams, these internal loads are represented as a normal force *N*, a shear force *V* and a bending moment *M* (Figure 5.4). For the rest of the analysis we assumed that the normal and shear forces induce negligible deformations compared to the bending generated by the moment *M*. Only the moment *M* is then considered and its magnitude is simply given by $M=F \cdot y_C$, where y_C is the vertical coordinate of point *C* (Figure 5.4). Figure 5.3b shows the local bending moment as a function of curvilinear position along the fish. For a fixed bending position and force in the spring, the middle region is subjected to the highest bending moment because it is the furthest from the line of action of the spring (i.e. *x* axis). As the bending increases, the bending moment at any point along the fish increases because both the tensile force in the spring and the distance from the line of action increase.

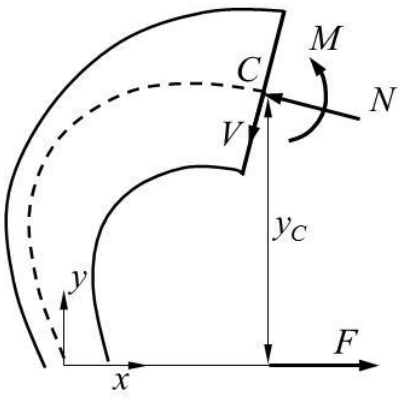

Figure 5.4. Free body diagram of the bent fish showing: *C* (location of virtual cross section), *V* (shear force), *M* (bending moment), *N* (normal force), y_C (distance from *x* axis to point *C*), *F* (force acting on the spring).

5.2.2. Results

5.2.2.1. Bending moment vs. curvature at three locations

This analysis therefore produces a rich set of data where the curvature and bending moment are known at any point along the mid-dorsal line. Figure 5.5 shows *M-C* curves as measured at three locations (*s* distances) along the mid-dorsal line: at 100 mm in the rostral region, at 150 mm in the trunk region, and at 180 mm in the caudal region for fish sample #1, and at 80 mm, 110 mm and 150 mm for fish sample #2. A similar shape was observed for *M-C* curves from all three regions of the fish. For low curvatures, the fish is highly flexible and requires negligible force to bend. At higher curvatures, a significant stiffening is observed, up to a maximum curvature. A rightward shift in the *M-C* curves and decrease in slope or stiffness along the *M-C* curve was not observed upon descaling of the fish, as the scaled and descaled fish displayed similar results. Any potential decrease in flexural stiffness after descaling of the fish is small or negligible and was not detected with this experimental setup.

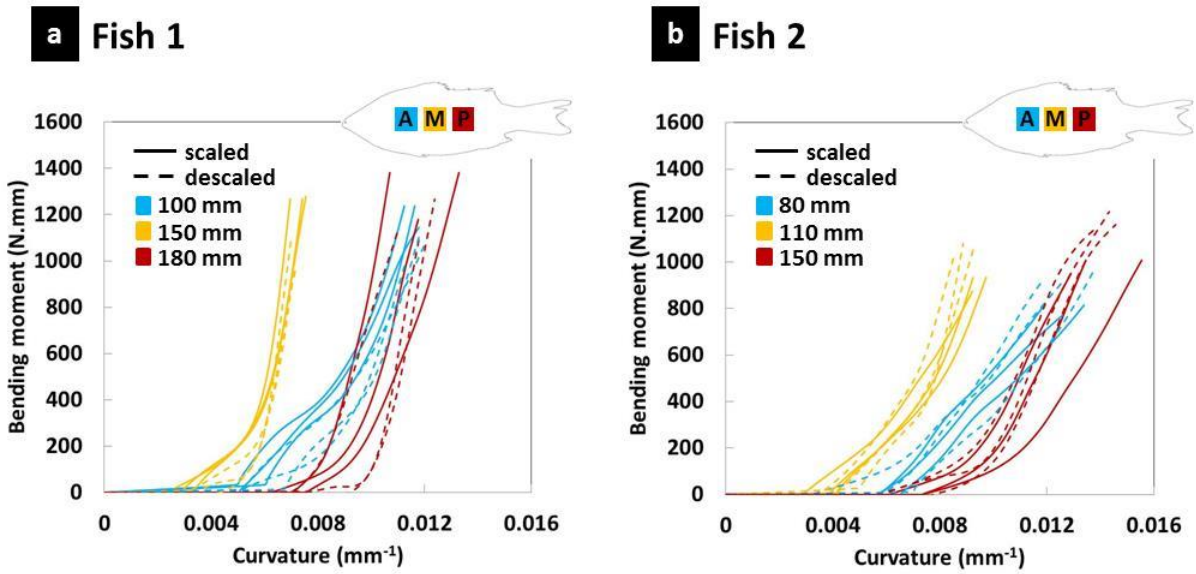

Figure 5.5. (a) *M-C* curves at three locations along the mid-dorsal line of fish sample #1: at 100 mm in the anterior region, at 150 mm in the mid region, and at 180 mm in the posterior region; (b) *M-C* curves at 80 mm, 110 mm and 150 mm for fish sample #2.

5.2.2.2. Bending moment vs. curvature vs. curvilinear distance

Comparison of *M-C* curves along the entire curvilinear length of the fish revealed a trend in the data. Although curves of similar shape were observed at different points along the mid-dorsal line of the fish, the curvature at (initial) stiffening and the stiffness varied with position. Figure 5.6 shows a more comprehensive representation of the flexural behavior of the whole fish, consisting of a surface in the (*s*,*C*,*M*) space. This 3D plot of *M* versus *C* along the entire curvilinear length of the fish reveals an obvious pattern in the *M-C* curves in that lowest curvature at stiffening and highest stiffness occurs near the middle or trunk portion of the fish centered at a curvilinear distance of *ca*. 150 mm. This region of higher stiffness manifests as a distinct ridge on the surface plotted in 3D space, the ridge tapering off in both anterior and posterior directions towards the softer head and tail regions.

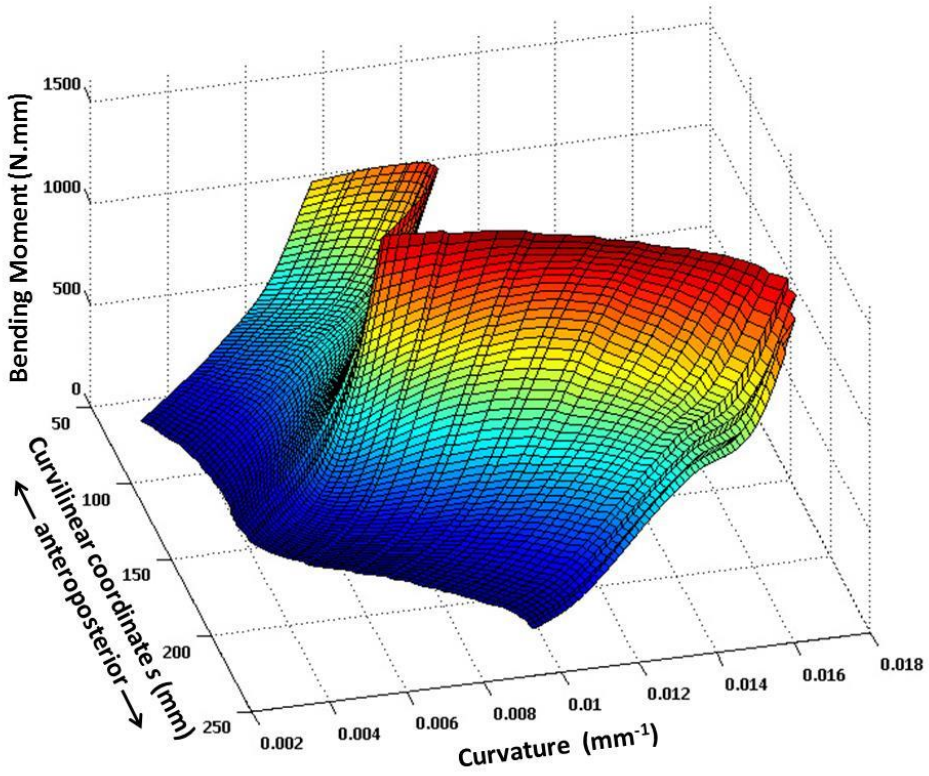

Figure 5.6. Surface plot of *M-C* curves along the entire curvilinear length (*s*) of the fish.

5.3. Whole fish bending tests (descaled vs. incised)

5.3.1. Material & methods

5.3.1.1. Sample collection & dissection

The dissection procedure and experimental setup employed in this section to perform whole fish bending tests were the same as in section 5.2.1.1.

5.3.1.2. Test procedure

Bending tests started with the fish in a straight body position. The wire was then pulled by small (*ca*. 1 N) increments, and a picture was taken at each bending position (*ca*. 15 positions per test) until a high body curvature was achieved. The descaled fish was first tested three times with intact s. compactum (control group), and then tested three times with the s. compactum disrupted. Using a 500 µm control-depth surgical knife (Shreeji Micro Systems Inc., Gujarat, India), nine vertical incisions were made to the skin on both sides of the fish from the head to the tail region (Figure 5.7). The incisions were *ca*. 32 mm in length and had an anteroposterior (A-P) spacing of *ca*. 25 mm. Use of the 500 µm control-depth knife allowed precise targeting and disruption of the s. compactum layer of the skin without significant damage to the underlying muscle, because our histology results suggest that the hypodermis, the intervening tissue layer between the s. compactum and underlying muscle, is on average located at a depth of *ca*. 500 µm from the skin surface. It was previously demonstrated in section 5.2.1.2. that no significant degradation of properties occurs over the course of the bending tests.

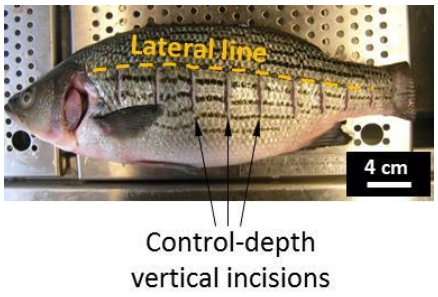

Figure 5.7. Fish specimen used in bending tests showing control-depth incisions made to the s. compactum.

5.3.1.3. Image analysis (coordinate selection)

5.3.1.4. Data analysis (curvature & moment calculations)

The image and data analyses used in this section to analyze the whole fish bending test data were the same as in sections 5.2.1.3. and 5.2.1.4.

5.3.2. Results

5.3.2.1. Bending moment vs. curvature at three locations

Figure 5.8 shows bending moment-curvature (*M*-*C*) curves measured at three locations (*s* distances) along the mid-dorsal line (A-P axis): 100 mm in the anterior region, 140 mm in the mid-region, and at 180 mm in the posterior region. Although the mid-region of the fish exhibits the stiffest flexural response (lowest curvature at stiffening and highest stiffness), *M*-*C* curves display a similar shape at all three A-P regions of the fish. At low curvatures, a soft flexural response is observed, whereas at higher curvatures, significant stiffening occurs. A rightward shift of the *M*-*C* curves and decrease in flexural stiffness along the *M*-*C* curve was observed at all three A-P locations upon s. compactum incision, but was more pronounced for the thinner A

and P ends of the fish (Figure 5.8). These experiments demonstrate that the s. compactum therefore carries a significant portion of the bending moment.

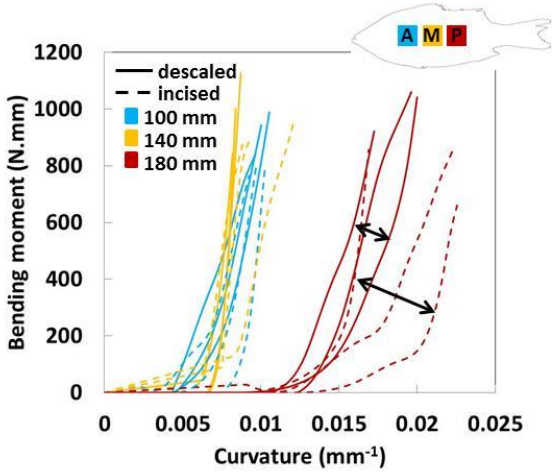

Figure 5.8. Bending moment-curvature (*M-C*) curves at three locations along the mid-dorsal line (anteroposterior, A-P, axis): 100 mm in the anterior region, 140 mm in the mid-region and 180 mm in the posterior region, for a striped bass fish in both "descaled" and s. compactum "incised" conditions, (black arrows indicate the rightward shift of *M-C* curves at 180 mm after s. compactum incision).

5.4. Striped bass body morphometrics

5.4.1. Material & methods

In order to measure the body dimensions of a typical striped bass specimen, whole-body morphometrics were measured using a series of metal rings (Figure 5.9) and image analysis employing the software ImageJ version 1.46r (http://rsb.info.nih.gov/ij/) and MomentMacroJ version 1.3. Images of the rings were analyzed to measure cross-sectional area (*XSA*) (area of transverse sections) and second moment of area with respect to the y-axis (I_y) (dorsoventral axis), along the anteroposterior axis of the fish relative to the fish's lateral line system. The *X*,*Y* coordinates where the rings contacted the lateral line (Figure 5.9) were digitized using the software Plot Digitizer version 1.9 (http://plotdigitizer.sourceforge.net/).

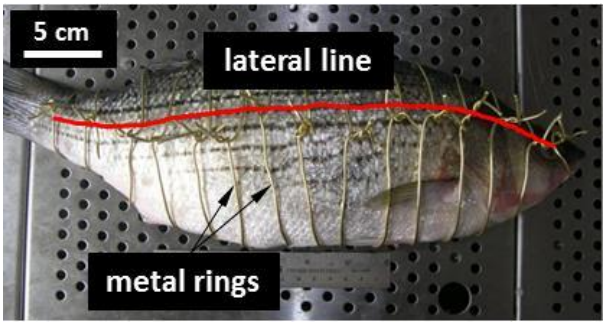

Figure 5.9. Experimental setup for measuring striped bass body morphometrics.

5.4.2. Results

Both *XSA* and I_y increased and decreased in a parabolic fashion along the anteroposterior length of the fish, with peak *XSA* = *ca*. 6 cm^2 and I_y = *ca*. 4 x 10^6 mm^4 occurring in the middle trunk portion of the fish at a curvilinear length of *ca*. 150 mm (Figure 5.10).

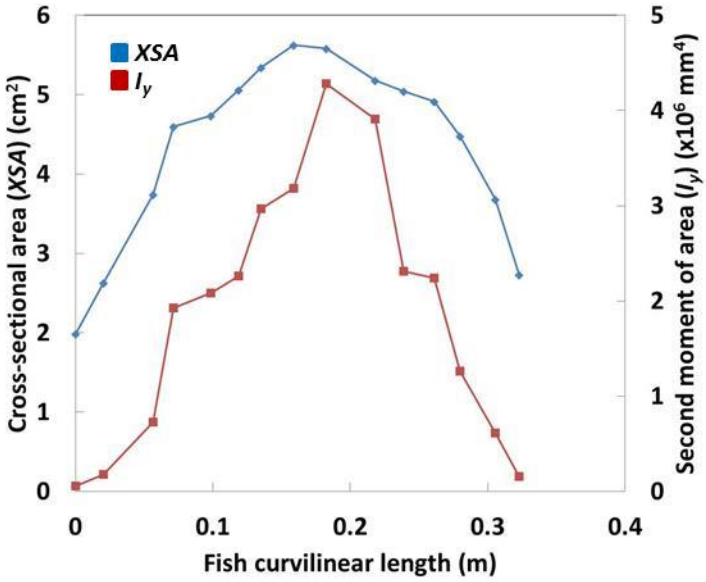

Figure 5.10. *XSA* and I_y as functions of fish curvilinear length along the lateral line system (anteroposterior axis).

5.5. Discussion

The nonlinear flexural behavior of striped bass observed in this chapter is similar to the results reported by Long *et al*. [84] on longnose gar (*L. osseus*). The *M-C* curves produced by Long *et al*. [84] for gar fish exhibit the same general shape as we observed for striped bass. However, whereas maximal curvature is similar for both fish types (16 m^{-1} for the tail region of striped bass and 35 m^{-1} for gar), the maximal bending moment measured by Long *et al*. [84] (*ca*. 0.04 N.m) is 35 times lower than observed for striped bass (*ca*. 1.4 N.m). This is likely due to the similar length, but substantially lower diameter of longnose gar compared to striped bass. Similar effects of body size and cross-sectional shape on body flexibility were demonstrated by Aleyev [87], and described by Tytell *et al*. [88], using a variety of fish species ranging from slender anguilliform to thicker carangiform (fusiform) body type. The effect of body size on flexural stiffness is not only seen across species of differing body types, but also along an individual fish of a certain species if *XSA* varies along the fish. The most evident variable that changes with anteroposterior body position for striped bass that could affect local flexural stiffness is thickness of the body itself or body *XSA*, which seems to be a reasonable explanation for the markedly higher stiffness values recorded for the thick mid-portion of the striped bass fish. *XSA* and I_y increase markedly along the anteroposterior axis of a typical striped bass specimen from either end of the fish to the middle trunk region. The 3D surface plot of *M-C* along the length of striped bass differs from expected results for an object of cylindrical shape (nearer to the gar fish body type), which should exhibit uniform flexural stiffness along the length of the cylinder.

Long *et al*. [84] not only performed bending tests on longnose gar in the scaled condition (skin intact), but also after dermal incisions followed by partial descaling of the fish (removal of a scale row). A rightward shift of the *M-C* curve was observed after these ablation treatments and

significant decrease in flexural stiffness (measured 10 m^{-1} past the end of the "neutral zone") of the fish was determined. An insignificant decrease in flexural stiffness was observed after partial descaling of the fish. These results demonstrate an effect of dermal incision and suggest a possible small effect of descaling on the flexural stiffness of the gar fish. However, in this chapter, no decrease in flexural stiffness upon descaling was observed for striped bass, and this is not surprising given the thicker and more heavily mineralized ganoid scales of the gar fish and its slender body. The effect of descaling on flexural stiffness of striped bass is negligible or undetectable using this experimental setup, and suggests that interlocking of scales during undulatory locomotion does not serve an important mechanical role by acting as a whole body exotendon and facilitating muscle contraction during swimming. The experiments on striped bass employing probe tests of the body surface and digital image correlation, which were reported in section 4.3.2.7., revealed the mechanical interaction of fish scales and their local effects on puncture resistance. However, this work demonstrates that the mechanical interaction of scales at high body curvatures during swimming has minimal effects on flexural stiffness and thus swimming mechanics, which, similar to the decreased size and weight of teleost scales compared to primitive scale types, may be an adaptation for improved speed, flexibility and manoeuverability of teleost fishes (Chapter 4). These results for striped bass are the first to reveal a lack of an exotendon effect provided specifically by the scales during locomotion. Whereas previous authors have also suggested the absence of an external tendon effect for the intact skin (including scales and underlying dermis) of other teleosts such as the Norfolk spot (*Leiostomus xanthurus*) and the skipjack tuna (*Katsuwonus pelamis*) [16], we also investigated using the methods developed here whether or not the subjacent dermal tissue (s. compactum) in striped bass functions in the locomotion of this teleost fish via an exotendon effect.

The examination of the contribution of the s. compactum to whole body flexural stiffness was comparable to Long *et al*. [84]. The ablation treatments used by Long *et al*. [84] caused a rightward shift of the *M-C* curve measured for longnose gar that was similar to the decrease in flexural stiffness observed in this chapter for striped bass after incision to the s. compactum. For the s. compactum to function as a tendon-like energy storage device and assist with fish locomotion, it is necessary that it stores and releases sufficient strain energy to facilitate muscle contraction. This energy storage and recovery capability was supported for the s. compactum of striped bass by the reduction in body flexural stiffness after s. compactum incision, which would likely also result in decreased energy absorbed at maximum curvature of the fish. It is also necessary that the energy is stored and recovered at the correct stages in the fish locomotory cycle, which highlights the importance of the "neutral zone" [84], or initial compliant response of the fish upon flexure before stiffening occurs at high body curvatures.

The shape of stress-strain curves from tensile tests on descaled fish skin in the A-P direction (Chapter 3) closely resembles that of *M-C* curves from whole fish bending tests, during which the fish exhibits an initial compliant flexural response followed by significant stiffening, and both stress-strain and *M-C* curves resemble the stress-strain curve of mammalian tendon [31]. Although the tensile behavior of the s. compactum as part of the intact integument during fish locomotion may differ somewhat from that of isolated skin specimens tested in tension along the A-P axis, the tensile response observed for such isolated samples conformed to the general hypothesis of s. compactum exotendon function, which requires an initial compliant phase permitted via shearing of lamellae (and alignment of collagen fibres) and un-crimping of collagen fibres as described by [8, 9, 17, 61], followed by marked strain hardening or stiffening from collagen fibre recruitment that allows sufficient energy absorption and recovery to assist

with the subsequent stage of locomotion. During fish swimming, the s. compactum would operate in a similar manner on the convex side of the fish allowing for the initial compliant phase or "neutral zone" [84] observed for *M-C* curves from whole fish bending tests and producing an initial low flexural stiffness. The stiffening observed near the end of *M-C* curves was suspected to arise in part from the s. compactum if the skin is indeed functioning as an external tendon. The contribution of the s. compactum to flexural stiffness of the fish at high strains or body curvatures was demonstrated from the incision experiments, which inhibited s. compactum function and resulted in decreased stiffness and likely energy absorption, thus supporting the exotendon hypothesis.

In conclusion, the mechanical interaction of teleost fish scales plays an important role in the puncture resistance of fish skin by distributing the force upon puncture and protecting soft underlying tissues (Chapter 4). However, in this chapter we demonstrated that the scales contribute a negligible amount of body flexural stiffness and therefore do not function in whole fish swimming mechanics by acting as an external tendon during locomotion. The relatively weak mechanical interaction of scales at high body curvatures and thus negligible contribution to flexural stiffness of the fish is a possible adaption for the enhanced speed and flexibility of modern teleost fishes. Instead, the s. compactum layer may provide the skin with tendon-like properties that enhance locomotion. The tensile response of fish skin stretched in the anteroposterior direction is generated by two main histological features and mechanisms of the s. compactum, the angle of fibres composing the collagen cross-ply and the crimping of collagen fibres. These structural characteristics of the s. compactum produce the tendon-like response of the skin (Chapter 3), including an initial compliant phase and a subsequent stiffening phase that may result in the storage and recovery of elastic strain energy, thus promoting muscular

contraction and providing the skin with an external tendon function. The structural and tensile properties of the s. compactum vary across the anteroposterior axis of the fish, with the skin in the dorsal and tail regions displaying the stiffest and strongest responses, suggesting possible differences in function for the different regions of the fish. In this chapter, we demonstrated that the s. compactum also increases the flexural stiffness of the fish, which further supports a tendon-like, energy storage device role of this layer of the skin. As well, the s. compactum accounts for a large portion of the puncture resistance of the intact scaled skin (Chapter 4), which suggests an additional role of the s. compactum of teleosts in the mechanical protection against predator bites. The structural and mechanical properties of the s. compactum of striped bass skin, in conjunction with research on the puncture and bending mechanics of the scaled skin, will now be used in the biomimetic design of artificial materials and systems inspired from teleost fish skin that replicate the range of desirable properties exhibited by this high-performance natural material, including light weight, flexibility, high protective capacity (or puncture resistance), and mechanical energy storage and recovery capability (or tendon-like properties).

CHAPTER 6

GENERAL DISCUSSION & FUTURE WORK

6.1. Thesis contributions

(i) In the second chapter of this research, the tissue design of fish scales from striped bass (*M. saxatilis*) was shown to be similar to the general structure of teleost scales, including upper and lower mineralized portions of the scale, an uneven calcification front, and collagen cross-ply structure throughout the scale thickness. However, features unique to *M. saxatilis* scales were also observed, such as the radial-circumferential arrangement of collagen fibres that produces a near-orthogonal pattern at the microscale where the fibres cross over. As well, the conical shape of the scale was demonstrated using micro-CT, and the thickness distribution of the scale in combination with the observed scalation pattern of uniform 3-scale overlap, also suggested a uniform "effective thickness" of the scaled portion of the skin across the surface of striped bass. The structure of the skin was examined in cross section using histological staining and image analysis to reveal the arrangement of the scales within the upper s. spongiosum layer of the dermis and to characterize the main structural features of the underlying dermal s. compactum, including the angle of the cross-helical collagen fibres and the degree of crimping of the fibres at different locations along the long axis of the fish. The structural features of the scales and s. compactum of the integument from striped bass were then related to the mechanical properties of the skin and whole fish measured in the subsequent chapters in order to investigate potential mechanical functions of the scales and s. compactum in striped bass.

(ii) In the third chapter of this research, the tensile properties of the scales and skin from striped bass were first examined by performing tensile tests on individual scales and revealing energy dissipative mechanisms of the scale. As well, by performing tensile tests on descaled skin from the same locations (and in different orientations) as the histological evaluation of the s.

compactum at different sites along the anterorposterior axis of the fish that was conducted in the previous chapter, aspects of the hypothesized exotendon mechanism of the s. compactum were explained to be generated by the local structure of the s. compactum including the angle of the cross-helical collagen fibres and the amount of crimping in the fibres. Both of these structural characteristics of the s. compactum, in addition to other potential tendon-like mechanisms such as elastin tissue content and molecular kinking of collagen fibrils, permit the initial flexible phase of the bending response via shearing of collagen fibre lamellae, and alignment and un-crimping of the collagen fibres, followed by strain hardening due to collagen fibre recruitment. Differences in the structure and tensile properties of the s. compactum along the long axis of the fish may be due to differences in the exotendon role and multifunctionality of the s. compactum layer across the length of the fish. The tendon-like structure and tensile properties of the s. compactum supported an external tendon function of the s. compactum in teleost fish skin, which was further explored in the fifth chapter of this work.

(iii) The fourth chapter of this research provided several original contributions to the understanding of the puncture mechanics of individual teleost fish scales and the intact scaled skin of striped bass. Perhaps the largest contribution from this chapter was the demonstration of the precise puncture mechanism displayed by individual scales upon penetration with a sharp probe simulating a predator tooth. A puncture sequence, generated from the mineralization pattern and cross-ply structure of the scale, was revealed that consisted of the production of four bony flaps in the upper layer, delamination of both layers, and biaxial tension imposed upon the lower collagenous retaining membrane by the mineralized flaps. This mechanism of puncture at the level of the scale was shown to increase the penetration resistance of the scale beyond that of

common, protective engineering polymers such as polycarbonate. The high puncture performance of individual scales and the ‘four flaps’ mechanism producing the optimized penetration resistance of teleost scales are now being reproduced into high-performance artificial fish scales with additional similar properties as teleost scales, such as light weight and transparency.

The puncture properties of striped bass skin and underlying mechanisms were also investigated at the macroscale and level of potential scale interaction in contrast to the failure mechanisms upon puncture of individual teleost scales. Collaborative mechanisms occurring between the scales during a puncture event, and the contributions of surrounding tissues of the skin to puncture performance, were evaluated and main factors and mechanisms were revealed that control the enhanced penetration resistance of the intact scaled skin. Possible mechanisms of the skin that were rejected due to negligible contribution to puncture performance included substrate stiffness, friction between scales and local scale arrangement. The particular site of puncture on the scale, including effects of scale thickness distribution and local features, was shown to be an important factor, which was also shown to be mediated by the specific scalation pattern and number of overlapping scales developed by the teleost fish. The factor with the largest influence on the penetration resistance of the skin, however, was found to be the deformation and mechanical interaction of the scales that resulted in a significantly lower deflection of the skin in comparison to non-overlapping scales, which could potentially cause blunt damage to fragile underlying tissues before rupture of the protective layer occurs. The interacting scales were shown to distribute the force upon puncture over larger tissue volumes, therefore limiting deflection of the skin and protecting soft underlying tissues. This collective scale mechanism is possibly the most important function of the overlapping arrangement of the

scales in serving as a flexible, protective layer that also minimizes deflection of the skin. The attributes and puncture properties of the intact scaled skin of teleosts, including collaborative mechanisms occurring within the skin upon puncture, are being modeled and integrated into the biomimetic design of synthetic protective systems with similar puncture resistant and robust characteristics as determined for striped bass fish skin.

(iv) The fifth chapter of this work originated from the main observation and underlying mechanical theory of teleost fish scale interaction upon puncture that were described in the previous chapter on fish skin puncture mechanics. The model of fish scale interaction with force dispersal during a puncture event was described as being applicable not only to puncture events, but also to the undulatory locomotion of modern teleost fishes. In this scenario, at the end of a swimming stroke and at high body curvatures, the scales on the inner compressed side of the flexed fish deform and have the potential to interact as a system that collectively increases the flexural stiffness of the whole fish. However, it was found that the collective contribution of the scales to whole body flexural stiffness of the fish was negligible and, and therefore it is unlikely that the scales function as an external tendon during locomotion in this teleost fish. The overall flexural response of the fish (or its bending moment versus body curvature curve), though unaffected by the descaling treatment, resembled the tensile response of tendon in that an initial compliant phase was observed, which allows initial flexibility or range of motion, followed by a marked stiffening phase, which permits energy absorption and subsequent recovery to facilitate muscle contraction and the next stage of the locomotory cycle. The maximum flexural stiffness of the fish was recorded at the thick middle portion of the fish, which suggested effects of local body dimensions on flexural properties. The tendon-like flexural response of the fish, including

the substantial stiffening phase at high body curvatures, was shown not to arise from the mechanical interaction of scales and therefore, it was suspected that the underlying thick, collagenous s. compactum layer of the skin might be partially responsible for the observed strain hardening phase of the whole body flexural response. The lack of a contribution of the scales to the total flexural response of the fish may be adaptive in allowing the full range of motion necessary for effective undulatory locomotion in teleost fishes.

This chapter also involved an investigation into the potential exotendon function of the dermal s. compactum layer of teleost integument. Knowledge of a lack of an effect of the stiff dermal scales on flexural properties and likely swimming performance and previous studies on the possible energy storage device role of the s. compactum in cartilaginous fishes motivated a closer and more thorough analysis of the mechanical properties of this integumentary layer and its effects on whole fish bending and locomotion. The same methods followed to assess the contribution of scales to whole fish bending mechanics were applied to assess the contribution of the s. compactum, and a significant reduction in body flexural stiffness was observed after selective incision to the s. compactum. This finding confirmed the predicted effects of the s. compactum on fish bending mechanics and supported an external tendon role of the s. compactum in this teleost fish to promote swimming efficiency. The exotendon mechanism and mechanical energy absorption and release capabilities of the s. compactum layer of striped bass fish skin are now receiving further characterization and modeling in order to incorporate this additional mechanical role of teleost integument into the design and manufacture of artificial protective skins with diverse functions.

6.2. Biomimetic design of protective systems inspired from fish skin

The purpose of this research was to characterize the structure and mechanical properties, including the puncture resistance and tensile properties, of teleost fish scales and skin to provide a foundation and the information needed for the first steps towards the eventual design and fabrication of biomimetic protective materials and systems inspired from the properties of teleost integument. An understanding of the composition and architecture of the scales and the intact skin was first required and the detailed structure of the skin, which conformed to general models of scale and skin structure and revealed novel structural observations, was shown using a variety of techniques including histological processing and staining, atomic emission spectroscopy, optical and scanning electron microscopy, micro-computed tomography, and three-dimensional image correlation. Through this structural characterization of teleost skin using the model species striped bass (*M. saxatilis*), and by means of extensive literature review, structure-property relationships were predicted, for example the function of the orthogonal plywood pattern of collagen fibres in the lower 'collagen' layer of the scale was suspected to be the resistance to biaxial tension somehow imposed on the collagen layer by the overlying 'bony' layer of the scale. Knowledge of the fine structure of the scale and skin of striped bass was then combined with mechanical testing of the same natural materials to investigate the underlying mechanisms responsible for the observed enhanced mechanical properties of teleost skin.

The penetration resistance of the scale was measured to be superior to that of protective engineering materials such as polycarbonate and shown to arise from a specialized mechanism and interaction between the bony and collagen layers of the scale upon puncture with a sharp probe similar to a predator tooth. This puncture mechanism of the scale consisted of the induction of four bony flaps by the probe tip, which then imposed the predicted biaxial tension

upon the lower collagen layer that, in reaction, offered resistance to the biaxial tension from the flaps due to the orthogonally arranged collagen fibres. The structure of the scale, including the mineral distribution pattern and the collagen cross-ply structure, was shown to be essential for the initiation of this puncture sequence, which maximizes the penetration resistance of individual teleost scales. However, a comprehension of the structural and mechanical design of teleost fish skin requires examination of possible mechanisms of puncture resistance operating at all levels of the integument and not just the mechanics of the isolated scales. The next stage of this research on the puncture mechanics of teleost skin, therefore, consisted of an investigation of the puncture performance of the intact scaled skin with contributions from neighboring and interacting scales. Collective scale and skin mechanisms were explored using similar puncture test methods and various other techniques, and the mechanical interaction of the scales and with their surrounding connective tissues was studied and modeled. The factor at the macroscopic level with the largest influence on the overall puncture performance of the skin was the prevention of excessive deflection of the skin by the progressive interlocking of scales, which potentially protects soft underlying tissues such as musculature from blunt trauma before penetration of the scales occurs. This mechanism of scale interaction with puncture force dispersal and restricted deflection of the skin allows for both high puncture force and stiffness of the skin, which could be important for the protection of inner tissue layers. In addition to the collaborative mechanisms occurring between the scales during a puncture event to limit skin deflection, a substantial contribution to the penetration resistance of the skin by the basal s. compactum layer was also demonstrated.

The same model of teleost scales during puncture was also applied to the study of the possible extra mechanical function of the scales during teleost locomotion by serving as a whole

body exotendon that increases the efficiency of swimming. The flexural properties of whole teleost fish are critical to the swimming performance of the fish, and thus cooperative interactions between the scales that contribute significantly to the bending properties of the fish could potentially function to improve swimming performance. In this context, the scales on the inner compressed side of a flexed teleost fish during undulatory locomotion were proposed to function as a whole body external tendon that stores and releases strain energy to facilitate the subsequent muscle contraction and swimming stroke. The findings from whole fish bending tests, however, demonstrated that the scales contribute negligibly to the flexural stiffness of the fish, and thus that these protective features of the skin likely do not function additionally in enhancing swimming performance. Alternatively, the subjacent dermal s. compactum layer of the skin was suspected and examined as the probable source of the tendon-like bending properties of the whole fish. Similar fish bending tests, but with incisions made to the s. compactum in addition to descaling, determined a significant effect of the s. compactum on body flexural stiffness, which supported the exotendon function of the s. compactum and its cross-helically arranged collagen fibres during fish locomotion. Further evidence of an exotendon role was provided from tensile tests on s. compactum specimens along the length of the fish with corresponding histology at the same locations. The local structural features of the s. compactum were shown to generate the observed tendon-like, tensile response of this tissue layer, which was consistent with previous studies on the external tendon role of the s. compactum in shark skin [17, 61]. The multifunctional nature of teleost fish skin and its diverse properties, such as high protective capacity and additional locomotory function, was highlighted by this study on the exotendon properties of the s. compactum layer of teleost integument.

The main reason for this work was to characterize the structure and mechanics, including the penetration resistance and flexural properties, of teleost fish scales and skin to supply the research necessary for the initial stages of the biomimetic design of protective systems inspired from fish skin. Insights were revealed into the puncture and bending mechanics of teleost skin and whole fish, with the specific aim of elucidating the adaptive features and mechanisms controlling the optimized performance of the skin in the resistance to mechanical perturbation and in the efficient locomotion of the fish. Mechanisms occurring within the skin during a puncture event and during flexure of the fish, with particular contributions from the dermal scales and s. compactum, were shown to increase the penetration resistance of the skin over multiple levels of hierarchical structure, and to impart the skin with tensile properties that function in concert with the musculature to maximize the efficacy of the undulatory form of locomotion employed by the fish. With these mechanisms outlined at the macro- and microscales, and with insights from experimentation on collagen fibrils at the molecular level [89], the focus of this line of research has now shifted to the effective replication of fish skin structures and mechanisms into bio-inspired protective and flexible coverings that display a range of capabilities similar to the properties of teleost skin such as light weight, transparency, breathability, and additional mobility functions. The future direction of this biomimetic research is thus to explore pathways to fabricate protective and locomotory systems inspired from teleost fish skin.

To this aim, early prototypes and preliminary puncture tests have been performed on artificial fish scales that mimic the general structure and mechanical response of teleost scales upon sharp penetration. Initial results [28] are encouraging in the construction of thin and light weight, bilayered scales with upper stiff and lower compliant phases made from engineering

materials with properties comparable to those of the natural fish scale, and in the reproduction of a similar failure mode with a cross-pattern style of failure followed by a ‘four flaps’ mechanism of puncture resistance. The improved design and puncture performance of these artificial scales is an active area of research within the biomimetic fabrication of protective, flexible membranes modeled after teleost fish skin. While reproduction of the puncture mechanism of individual teleost scales is in progress, advancements have also been made in the replication of mechanisms operating at the level of the intact fish skin, with an initial focus on the collective mechanisms occurring between the interacting scales during indentation and penetration of the skin. A biomimetic approach to the study of fish skin was conducted by Browning *et al*. [78], who investigated the puncture resistance of teleost skin utilizing a two-dimensional polymer model of scale interaction upon puncture, in order to examine collaborative scale mechanisms and puncture properties of the skin. More recently, Vernerey *et al*. [29], and Vernerey & Barthelat [30], reported on the mechanical design of teleost skin and the development of synthetic, flexible armors with similar properties as fish skin using a computational approach and incorporating the puncture properties of the skin that were determined in this work. Corresponding research has been carried out by Chintapalli *et al*. [28], on the testing and fabrication of novel, flexible armor designs that replicate the properties of teleost fish scales and skin.

Overall, this study supports teleost fish scales and skin as promising sources of biomimetic inspiration for the production of synthetic materials with effective protective properties in combination with several other desirable attributes such as flexibility, breathability, ultra-thinness, light weight, transparency, and energy storage and locomotory capabilities. The fabrication of biomimetic protective systems inspired from fish skin will soon be realized and may have important applications in the advancement of personal armor systems and other

protective coverings. The most evident biomimetic application for the study of the protective properties of teleost skin is the design of protective clothing and gear such as body armor and vests that have the capacity to withstand significant penetration forces and prevent blunt trauma from a variety of close-contact threats and mechanical disturbances such as puncture with sharp devices. A similar protective vest, called “Dragon Skin” and made by Pinnacle Armor [14] using steel and composite ceramic plates, was developed recently for military and ballistic applications and was inspired by the scalation patterns of different vertebrates including teleost fishes. However, the mechanisms and material properties learned from teleost fish skin and applied to the design of artificial, protective and flexible skins, can be used for the development of various other forms of protective coverings that are improved by possessing additional beneficial properties such as flexibility, breathability, ultra-thinness, light weight and transparency, for example flexible packaging materials, green house paneling, and hybrid vehicles [90].

As well, the tensile properties of teleost fish skin, and the role of the integument during fish locomotion and under bending deformation as a mechanical energy storage device, may allow for the design of fish skin-inspired, synthetic flexible skins with multiple functions in addition to high protective capacity, such as the promotion of locomotory efficiency. The structure of the s. compactum layer of the skin, that of a cross-helical arrangement of collagen fibres similar to the mechanical theory on open- and closed fibre-reinforced cylinders [31] and which provides the tendon-like properties to teleost skin, has additional mechanical benefits such as maximized body volume and resistance to principal stresses that may arise from internal pressure [17, 31, 32], as well as wrinkle prevention [16] and restriction of torsion or other body movements [17, 32, 34, 35] for improved hydrodynamics and swimming. Some of these mechanical benefits of a cross-helical arrangement of fibres have been incorporated into the

design of several fibre-reinforced cylindrical objects such as garden hoses and other rubber tubing [91] and the bodies of aircrafts [92]. The functions and mechanisms evolved by teleost and shark skin to improve swimming efficiency and performance, including pressure-resistance and torsion-resistance with stability and flotation effects, may also be applied to the improved design of ship hull hydrostats [17, 31, 32, 90], and to high-performance swim suit flotation (and energy storage) devices [17, 32, 34, 35, 90]. The applications for the biomimetic design of flexible, protective coverings with additional beneficial properties inspired from teleost fish skin, are wide ranging and have commenced with the manufacture of personal armor systems that employ similar mechanisms in the resistance to puncture and other mechanical disturbances as found in the natural, scaled skin of teleost fishes.

REFERENCES

1. Gosline, W.A. 1971. *Functional Morphology and Classification of Teleostean Fishes*. The University Press of Hawaii, Honolulu, U.S.A.
2. Wootton, R.J. 1990. *Ecology of Teleost Fishes*. Chapman and Hall, New York, U.S.A.
3. Nelson, J.S. 1994. *Fishes of the World, 3rd edition*. John Wiley & Sons Inc., New York, U.S.A.
4. Moyle, P.B, & J.J. Cech, Jr. 2004. *Fishes - An Introduction to Icthyology, 5th edition*. Prentice Hall, Upper Saddle River, U.S.A.
5. Helfman, G.S., Collette, B.B., Facey, D.E., & B.W. Bowen. *The Diversity of Fishes - Biology, Evolution, and Ecology, 2nd edition*. John Wiley & Sons Ltd., West Sussex, England.
6. Hartman, K.J. 1999. Predation on striped bass. *Proc. Atlantic Striped Bass Workshop and Roundtable Discussion*, p. 6.
7. Bemis, W.E., Giuliano, A., & B. McGuire. 2005. Structure, attachment, replacement and growth of teeth in bluefish, *Pomatomus saltatrix* (Linnaeus, 1766), a teleost with deeply socketed teeth. *Zoology* **108**, 317-327.
8. Elliot, D.G. 2000. Chapter 5 - Integumentary System (Gross Functional Anatomy), Chapter 17 - Integumentary System (Microscopic Functional Anatomy). In: Ostrander, G.K., (Ed.), *The Laboratory Fish*. Academic Press, Oxford, England, pp. 95-108, 271-306.
9. Whitear, M. 1986. The skin of fishes including cyclostomes. In: Bereiter-Hahn, J., Matoltsy, A., Richards, K., (Eds.), *Biology of the Integument - 2 Vertebrates*. Springer, Berlin, Germany, pp. 8-77.

10. Sire, J.-Y. 1990. From ganoid to elasmoid scales in the actinopterygian fishes. *Neth. J. Zool*. **40**, 75-92.

11. Barthelat, F. 2007. Biomimetics for next generation materials. *Phil. Trans. R. Soc. A* **365**, 2907-2919.

12. Ball, P. 1999. Engineering: shark skin and other solutions. *Nature* **400**, 507-509.

13. Sim, D., & J. Kaminski. 2012. *Roman imperial armour: The production of early imperial military armour*. Oxbow Books, Oxford, England.

14. Pinnacle Armor. 2014. http://www.pinnaclearmor.com/body-armor/dragon-skin/.

15. Bruet, B.J.F., Song, J.H., Boyce, M.C., & C. Ortiz. 2008. Materials design principles of ancient fish armour. *Nat. Mater*. **7**, 748-756.

16. Hebrank, M.R., & J. H. Hebrank. 1986. The mechanics of fish skin: lack of an "external tendon" role in two teleosts. *Biol. Bull*. **171**, 236-247.

17. Wainwright, S.A., Vosburgh, F., & J.H. Hebrank. 1978. Shark skin: function in locomotion. *Science* **202**, 747-749.

18. Barthelat, F., Tang, H., Zavattieri, P.D., Li, C.-M., & H.D. Espinosa. 2007. On the mechanics of mother-of-pearl: a key feature in the material hierarchical structure. *J. Mech. Phys. Solids* **55**, 306-337.

19. Aizenberg, J., Weaver, J.C., Thanawala, M.S., Sundar, V.C., Morse, D.E., & P. Fratzl. 2005. Skeleton of *Euplectella* sp.: structural hierarchy from the nanoscale to the macroscale. *Science* **309**, 275-278.

20. Meyers, M.A. 2006. Toucan beaks engineered for strength and low density. *Adv. Mater. Process.* **164**, 121.

21. Fratzl, P. 2007. Biomimetic materials research: what can we really learn from nature's structural materials? *J. R. Soc. Interface* **4**, 637-642.

22. Barthelat, F., & H.D. Espinosa. 2007. An experimental investigation of deformation and fracture of nacre-mother of pearl. *Exp. Mech*. **47**, 311-324.

23. Tang, Z., Kotov, N.A., Magonov, S., & B. Ozturk. 2003. Nanostructured artificial nacre. *Nat. Mater*. **2**, 413-418.

24. Tuan, W.-H., Yu, Y.-J., & Y.-L. Chin. 2011. From biomimetic concept to engineering reality - a case study on the design of ceramic reinforcement. *Adv. Eng. Mater*. **13**, 351-355.

25. Currey, J.D. 1999. The design of mineralised hard tissues for their mechanical functions. *J. Exp. Biol*. **202**, 3285–3294.

26. Sire, J.-Y. 1986. Ontogenic development of surface ornamentation in the scales of *Hemichromis bimaculatus* (Cichlidae). *J. Fish Biol*. **28**, 713-724.

27. Sudo, S., Tsuyuki, K., Ito, Y., & T. Ikohagi. 2002. A study on the surface shape of fish scales. *JSME Int. J. Ser. C* **45**, 1100-1105.

28. Chintapalli, R., Mirkhalaf, M., Dastjerdi, A.K., & F. Barthelat. 2014. Fabrication, testing and modeling of a new flexible armor inspired from natural fish scales and osteoderms. *Bioinspir. Biomim*. **9**, 036005.

29. Vernerey, F.J., Musiket, K., & F. Barthelat. 2014. Mechanics of fish skin: a computational approach for bio-inspired flexible composites. *Int. J. Solids Struct*. **51**, 274-283.

30. Vernerey, F.J., & F. Barthelat. 2014. Skin and scales of teleost fish: simple structure but high performance and multiple functions. *J. Mech. Phys. Solids* **68**, 66-76.

31. Wainwright, S.A., Biggs, W.D., Currey, J.D., & J.M. Gosline. 1976. *Mechanical Design in Organisms*. Edward Arnold Publishers Ltd., London, England, pp. 293-296.

32. Vogel, S. 2003. Hydrostatic Structures. In: *Comparative Biomechanics: Life's Physical World*. Princeton University Press, Princeton, U.S.A., pp. 407-422.

33. Motta, P.J. 1977. Anatomy and functional morphology of dermal collagen fibers in sharks. *Copeia* **3**, 454-464.

34. Lingham-Soliar, T. 2005. Caudal Fin in the white shark, *Carcharodon carcharias* (Lamnidae): a dynamic propeller for fast, efficient swimming. *J. Morphol*. **264**, 233-252.

35. Flammang, B.E. 2010. Functional morphology of the radialis muscle in shark tails *J. Morphol*. **271**, 340-352.

36. Fouda, M.M. 1979. Studies on scale structure in the common goby *Pomatoschistus microps* Krøyer *J. Fish Biol*. **15**, 173-183.

37. Schonborner, A.A., Boivin, G., & C.A. Baud. 1979. The mineralization processes in teleost fish scales. *Cell Tiss. Res*. **202**, 203-212.

38. Lanzing, W.J.R., & D.R. Higginbotham. 1974. Scanning microscopy of surface structures of *Tilapia mossambica* (Peters) scales *J. Fish Biol*. **6**, 307-310.

39. Hollander, R.R. 1986. Microanalysis of scales of poeciliid fishes. *Copeia* **1**, 86-91.

40. Brown, G.A., & S.R. Wellings. 1969. Collagen formation and calcification in teleost scales. *Z. Zellforsch*. **93**, 571-582.

41. Seshaiya, R.V., Ambujabai, P., & M. Kalyani. 1963. Amino acid composition of ichthylepidin from fish scales. In: Ramachandran, G.N., (Ed.), *Aspects of protein structure*. Academic Press, New York, U.S.A., pp. 68-91.

42. Meunier, F.J. 1984. Spatial organization and mineralization of the basal plate of elasmoid scales in osteichthyans. *Amer. Zool.* **24**, 953-964.

43. Ogawa, N., Ura, K., & Y. Takagi. 2010. Scale calcification in the goldfish in vitro: histological and quantitative analysis. *Fisheries Sci.* **76**, 189-198.

44. Marino Cugno Garrano, A., La Rosa, G., Zhang, D., Niu, L.-N., Tay, F.R., Majd, H., & D. Arola. 2012. On the mechanical behavior of scales from *Cyprinus carpio*. *J. Mech. Behav. Biomed. Mater.* **7**, 17–29.

45. Meunier, F.J. 1981. 'Twisted plywood' structure and mineralization in the scales of a primitive living fish *Amia calva*. *Tissue & Cell* **13**, 165-171.

46. Meunier, F.J., & J. Castanet. 1982. Organisation spatiale des fibres de collagene de la plaque basale des ecailles des Teleosteens. *Zool. Scripta* **11**, 141-153.

47. Zylberberg, L., Bereiter-Hahn, J., & J.-Y. Sire. 1988. Cytoskeletal organization and collagen orientation in the fish scales*. *Cell Tiss. Res.* **253**, 597-607.

48. Bigi, A., Burghammer, M., Falconi, R., Koch, M.H.J., Panzavolta, S., & C. Riekel. 2001. Twisted plywood pattern of collagen fibrils in teleost scales: an x-ray diffraction investigation. *J. Struct. Biol.* **136**, 137-143.

49. Youn, H.S., & T.J. Shin. 2009. Supramolecular assembly of collagen fibrils into collagen fiber in fish scales of red seabream, *Pagrus major*. *J. Struct. Biol.* **168**, 332-336.

50. Scheyer, T.M., Sander, P.M., Joyce, W.G., Boehme, W., & U. Witzel. 2007. A plywood structure in the shell of fossil and living soft-shelled turtles (Trionychidae) and its evolutionary implications. *Org. Divers. Evol.* **7**, 136-144.

51. O'Connell, G.D., Sen, S., & D.M. Elliott. 2012. Human annulus fibrosus material properties from biaxial testing and constitutive modeling are altered with degeneration. *Biomech. Model. Mechanobiol.* **11**, 493–503.

52. Zylberberg, L., Bonaventure, J., Cohen-Solal, L., Hartmann, D.J., & J. Bereiter-Hahn. 1992. Organization and characterization of fibrillar collagens in fish scales in situ and in vitro. *J. Cell Sci.* **103**, 273-285.

53. Bereiter-Hahn, J., & L. Zylberberg. 1993. Regeneration of teleost fish scale. *Comp. Biochem. Physiol.* **105A**, 625-641.

54. Ikoma, T., Kobayashi, H., Tanaka, J., Walsh, D., & S. Mann. 2003. Microstructure, mechanical, and biomimetic properties of fish scales from *Pagrus major*. *J. Struct. Biol.* **142**, 327-333.

55. Meunier, F.J., & P.M. Brito. 2004. Histology and morphology of the scales in some extinct and extant teleosts. *Cybium* **28**, 225-235.

56. Torres, F.G., Troncoso, O.P., Nakamatsu, J., Grande, C.J., & C.M. Gomez. 2008. Characterization of the nanocomposite laminate structure occurring in fish scales from *Arapaima gigas*. *Mater. Sci. Eng. C* **28**, 1276-1283.

57. Zylberberg, L., Geraudie, J., Meunier, F.J., & J.-Y. Sire. 1992. Biomineralization in the integumental skeleton of the living lower vertebrates. In: Hall, B.K., (Ed.), *Bone Volume 4 - Bone metabolism and mineralization*. CRC Press Inc., Boca Raton, U.S.A., pp. 171-224.

58. Zylberberg, L., Meunier, F.J., & M. Laurin. 2010. A microanatomical and histological study of the postcranial dermal skeleton in the Devonian sarcopterygian *Eusthenopteron foordi*. *Acta Palaeontol. Pol.* **55**, 459-470.

59. Meyers, M.A., Lin, Y.S., Olevsky, E.A., & P.-Y. Chen. 2012. Battle in the Amazon: Arapaima versus Piranha. *Adv*. *Eng*. *Mater*. **14**, B279–B288.

60. Henrikson, R.C., & A.G. Matoltsy. 1968. The fine structure of teleost epidermis I. Introduction and filament-containing cells. *J. Ultrastruct*. *Res*. **21**, 194-212.

61. Naresh, M.D., Arumugam, V., & R. Sanjeevi. 1997. Mechanical behaviour of shark skin. *J*. *Biosci*. **22**, 431-437.

62. Meyers, M.A., Lin, A.Y.M., Seki, Y., Chen, P.Y., Kad, B.K., & S. Bodde. 2006. Structural biological composites: an overview. *JOM Journal of the Minerals, Metals & Materials Society* **58**, 35-41.

63. Fratzl, P., & R. Weinkamer. 2007. Nature's hierarchical materials. *Prog*. *Mater*. *Sci*. **52**, 1263-1334.

64. Szewciw, L.J., de Kerckhove, D.G., Grime, G.W., & D.S. Fudge. 2010. Calcification provides mechanical reinforcement to whale baleen alpha-keratin. *Proc*. *Roy*. *Soc*. *B* **277**, 2597-2605.

65. Vernerey, F.J., & F. Barthelat. 2010. On the mechanics of fishscale structures. *Int*. *J*. *Solids Struct*. **47**, 2268–2275.

66. Hebrank, M.R. 1980. Mechanical properties and locomotor function of eel skin. *Biol*. *Bull*. **158**, 58-68.

67. Jawad, L.A. 2005. Comparative morphology of scales of four teleost fishes from Sudan and Yemen. *J*. *Nat*. *Hist*. **39**, 2643-2660.

68. Liu, W.T., Zhang, Y., Li, G.Y., Miao, Y.Q., & X.H. Wu. 2008. Structure and composition of teleost scales from snakehead *Channa argus* (Cantor) (Perciformes: Channidae). *J*. *Fish Biol*. **72**, 1055-1067.

69. Bass, E.C., Ashford, F.A., Segal, M.R., & J.C. Lotz. 2004. Biaxial testing of human annulus fibrosus and its implications for a constitutive formulation. *Ann. Biomed. Eng.* **32**, 1231-1242.

70. Liu, C., & S. Shen. 1991. Lepidology of the mugilid fishes. *J. Taiwan. Mus.* **44**, 321-357.

71. Barthelat, F., & J. Poissant. 2010. A novel "subset splitting" procedure for digital image correlation on discontinuous displacement fields. *Exp. Mech.* **50**, 353-364.

72. Shen, Z.L., Dodge, M.R., Kahn, H., Ballarini, R., & S.J. Eppell. 2008. Stress-strain experiments on individual collagen fibrils. *Biophys. J.* **95**, 3956-3963.

73. ASTM-D412. Standard test methods for vulcanized rubber and thermoplastic elastomers - tension, Figure 1: Standard dies for cutting dumbbell specimens.

74. Yang, W., Chen, I.H., Gludovatz, B., Zimmermann, E.A., Ritchie, R.O., & M.A. Meyers. 2013. Natural flexible dermal armor. *Adv. Mater.* **25**, 31-48.

75. Wang, L.F., Song, J.H., Ortiz, C., & M.C. Boyce. 2009. Anisotropic design of a multilayered biological exoskeleton. *J. Mater. Res.* **24**, 3477-3497.

76. Ikoma, T., Kobayashi, H., Tanaka, J., Walsh, D., & S. Mann. 2003. Physical properties of type I collagen extracted from fish scales of *Pagrus major* and *Oreochromis niloticas*. *Int. J. Biol. Macromol.* **32**, 199-204.

77. Burdak, V.D., 1979. Morphologie fonctionnelle du tegument ecailleux des poissons. Kiev: La Pensee Scientifique (in Russian). French translation, *Cybium* **10,** 1986, 1-147.

78. Browning, A., Ortiz, C., & M.C. Boyce. 2013. Mechanics of composite elasmoid fish scale assemblies and their bioinspired analogues. *J. Mech. Behav. Biomed. Mater.* **19**, 75-86.

79. Onozato, H., & N. Watabe. 1979. Studies on fish scale formation and resorption III. Fine

structure and calcification of the fibrillary plates of the scales in *Carassius auratus* (Cypriniformes: Cyprinidae). *Cell Tiss*. *Res*. **201**, 409-422.

80. Barthelat, F., & R. Rabiei. 2011. Toughness amplification in natural composites. *J*. *Mech*. *Phys*. *Solids* **59**, 829-840.

81. Buehler, M.J. 2010. Tu(r)ning weakness to strength. *Nano Today* **5**, 379-383.

82. Keten, S., Xu, Z.P., Ihle, B., & M.J. Buehler. 2010. Nanoconfinement controls stiffness, strength and mechanical toughness of beta-sheet crystals in silk. *Nat*. *Mater*. **9**, 359-367.

83. Gemballa, S., & P. Bartsch. 2002. Architecture of the integument in lower teleostomes: functional morphology and evolutionary implications. *J*. *Morphol*. **253**, 290-309.

84. Long, J.H., Hale, M.E., McHenry, M.J., & M.W. Westneat. 1996. Functions of fish skin: flexural stiffness and steady swimming of longnose gar *Lepisosteus osseus*. *J*. *Exp*. *Biol*. **199**, 2139-2151.

85. De luliis, G., & D. Pulera. 2001. *The Dissection of Vertebrates: A Laboratory Manual, 2nd edition*. Academic Press, Burlington, U.S.A.

86. Jayne, B.C., & G.V. Lauder. 1995. Speed effects on midline kinematics during steady undulatory swimming of largemouth bass, *Micropterus salmoides*. *J. Exp. Biol.* **198**, 585-602.

87. Aleyev, Y.G. 1977. *Nekton*. W. Junk, The Hague.

88. Tytell, E.D., Borazjani, I., Sotiropoulos, F., Baker, T.V., Anderson, E.J., & G.V. Lauder. 2010. Disentangling the functional roles of morphology and motion in the swimming of fish. *Int. Comp. Biol.* **50**, 1140-1154.

89. Poissant, J., & F. Barthelat. 2012. In-situ mechanical testing of hydrated biological nanofibers using a nanoindenter transducer. *Exp*. *Mech*. **52**, 1287-1295.

90. AskNature & The Biomimicry 3.8 Institute. 2014. http://www.asknature.org/, http://biomimicry.net/.

91. TANIQ, Reinforced Rubber Technology. 2014. http://www.taniq.com/.

92. Soutis, C. 2005. Fibre reinforced composites in aircraft construction. *Prog. Aerosp. Sci.* **41**, 143-151.